QUANTUM AND CLASSICAL PHASE TRANSITIONS IN DISORDERED SYSTEMS

by

GAURAV RAMESH KHAIRNAR

A DISSERTATION

Presented to the Graduate Faculty of the

MISSOURI UNIVERSITY OF SCIENCE AND TECHNOLOGY

In Partial Fulfillment of the Requirements for the Degree

DOCTOR OF PHILOSOPHY

in

PHYSICS

2025

Approved by:

Dr. Thomas Vojta, Advisor
Dr. Aleksandr Chernatynskiy
Dr. Julia Medvedeva
Dr. Alexey Yamilov
Dr. Adrian Del Maestro

PUBLICATION DISSERTATION OPTION

This dissertation consists of the following three articles, formatted in the style used by the Missouri University of Science and Technology.

Paper I: Pages 33-55 has been published as *Phase boundary near a magnetic percolation transition* in The European Physical Journal B, 94, 43 (2021) with Cameron Lerch and Thomas Vojta.

Paper II: Pages 56-81 has been published as *Helicity modulus and chiral symmetry breaking for boundary conditions with finite twist* in Physical Review E 111, 024114 (2025) with Thomas Vojta.

Paper III: Pages 82-126 has been published as *Phases and phase transitions of the disordered quantum clock model* in Physical Review B 111, 094212 (2025) with Vishnu Pulloor Kuttanikkad, Rajesh Narayanan and Thomas Vojta.

ABSTRACT

This work examines the effects of quenched disorder on classical and quantum phase transitions. There are countless examples of phase transitions in nature. Here, we study phase transitions in condensed matter with the help of simple models that focus on the essential unifying features of the problems. We are particularly interested in investigating how the presence of disorder changes the behavior of the system in the vicinity of a phase transition.

Here, we discuss three closely related problems regarding phase transitions. First we consider the behavior of highly diluted magnets with varying dilution levels in order to explain the unusual phase diagram observed in experiments on hexaferrite materials through a percolation scenario. Next, we study the response of a two-dimensional planar (XY) magnet to a finite twist in the boundary conditions. Such boundary conditions are important for numerous experimental scenarios and computational methods. Then, we investigate the phase diagram of the disordered quantum clock model in one dimension. This system exhibits multiple phases and phase transitions that are strongly affected by disorder.

To understand the phase transitions in the above systems, we analyze the equilibrium properties of thermodynamic observables using large-scale Monte Carlo simulations. The utility of the simulations is further enhanced by a sophisticated finite-size scaling analysis. Our research presents a comprehensive analysis of the disorder dependence of phases and phase transitions in the aforementioned systems. Through rigorous investigation, we demonstrate that disorder gives rise to a diverse array of novel phenomena. These include alterations in universality class, the emergence of infinite randomness criticality, and Griffiths singularities.

ACKNOWLEDGMENTS

First and foremost, I extend my deepest appreciation to my advisor, Dr. Thomas Vojta, whose expertise, patience, and unwavering support have been instrumental in shaping both this dissertation and my growth as a researcher. Your insights and rigor to solve any problem at hand has been truly inspirational, and I hope to become a successful researcher as yourself.

I am also indebted to the members of my dissertation committee: Dr. Medvedeva, Dr. Chernatynskiy, Dr. Yamilov and Dr. Del Maestro. I am deeply grateful for your time and effort in reviewing my work. Your constructive feedback, valuable insights, and motivation enhanced quality and depth of my work.

I would like to express sincere thanks to my external collaborators, Cameron, Vishnu, and Dr. Narayanan. I am really fortunate to have gotten an opportunity to work with you. I would like to acknowledge Martin, Jack, Xuecheng, Hatem, Reece, Jonathan, Angela, and Logan; it was a great pleasure exploring various research interests together.

I owe a great part of my success to all the faculty members of the physics department, whose continuous commitment greatly inspired me throughout my time here. Interacting with Dr. Waddill, Dr. Jentschura, Dr. Wilemski, Dr. Agnes Vojta, Dr. Parris, and Dr. Musser had a defining impact on me as a graduate student. To my colleagues and friends in the department, thank you for the stimulating discussions, collaborative spirit, and moments of levity that made this place special. My sincere appreciation goes to the administrative staff, Trish, Michelle, Jason, and Pam; for their efforts in managing the daily operations of the department, ensuring a supportive environment.

On a personal note, I am eternally grateful to my family for their unconditional love, patience and support. I dedicate this thesis to them.

TABLE OF CONTENTS

Page

PAPER

LIST OF ILLUSTRATIONS

Figure Page

SECTION

PAPER I

PAPER II

PAPER III

LIST OF TABLES

1. INTRODUCTION

Condensed matter physics is a study of emergent physical properties of matter. Microscopically, matter is composed of electrons and ions. Understanding how a large number of these quantum particles interacting strongly with their neighbors lead to the physical properties of materials is the central objective of the subject. Most of the properties of practical interest such as transport, thermal, optical and magnetic properties are governed by the low-energy dynamics of the system. Moreover, many qualitative features of the collective behavior exhibited by these large systems are believed to be completely characterized by dimensionality and fundamental symmetries, even if the microscopic details vary. This principle of "universality" allows one to formulate simple model Hamiltonians. As condensed matter systems consist of a large number of constituents, great progress is made possible by applying the principles of statistical physics. Alternatively, condensed matter systems can serve as useful testing platforms for statistical physics.

Many important concepts have been developed based on these ideas, including band theory of solids, density functional theory, Bardeen-Cooper-Schrieffer theory of superconductivity, Anderson localization, topological phase transition, and renormalization group theory. Often, progress has led to even greater mysteries such as high-temperature superconductivity, non-Fermi liquid behavior, many-body localization phenomena, topological phases of matter, etc.

Amongst numerous milestones of the field, the concept of phase transitions is a crucial one. A phase transition is said to occur when the physical properties of a system change abruptly as some system parameter is varied. Understanding how the interplay of interactions and fluctuations can lead to phase transitions naturally provides an organizing principle in condensed matter physics. Such insight leads to the development and discovery of new materials whose desirable phases can be controlled.

1.1. EXAMPLES OF PHASE TRANSITION

We will now present some examples of phase transitions to motivate the subsequent discussion. Different phases are distinguished using a quantity called order parameter. Usually order parameter is zero in one phase and non-zero in another phase [1].

1. Hexagonal ferrites such as $PbFe_{12}O_{19}$, $SrFe_{12}O_{19}$, $BaFe_{12}O_{19}$ have wide range of commercial applications due to their remarkable magnetic properties. These compounds crystallize in the magnetoplumbite structure. A double unit cell consists of 24 Fe^{3+}, all in spin state $S = 5/2$ [1] (see Fig. 1.1). At room temperature, 8 Fe ions on sublattices $4f$ are oriented anti-parallel to the remaining 16 Fe ions in the double unit cell, giving rise to nonzero magnetization. If the temperature is increased, net magnetization decreases , and around $720K$ thermal fluctuations dominate to destroy spontaneous magnetization. The temperature at which this transition to paramagnetic phase occurs is called the Curie temperature T_c.

2. Next consider the magnetic properties of compounds like $LiHoF_4$ or $LiTbF_4$. The Ho or Tb spins fluctuate between parallel or antiparallel orientations with respect to a certain crystalline axis [2]. The magnetic dipolar interaction between the Ho ions leads to a ferromagnetic state in which all spins point parallel to each other at the lowest temperatures. Now, the application of magnetic field in transverse direction to the preferred spin axis facilitates tunneling between the two spin orientations. At large field strengths compared to magnetic dipolar interaction, the quantum tunneling can overcome the long-range magnetic order. This transition at $T = 0$ is driven by quantum fluctuations and is called a quantum phase transition [3].

[1] Topological phase transitions involve changes in the nonlocal topological invariants. The topologically ordered phases do not always have a conventional local order parameter associated with them, see example below.

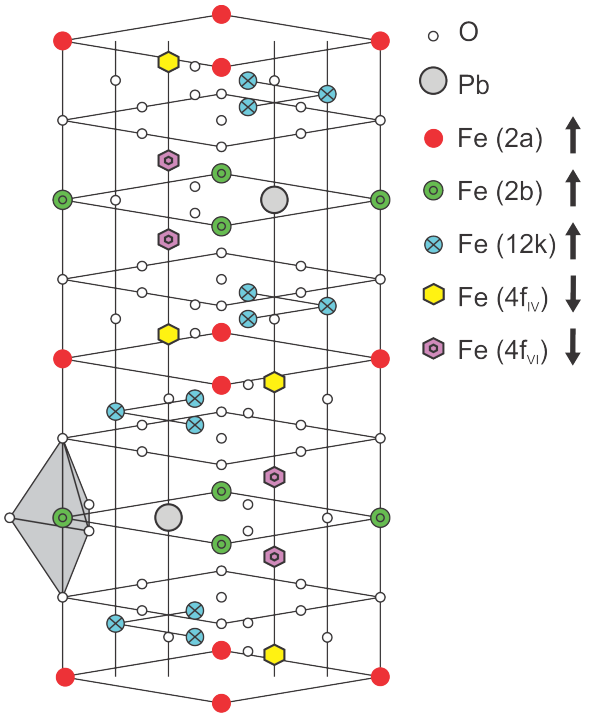

Figure 1.1. Double unit cell of $PbFe_{12}O_{19}$ [1].

3. Liquid Helium undergoes a superfluid phase transition at low temperature. A true long-range ordered superfluid phase is forbidden in two dimensions by statistical mechanics [4]. Whether superfluidity exists for a two dimensional Helium film is therefore an interesting question. It is now understood that two-dimensional Helium films exhibit topological quasi-long-range order at low temperatures. The superfluid is populated by bound vortex and antivortex pairs. At high temperatures, these pairs dissociate, and the free vortices destroy superfluidity. This type of phase transition lacks an obvious order parameter and is called a topological phase transition [5, 6].

4. Consider a random composite system of metal and ceramics. One can investigate electrical conductivity of the composite as the volume fractions of the constituents are varied. At low concentrations of metal, conductivity across the sample will be zero due to disconnected clusters of the metal particles. For higher metal concentrations,

the metallic grains form a connected network, and the sample is conducting. The critical concentration at which sample becomes conducting is called percolation threshold, and the phase transition across this threshold is referred to as the percolation phase transition [7].

These examples demonstrate that as we change some control parameter such as temperature, external magnetic field, or chemical composition, the system undergoes a phase transition. We are interested in the behavior near phase transitions, also known as critical behavior. A phase transition can be classified as a first order transition, if there is a finite discontinuity in the first derivative of the free energy (or, the ground state energy in the case of quantum phase transition). If the first derivative is continuous, and there is a discontinuity in the higher derivative of the free energy, then the transition is called a continuous transition. In the next sections, we will discuss theoretical descriptions of phase transitions and the effects of disorder.

1.2. THEORETICAL MODELS

There are countless examples of phase transitions in addition to the ones mentioned above. Developing a complete microscopic description for each problem is a formidable and near impossible task. However different phase transitions share unifying properties that only depend on characteristics such as the dimensionality of space, symmetry of the order parameter, presence of disorder. Great progress can thus be made by keeping only these essential features of the system under investigation. The resulting "simple" models are numerically tractable and provide a qualitative understanding of the critical behavior. Now we introduce two models which are instrumental to understand the phase transition examples mentioned in the previous section.

1.2.1. Ising Model. The classical Ising model, consists of "spin" variables on a hypercubic lattice in d dimensions that take values $S_i = \pm 1$ [3]. Its Hamiltonian is given by

$$H = -J \sum_{\langle ij \rangle} S_i S_j - h \sum_i S_i. \tag{1.1}$$

The first term describes interaction with nearest neighbor spins. If the exchange constant $J > 0$, spins favor parallel alignment and for $J < 0$ anti-parallel alignment. The second term in the Hamiltonian captures the influence of an external magnetic field h. The partition function for the Ising model in one dimension can be analytically calculated. The same is true in two dimensions, but only in the absence of an external field. For higher dimensions or in the presence of an external field, accurate results can be obtained by powerful numerical methods such as Monte Carlo simulations, perturbation theory or renormalization group procedures. Phase transitions do not occur in one-dimensional Ising model. In higher dimensions, the Ising model undergoes a phase transition between a high-temperature paramagnetic phase and a low-temperature ferromagnetic phase at critical temperature T_c. In addition to modeling certain magnetic systems, the Ising model can be applied to many other systems with binary degrees of freedom.

At low temperatures, the quantum character of the spin variables becomes important. This can be captured by the quantum Ising model or transverse field Ising model,

$$H = -J \sum_{\langle ij \rangle} \hat{\sigma}_i^z \hat{\sigma}_i^z - h_\perp \sum_i \hat{\sigma}_i^x - h_\parallel \sum_i \hat{\sigma}_i^z \tag{1.2}$$

where $\hat{\sigma}$ are Pauli matrices. In the basis where $\hat{\sigma}^z$ is diagonal,

$$\hat{\sigma}^z = \begin{pmatrix} 1 & 0 \\ 0 & -1 \end{pmatrix}, \quad \hat{\sigma}^y = \begin{pmatrix} 0 & -i \\ i & 0 \end{pmatrix}, \quad \hat{\sigma}^x = \begin{pmatrix} 0 & 1 \\ 1 & 0 \end{pmatrix}. \tag{1.3}$$

The eigenstates of $\hat{\sigma}^z$, which have eigenvalues ± 1, correspond to the two orientations of Ising spin. In the absence of the transverse-field, $h_\perp = 0$, the Hamiltonian will be diagonal in the basis of eigenstates of $\hat{\sigma}_i^z$, and the system reduces to the classical Ising model. Presence of the transverse field induces quantum mechanical tunneling between the two $\hat{\sigma}^z$ eigenstates.

Lets consider the qualitative behavior of the model at zero temperature and $h_\parallel = 0$. If $J \gg h_\perp$, the energy of the ground state is minimized if all the spins are aligned parallely. This gives us the doubly degenerate ferromagnetic ground state. Spins are correlated over long distances, and the spin correlation length ξ, is infinite (or only limited by the the linear size L of the system). In the opposite limit, $J \ll h_\perp$, the transverse field dominates, i.e. the ground state is approximately given by a direct product of eigenstates of $\hat{\sigma}^x$. Therefore the $\hat{\sigma}^z$ values at different sites are uncorrelated. This state is called a quantum paramagnet, where spin correlations decay exponentially, $\langle \hat{\sigma}_i^z \hat{\sigma}_j^z \rangle \sim \exp(-|x_i - x_j|/\xi)$. The ground states in the two limits differ qualitatively from each other, suggesting that for a critical value(s) of $h_\perp/J$, system undergoes a phase transition. Finally, at nonzero temperatures, $T > 0$, thermal fluctuations destroy the magnetic order and phase transition occurs at lower critical value of $h_\perp/J$. The temperature at which magnetic order is destroyed is called the critical temperature T_c. Fig. 1.2 shows the resulting schematic phase diagram.

1.2.2. Quantum Rotor Model. A quantum rotor can be imagined as a quantum particle constrained to move on a N-dimensional hyper-sphere [3]. The orientation of the rotor can be described by an N-component unit vector $\hat{\mathbf{n}}$, with $\hat{\mathbf{n}}^2 = 1$. Kinetic energy of the rotor is given by

$$H_K = \frac{U}{2}\hat{\mathbf{L}}^2 \tag{1.4}$$

where, $1/U$ is the moment of inertia, and $\hat{\mathbf{L}}$ is angular momentum. For $N = 2$, energy eigenvalues are $Ul^2/2$ for $l = 0, 1, 2, ...$, with degeneracy $2 - \delta_{l,0}$. For $N = 3$, eigenvalues are $Ul(l+1)/2$ with degeneracy $2l + 1$.

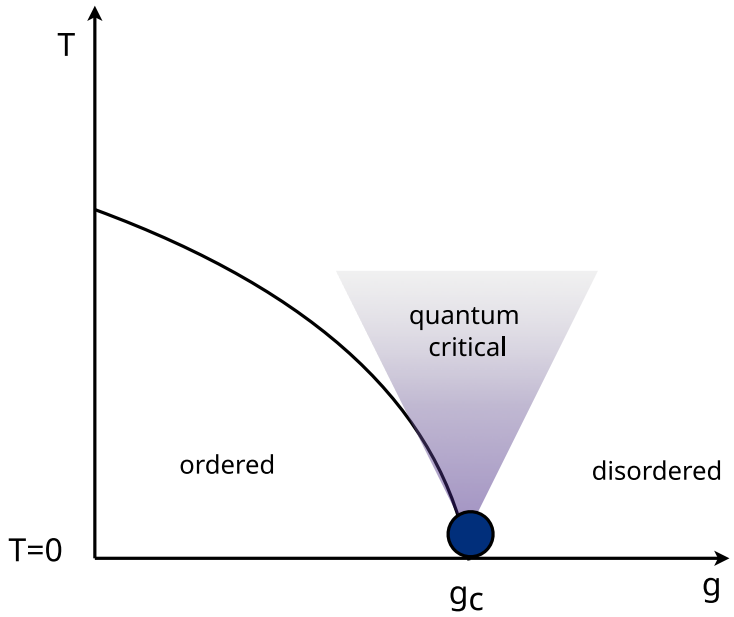

Figure 1.2. Schematic phase diagram of the quantum Ising model in $d \geq 2$ as function of temperature T and $g = h_{\perp}/J$ for $h_{\parallel} = 0$. Quantum phase transition occurs at zero temperature and at critical value g_c of tuning parameter. The solid black curve indicates classical phase transition from ordered to disordered phases. The shaded region is called the quantum critical region, where signatures of quantum phase transitions are still accessible at finite temperatures [3].

Now these rotors are placed on an d-dimensional hypercubic lattice, and they are coupled to neighbors. The full Hamiltonian of the resulting rotor model reads,

$$H = \frac{U}{2} \sum_i \hat{\mathbf{L}}_i^2 - t \sum_{\langle ij \rangle} \hat{\mathbf{n}}_i \cdot \hat{\mathbf{n}}_j. \tag{1.5}$$

The interaction energy is minimized when the rotors are oriented parallely, i.e. in a long-range ordered state. On the other hand, the kinetic energy is minimized when the orientations of the rotors is maximally uncertain. In the absence of interaction term, the system will prefer to be in quantum disordered state where the rotors are uncorrelated and oriented randomly.

Consider the case of $N = 2$. The components of the rotor can be described by $\hat{\mathbf{n}}_i = (\cos\theta_i, \sin\theta_i)$, where an angular variable θ_i is introduced at each site. In the angle eigenbasis, the angular momentum operator is given by, $\hat{L}_i = \frac{1}{i}\frac{\partial}{\partial\theta_i}$. Then the Hamiltonian reads,

$$H = \frac{U}{2}\sum_i \left(\frac{1}{i}\frac{\partial}{\partial\theta_i}\right)^2 - t\sum_{\langle ij\rangle}\cos(\theta_i - \theta_j). \tag{1.6}$$

In the large U limit, the eigenstates of the Hamiltonian are simultaneous eigenstates of angular momentum, and are denoted by $\prod_i |m_i\rangle$, where m_i is the integer angular momentum associated with the wave functions $\exp(im_i\theta_i)$.

There are no elementary quantum rotors in nature. However, the quantum rotor Hamiltonian eq. (1.6) can be understood as a limiting case of the Bose Hubbard model,

$$H_B = -\tilde{t}\sum_{\langle ij\rangle}(\hat{b}_i^\dagger\hat{b}_j + \hat{b}_j^\dagger\hat{b}_i) - \mu\sum_i \hat{n}_{bi} + \frac{\tilde{U}}{2}\sum_i \hat{n}_{bi}(\hat{n}_{bi} - 1) \tag{1.7}$$

where, $\hat{n}_{bi} = \hat{b}_i^\dagger\hat{b}_i$ is a number operator, $\hat{b}_i, \hat{b}_i^\dagger$ are the boson annihilation and creation operators on the site i. They satisfy commutation relation, $[\hat{b}_i, \hat{b}_j^\dagger] = \delta_{ij}$. The first term allows hopping of bosons between nearest neighbors. The second term corresponds to chemical potential μ and controls the total number of bosons. The last term captures on-site interaction between the bosons. In the limit, $\tilde{t} \gg \tilde{U}$, hopping dominates and lowest energy state is delocalized boson condensate. If interaction dominates, $\tilde{t} \ll \tilde{U}$, strong on-site repulsion prevents addition of new bosons and global coherence is not possible and ground state is the Mott insulator.

In the limit of large integer filling, $n_b \gg 1$, Bose-Hubbard Hamiltonian can be written in the angle representation as quantum rotor Hamiltonian as written in eq. (1.6). Alternatively, quantum rotors also appear as effective degree of freedom in certain quantum magnets.

1.3. QUANTUM-CLASSICAL CORRESPONDENCE

In this section, we show that the partition function of the quantum rotor model (1.6) can be mapped onto that of a classical Hamiltonian called the XY model [8]. The quantum rotor Hamiltonian (1.6) can be decomposed into the kinetic energy part $\hat{T}$, and the potential energy, $\hat{V}$

$$\hat{T} = \frac{U}{2}\sum_{\vec{r}}\left(\frac{1}{i}\frac{\hat{\partial}}{\partial\theta_{\vec{r}}}\right)^2, \hat{V} = -t\sum_{\langle\vec{r},\vec{r}'\rangle}\cos(\hat{\theta}_{\vec{r}'} - \hat{\theta}_{\vec{r}}).$$

(Note that we are using $\vec{r}$ and $\vec{r}'$ to denote spatial positions.)

The partition function of the quantum rotor model,

$$Z = \mathrm{Tr}(\mathrm{e}^{-\beta\hat{H}}) = \mathrm{Tr}(\mathrm{e}^{-\beta(\hat{T}+\hat{V})}), \tag{1.8}$$

can be expressed in terms of the angle eigenbasis

$$Z = \int \mathrm{D}\theta\, \langle\theta|\mathrm{e}^{-\beta(\hat{T}+\hat{V})}|\theta\rangle = \lim_{M\to\infty}\int \mathrm{D}\theta\, \langle\theta|\left(\mathrm{e}^{-\frac{\beta}{M}\hat{T}}\mathrm{e}^{-\frac{\beta}{M}\hat{V}}\right)^M|\theta\rangle$$

where we have used the Trotter product formula, $e^{\hat{A}+\hat{B}} = \lim_{M\to\infty}(e^{\hat{A}/M}e^{\hat{A}/M})^M$. Inserting complete sets of angle eigenstates, we obtain

$$Z = \lim_{M\to\infty}\int \mathrm{D}\theta\, \langle\theta(\tau_0)|(\mathrm{e}^{-\frac{\beta}{M}\hat{T}}\mathrm{e}^{-\frac{\beta}{M}\hat{V}})|\theta(\tau_1)\rangle \ldots \langle\theta(\tau_{M-1})|(\mathrm{e}^{-\frac{\beta}{M}\hat{T}}\mathrm{e}^{-\frac{\beta}{M}\hat{V}})|\theta(\tau_0)\rangle$$

The action of $\hat{V}$ on the angle eigenstates is straight-forward. Denoting $\Delta\tau = \frac{\beta}{M}$ we obtain,

$$\exp(-\Delta\tau\hat{V})\,|\theta(\tau_j)\rangle = \exp\left(\Delta\tau t\sum_{\langle\vec{r},\vec{r}'\rangle}\cos[\theta_{\vec{r}'}(\tau_j) - \theta_{\vec{r}}(\tau_j)]\right)|\theta(\tau_j)\rangle\,. \tag{1.9}$$

Then,

$$Z = \int \mathrm{D}\theta \prod_{j=0}^{M-1} \exp\left(\Delta\tau t \sum_{\langle \vec{r},\vec{r}' \rangle} \cos[\theta_{\vec{r}'}(\tau_j) - \theta_{\vec{r}}(\tau_j)]\right) \langle \theta(\tau_j)| \exp(-\Delta\tau \hat{T}) |\theta(\tau_{j+1})\rangle \,. \quad (1.10)$$

As the kinetic energies on different sites commute, we can treat each site separately,

$$T_j = \langle \theta(\tau_j)| \exp(-\Delta\tau \hat{T}) |\theta(\tau_{j+1})\rangle \quad (1.11)$$

$$= \prod_{\vec{r}} \langle \theta(\tau_j)| \exp\left(-\frac{\Delta\tau U}{2} \frac{\partial^2}{\partial\theta^2}\right) |\theta(\tau_{j+1})\rangle \quad (1.12)$$

Let $|J^{\tau}_{\vec{r}}(\tau_j)\rangle$ be an integer-valued angular momentum eigenstate at $\vec{r}$ at τ_j. Its corresponding wavefunction in the angle eigenbasis is, $\langle \theta(\tau_j)|J^{\tau}_{\vec{r}}(\tau_j)\rangle = \exp(iJ^{\tau}_{\vec{r}}(\tau_j)\theta\vec{r}(\tau_j))$. We now insert complete sets of angular momentum states into eq. (1.12)

$$\begin{aligned} T_j &= \prod_{\vec{r}} \sum_{\{J\}} \sum_{\{J'\}} \langle \theta(\tau_j)|J_{\vec{r}}(\tau_j)\rangle \langle J_{\vec{r}}(\tau_j)| \exp\left(-\frac{\Delta\tau U}{2} \frac{\partial^2}{\partial\theta^2}\right) |J'_{\vec{r}}(\tau_j)\rangle \langle J'_{\vec{r}}(\tau_j)|\theta(\tau_{j+1})\rangle \\ &= \prod_{\vec{r}} \sum_{\{J\}} \langle \theta(\tau_j)|J_{\vec{r}}(\tau_j)\rangle \langle J_{\vec{r}}(\tau_j)|\theta(\tau_{j+1})\rangle \exp\left(-\frac{\Delta\tau U}{2} J^2_{\vec{r}}(\tau_j)\right) \\ &= \exp\left(iJ_{\vec{r}}(\tau_j)[\theta_{\vec{r}}(\tau_j) - \theta_{\vec{r}}(\tau_{j+1})]\right) \exp\left(-\frac{\Delta\tau U}{2} J^2_{\vec{r}}(\tau_j)\right). \end{aligned}$$

Therefore,

$$\begin{aligned} Z = \int \mathrm{D}\theta \prod_{j=0}^{M-1} \sum_{\{J\}} &\exp\left(\Delta\tau t \sum_{\langle \vec{r},\vec{r}' \rangle} \cos[\theta_{\vec{r}'}(\tau_j) - \theta_{\vec{r}}(\tau_j)]\right) \\ &\times \exp\left(\sum_{\vec{r}} iJ_{\vec{r}}(\tau_j)[\theta_{\vec{r}}(\tau_j) - \theta_{\vec{r}}(\tau_{j+1})]\right) \exp\left(\sum_{\vec{r}} -\frac{\Delta\tau U}{2} J^2_{\vec{r}}(\tau_j)\right). \end{aligned}$$

We have thus arrived at a representation of the partition function in terms of the classical variables $\theta_{\vec{r}}(\tau_j)$ and $J_{\vec{r}}(\tau_j)$. Now one can proceed in one of two ways. If we integrate out the angle variables $\theta_{\vec{r}}(\tau_j)$, we will obtain a so-called $J-$current model. Or, if we integrate out the integer angular momentum variables $\{J\}$, we will obtain a $d+1$ dimensional classical

model in terms of the $\theta_{\vec{r}}(\tau_j)$.

To simplify the above expression for Z, we can use Poisson summation formula,

$$\sum_{J=-\infty}^{\infty} g(J) = \sum_{m=-\infty}^{\infty} \int d\phi \mathrm{e}^{2\pi i m\phi} g(\phi). \tag{1.13}$$

Therefore, for our case,

$$\begin{aligned}
&\sum_{\{J\}} \mathrm{e}^{iJ(\tau_j)[\theta(\tau_j)-\theta(\tau_{j+1})]} \mathrm{e}^{-\Delta\tau U J^2(\tau_j)/2} \\
&= \sum_{m=-\infty}^{\infty} \int dJ \mathrm{e}^{2\pi i m J} \exp\left(-\frac{\Delta\tau U}{2} J^2(\tau_j)\right) \exp\left(iJ(\tau_j)[\theta(\tau_j)-\theta(\tau_{j+1})]\right) \\
&= \sum_{m=-\infty}^{\infty} \int dJ \exp\left(-\left(\frac{\Delta\tau U}{2} J - \frac{1}{\sqrt{2\Delta\tau U}}([\theta(\tau_j)-\theta(\tau_{j+1})] - 2\pi m)\right)^2\right) \\
&\times \exp\left(-\frac{1}{2\Delta\tau U}([\theta(\tau_j)-\theta(\tau_{j+1})] - 2\pi m)^2\right) \\
&= \sum_{m=-\infty}^{\infty} \sqrt{\frac{2\pi}{\Delta\tau U}} \exp\left(-\frac{1}{2\Delta\tau U}([\theta(\tau_j)-\theta(\tau_{j+1})] - 2\pi m)^2\right).
\end{aligned}$$

In the last step, integral over J is a Gaussian integral. We now apply the Villain approximation. The exponential of a periodic function can be approximated by a periodic sequence of narrow Gaussians,

$$\sum_{m=-\infty}^{\infty} \exp\left(-\frac{1}{2\Delta\tau U}([\theta(\tau_j)-\theta(\tau_{j+1})] - 2\pi m)^2\right) \approx \mathrm{e}^{\frac{1}{\Delta\tau U}\cos[\theta(\tau_j)-\theta(\tau_{j+1})]} \tag{1.14}$$

therefore we can write the partition function of the quantum rotor model as

$$Z = \int \mathrm{D}\theta \exp\left(\Delta\tau t \sum_{\langle \vec{r},\vec{r}' \rangle} \cos[\theta_{\vec{r}'}(\tau_j) - \theta_{\vec{r}}(\tau_j)] + \sum_{\vec{r}} \frac{1}{\Delta\tau U} \cos[\theta_{\vec{r}}(\tau_j) - \theta_{\vec{r}}(\tau_{j+1})]\right) \tag{1.15}$$

We obtain an action with additional dimension, the $\tau-$direction which represents imaginary time. The action corresponds to a $(d+1)$ dimensional classical Hamiltonian,

$$H = -\sum_{\vec{r},\vec{r}'\tau_j} J^s \cos[\theta_{\vec{r}'}(\tau_j) - \theta_{\vec{r}}(\tau_j)] - \sum_{\vec{r},\tau_j} J^\tau \cos[\theta_{\vec{r}}(\tau_j) - \theta_{\vec{r}}(\tau_{j+1})] \tag{1.16}$$

where, we define, $J^s = t\Delta\tau$ for the spatial bonds, and $J^\tau = 1/\Delta\tau U$ for the temporal bonds. The classical Hamiltonian eq. (1.16) is the well-known classical XY model. Hence we established a correspondence between d-dimensional quantum rotor model and the $d+1$ dimensional classical XY model. In the next sections we will discuss some basic properties of phase transitions and critical behavior of the classical XY model.

Quantum-classical mapping proves a very effective strategy to study equilibrium properties because powerful tools developed for classical phase transitions can be used. This has limitations when the states of mapped classical model have complex Gibbs weights, giving rise to unphysical negative probabilities. Moreover, a lot of physical properties of interest such as energy spectrum, correlation functions, etc. are related to real time functions. The mapped classical system describes imaginary time dynamics, and one can obtain real-time properties by analytic continuation. Analytic continuation is an ill-posed problem and hence it might limit the usefulness of classical analogue. As quenched disorder is time-independent, the quantum to classical mapping in disordered system produces defects which are extended along the imaginary time axis. As we will see later, this property has important implications for the critical behavior.

1.4. MEAN FIELD THEORY

Mean Field Theory (MFT) is powerful approximation method used to simplify the analysis of many-body systems. The interactions between particles are approximated by considering the effect of all other particles on any given particle as an average, or "mean field", rather than explicitly accounting for all individual interactions. We will present the example of the classical XY model to demonstrate the idea of MFT [3].

Consider a ferromagnetic classical XY model,

$$H = -J \sum_{\langle ij \rangle} \vec{S}_i \cdot \vec{S}_j = -J \sum_{\langle ij \rangle} \cos(\theta_i - \theta_j) \tag{1.17}$$

where, $\vec{S} = (\cos\theta, \sin\theta)$ is a unit vector, and $\theta \in [0, 2\pi)$. The partition function is given by

$$Z = \prod_i \int_0^{2\pi} d\theta_i \exp(-\beta H). \tag{1.18}$$

If we focus on fluctuations of one arbitrary spin $\vec{S}_i$, the local Hamiltonian can be approximated as,

$$-J\vec{S}_i \cdot \left(\sum_{\langle j \rangle} \vec{S}_j \right) \approx -J\vec{S}_i \cdot \left(\sum_{\langle j \rangle} \langle \vec{S}_j \rangle \right) \tag{1.19}$$

where the j sum is over the neighbors of site i. If all the neighbors are replaced by their average, the Hamiltonian is equivalent to that of a spin in a local field (see Fig. 1.3). This approximation is called the mean-field approximation. To formally derive the mean-field approximation, we can use a variational principle based on the Bogolibov inequality,

$$F \leq F_{\mathrm{MF}} + \langle H - H_{\mathrm{MF}} \rangle_{\mathrm{MF}}. \tag{1.20}$$

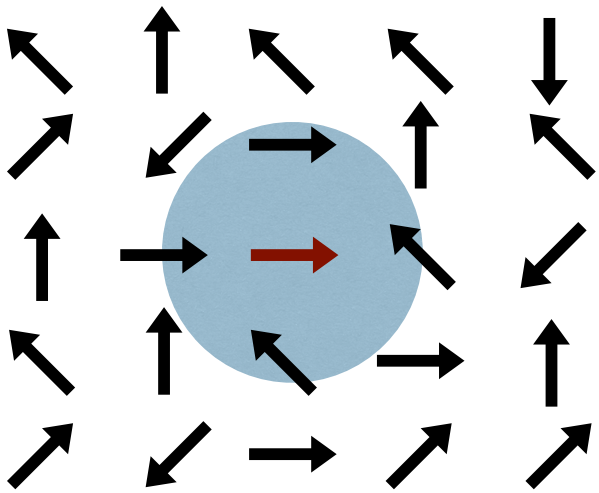

Figure 1.3. A spin experiences a local field created by its neighbors. In the mean field approximation, all the neighbor spins in the shaded area are replaced by their average value.

Here H_{MF} is a variational Hamiltonian which we take to have the form of independent spins in a field,

$$H_{\mathrm{MF}} = -\vec{h}_{\mathrm{MF}} \cdot \sum_i \vec{S}_i = -\sum_i h \cos\theta_i \tag{1.21}$$

where, without the loss of generality, we assume $\vec{h}_{\mathrm{MF}} = h\hat{x}$. The partition function reads,

$$Z_{\mathrm{MF}} = \prod_i \int_0^{2\pi} d\theta_i \exp(\beta h \cos\theta_i) = (2\pi I_0(h))^M \tag{1.22}$$

where, I_0 is a Bessel function of first kind and M is total number of spins. This yields,

$$F_{\mathrm{MF}} = -M k_B T \ln(2\pi I_0(\beta h)). \tag{1.23}$$

Magnetization $\vec{m}$ can be obtained from the free energy,

$$\vec{m} = \langle \vec{S}_i \rangle_{\mathrm{MF}} = -\frac{1}{M}\frac{\partial F_{\mathrm{MF}}}{\partial h}\hat{x} = \frac{k_B T}{2\pi I_0(\beta h)}\frac{\partial I_0(\beta h)}{\partial h}\hat{x}. \tag{1.24}$$

Now let us estimate the mean field parameter h by minimizing F_{MF} according to eq. (1.20),

$$F \leq F_{\mathrm{MF}} - J\sum_{\langle ij \rangle}\langle \vec{S}_i.\vec{S}_j \rangle_{\mathrm{MF}} + \vec{h}_{\mathrm{MF}}.\sum_i \langle \vec{S}_i \rangle_{\mathrm{MF}} \tag{1.25}$$

$$F \leq -M\ln(2\pi I_0(\beta h)) - MdJm^2 + Mhm \tag{1.26}$$

The stationarity condition,

$$\frac{\partial F}{\partial m} \leq \frac{\partial F_{\mathrm{MF}}}{\partial h}\frac{\partial h}{\partial m} - 2MdJm + Mh + Mm\frac{\partial h}{\partial m}. \tag{1.27}$$

The first and last term cancel and therefore for stationarity, $h = 2Jdm$. Substituting this in eq. (1.24), we obtain mean field equation for magnetization m,

$$m = \frac{K_B T}{4\pi J d I_0(2\beta J d m)}\frac{\partial I_0(2\beta J d m)}{\partial m}\ . \tag{1.28}$$

Similarly, mean field equations for other observables can be obtained. Let us plot the free energy from eq. (1.26) for different values of βJ. As shown in Fig. 1.4, free energy changes qualitatively at $\beta J = \beta J_c = \frac{1}{d}$. For $\beta J < \beta J_c$, F has a single minimum at $m = 0$, this is the paramagnetic phase of the XY model. For $\beta J > \beta J_c$, F has two degenerate minima at non-zero magnetization. Recall, earlier we had set $\vec{h}_{\mathrm{MF}}$, $\vec{m}$ to point along $\hat{x}$. However, this is an arbitrary choice, therefore the minimum for $\beta J > \beta J_c$, is not just doubly degenerate, but due to rotational invariance within $x - y$ plane, infinitely degenerate. If $\beta J > \beta J_c$, the system will spontaneously choose one of these equivalent minima, i.e. magnetization direction. This phenomena is called 'spontaneous symmetry breaking'.

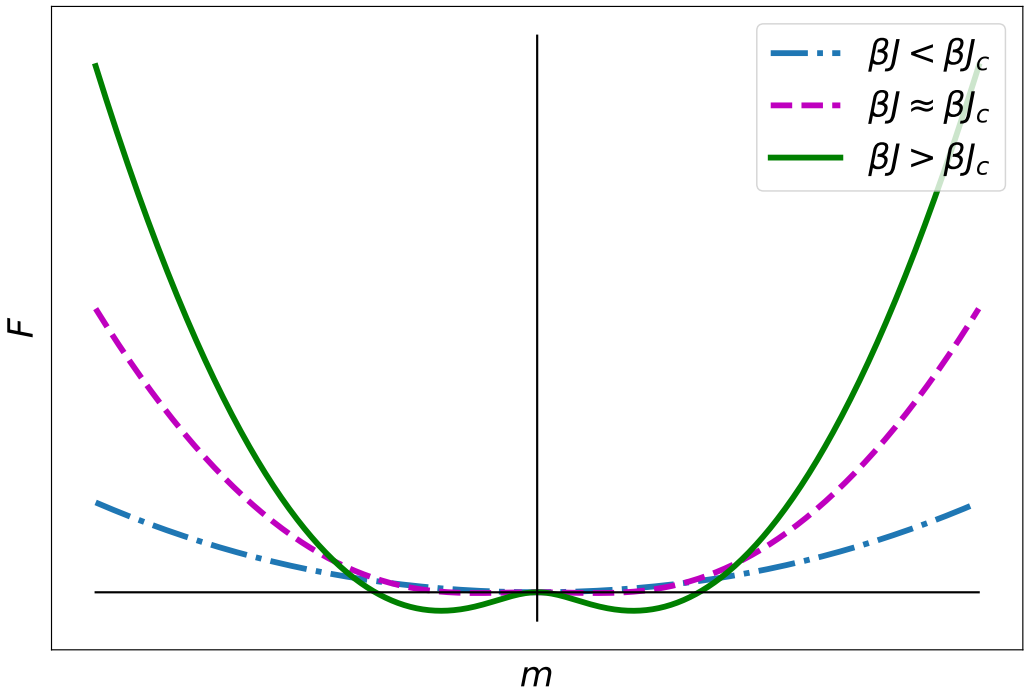

Figure 1.4. Mean-field free energy F as a function of the magnetization m, for different βJ from eq. (1.26).

1.4.1. Landau Theory. A systematic understanding of mean-field theory is due to Landau, who proposed that the free energy can be expanded in powers of the order parameter

$$F_L(m) = F_0 - hm + tm^2 + km^3 + um^4 + O(m^5). \tag{1.29}$$

Here, m is the order parameter and the coefficients h, t, k, u only depend on the external parameters (external field, temperature, pressure, etc.). For each set of external parameters, value of m can be obtained by minimizing the free energy $F_L(m)$. The Landau theory eq. 1.29 captures the universality of critical behavior between different systems and explains how symmetry of order parameter is broken spontaneously at the phase transition.

1.4.2. Landau-Ginzburg-Wilson Theory. Now we discuss Landau-Ginzburg - Wilson theory, which generalizes the above discussion [3]. So far the free energy was expressed in terms of a single spatially uniform order parameter m. However, the spins are not expected to have uniform, time-independent values. Therefore, we generalize m by introducing a continuous, coarse-grained order parameter field $\phi_\alpha(\vec{r})$ where $\alpha = 1, 2, ..., N$, and define a free energy functional $\mathcal{F}[\vec{\phi}(\vec{r})]$. A few considerations in writing $\mathcal{F}[\vec{\phi}(\vec{r})]$ are,

- if the system is invariant under $O(N)$ rotations of $\vec{\phi}(\vec{r})$, $\mathcal{F}[\vec{\phi}(\vec{r})]$ should be invariant under global rotations.
- In the vicinity of a continuous phase transition, $\vec{\phi}(\vec{r})$ is small, so expanding $\mathcal{F}[\vec{\phi}(\vec{r})]$ in a power series in $\vec{\phi}$ is justified.
- in contrast to mean-field theory, the free energy functional $\mathcal{F}$ allows spatial variations in local magnetic order and assumes that the variations occur at much larger length scale compared to lattice spacings.

Therefore, the Landau-Ginzburg-Wilson free energy functional is given by

$$\mathcal{F} = \int d^d\vec{r} \left\{ \frac{1}{2} \left[K(\nabla_{\vec{r}}\vec{\phi})^2 + t\phi^2(\vec{r}) \right] + \frac{u}{4!} \left(\phi^2(\vec{r})^2 \right) \right\}, \tag{1.30}$$

where K, t, u are nonuniversal parameters. To make comparison with earlier discussion, we first identify the expectation value of $\vec{\phi}(\vec{r})$ with magnetization,

$$\langle \vec{\phi}(\vec{r}) \rangle = \vec{m}. \tag{1.31}$$

Landau (mean-field) theory is recovered as the saddle point solution of the Landau-Ginzburg-Wilson free energy functional,

$$\frac{\delta\mathcal{F}}{\delta\phi} = \int d^d\vec{r} \left(t\langle\phi\rangle + \frac{u}{6}\langle\phi\rangle^3 \right) = 0. \tag{1.32}$$

For $t, u > 0$, $\mathcal{F}$ is minimized if $\phi(\vec{r}) = 0$. This corresponds to the paramagnetic solution. For $t < 0, u > 0$, the optimal value of $\phi(\vec{r})$ will be non-zero. The invariance of $\mathcal{F}$ under $O(N)$ rotations is also expected to be preserved by $\vec{\phi}$, therefore we have solutions that can be mapped to each other under $O(N)$ rotations. For $t < 0$, minimizing $\mathcal{F}$ gives

$$m = \sqrt{\frac{-6t}{u}}. \tag{1.33}$$

This means, as $t \to 0$, m vanishes, marking the critical point. Also, mean-field theory predicts $m \sim t^{1/2}$, i.e. irrespective of the microscopic details, exponent $1/2$ would be observed universally for all phase transitions with $O(N)$ symmetry of order parameter.

While Landau-Ginzburg-Wilson theory provides qualitative insights, it may fail to accurately predict the critical exponents. In lower dimensions, fluctuations in eq. 1.30 dominate in wider regions near critical point. The upper critical dimension d^+ is the spatial dimensionality above which the fluctuations are negligible and the Landau theory is exact. For d between the upper critical and lower critical dimension, $d^- < d < d^+$, the critical behavior is different than that of Landau theory. Finally, for $d < d^-$, fluctuations completely dominate and ordered phase does not exist [9].

1.5. UNIVERSALITY AND CRITICAL EXPONENTS

Even though Landau theory is not universally valid, the notion of power-law singularities, characterized by critical exponents applies to all (continuous) phase transitions. In this section, we define critical exponents associated with some thermodynamic observables [10]. First, define the reduced temperature t as a measure of distance from the critical temperature,

$$t = \frac{T - T_c}{T_c}. \tag{1.34}$$

The scaling hypothesis assumes that, in the vicinity of critical points, the correlation length ξ diverges as a power of $T - T_c$. Therefore we can write,

$$\xi \sim |T - T_c|^{-\nu} \tag{1.35}$$

where ν is the correlation length critical exponent. Other observables also follow power-law dependencies, allowing us to define other critical exponents. The magnetization m vanishes near T_c, at zero external field. Correspondingly the critical exponent β is defined as,

$$m \sim (T_c - T)^{\beta}. \tag{1.36}$$

The critical exponent δ is determined by the dependence of m on the external field h at the critical temperature,

$$m \sim h^{1/\delta}. \tag{1.37}$$

The magnetic susceptibility is defined as $\chi = \partial m/\partial h|_{h\to 0}$. Critical exponent associated with the behavior of χ is defined as,

$$\chi \sim |T - T_c|^{-\gamma} \tag{1.38}$$

The specific heat is defined as $C = -T(\partial^2 F/\partial T^2)_{h\to 0}$. The corresponding critical exponent at T_c is defined as,

$$C \sim (|T - T_c|)^{-\alpha} \tag{1.39}$$

Although, the critical temperature depends on the details of microscopic interactions, critical exponents are largely universal. Systems can be divided into broad groups, known as 'universality classes', such that all systems belonging to a given class have the same critical

exponents. Universality classes depend on dimensionality, and symmetries. To study the critical behavior, identification of the universality class is helpful in choosing a simple model belonging to the same class.

1.6. FINITE SIZE SCALING

At a critical point, the free energy functional is invariant under a scaling transformation, i.e. a change of length scale. The study of scaling transformations on the free energy is the subject of 'renormalization group theory'. The concepts of universality, scaling laws and critical exponents can be derived using the renormalization group (as was done when they were discovered in the 1960s and 1970s)[11, 12]. Here, we proceed by treating them as phenomenological hypotheses. Close to a critical point, the correlation length ξ is the only relevant length scale. Therefore, physics remains the same even after rescaling the system as,

$$x \longrightarrow x' = \frac{x}{b}$$

(Here b is the rescaling factor for the position variable x), provided the external parameters are adjusted such that ξ remains unchanged. The condition of statistical similarity under scaling is,

$$\mathrm{Tr}(\mathrm{e}^{-\beta H}) = \mathrm{Tr}'(\mathrm{e}^{-\beta H'}) \tag{1.40}$$

where prime indices are for the scaled system. This procedure maps couplings of the Hamiltonian $\{t, h\}$ to a new set of couplings $\{t', h'\}$, such that free energy density fulfills, $F(t, h) = b^{-d} F(t', h')$. This mapping represents flows in the parameter space. We will now investigate scaling in a system with linear size L. From eq. (1.35)and (1.39), specific heat in the vicinity of critical point, $C \sim \xi^{\frac{\alpha}{\nu}}$. For a finite system, the correlation length ξ cannot exceed L. As a result, specific heat C would be bounded from above. The specific heat follows a scaling form,

$$C(t, L^{-1}) = t^{-\alpha} X_C(L^{-1} t^{-\nu}) \tag{1.41}$$

$$C(t, L^{-1}) = t^{-\alpha}(L^{-1}t^{-\nu})^{\frac{-\alpha}{\nu}} Y_C(tL^{1/\nu}) \tag{1.42}$$

$$C(t, L^{-1}) = L^{\frac{\alpha}{\nu}} Y_C(tL^{1/\nu}) \tag{1.43}$$

where, $Y_C(x)$ is a new scaling function with a maximum at $x = x^*$. Therefore, the specific heat peak occurs at a reduced temperature shifted from that of the infinite system by amount,

$$t_L = x^*/L^{1/\nu} \propto L^{-1/\nu}. \tag{1.44}$$

The maximum of the specific heat is,

$$C(t_L, L^{-1}) = L^{\alpha/\nu} Y_C(x^*) \propto L^{\alpha/\nu} \tag{1.45}$$

In the later sections we will use this effect to estimate asymptotic critical temperature and critical exponents from the Monte Carlo simulation of finite systems. Analogous scaling forms can be derived for other observables.

1.7. DISORDER EFFECTS ON CRITICAL BEHAVIOR

Disorder is ubiquitous in condensed matter systems. Imperfections in the form of vacancies, impurity atoms, or extended defects are unavoidable in practice. Although the random nature of disorder might be difficult to treat using theoretical methods, disorder leads to a new set of emergent phenomena, which are impossible to realize in clean systems. In this section we will develop qualitative ideas related to effects of disorder on critical behavior.

1.7.1. Harris Criterion. A system with disorder is by nature inhomogeneous. It is therefore not a priory known whether it can show singular behavior at a specific critical point. As disorder varies from point to point, there will be spatial regions which are

away from the critical point, even if the macroscopically the system is at the critical point. Whether the critical point of a clean system is stable under the introduction of weak disorder was studied by Harris. Here we present a simple argument for the Harris criterion [13].

Consider a sub-region of size L, marked by an index r. We can define a critical temperature of this region, $T_{c,r}$, which generally will be different than the global critical temperature T_c. From a central limit theorem, local fluctuations will cause variations in $T_{c,r}$ of order $L^{-d/2}$. Such a deviation is significant if it is of the order $|T - T_c|$. Therefore, for length scales shorter than $L = L_r \sim |T - T_c|^{-2/d}$, deviations are significant. Now if L_r is smaller than the correlation length, as critical point is approached, and $\xi \sim |T - T_c|^{-\nu}$, the local fluctuations will be averaged out. Thus, the stability requirement is, $L \ll \xi$, i.e.

$$|T - T_c|^{-2/d} \ll |T - T_c|^{-\nu}. \tag{1.46}$$

This leads to the Harris criterion,

$$d\nu \geq 2. \tag{1.47}$$

If the above inequality is violated, then the critical behavior is disorder dependent. Critical behavior in disordered systems can be understood based on three cases [14],

1. If Harris criterion eq (1.47) is satisfied, the disorder strength goes to zero under coarse graining. The critical behavior is that of the clean system.

2. If eq (1.47) is violated, there are two possibilities

   (a) In this case, under coarse graining, if the system remains inhomogeneous and the disorder strength approaches a finite constant. The critical behavior is governed by conventional power-laws, but the critical exponents differ from the clean version.

Table 1.1. Classification of critical points in the presence of random-T_c disorder [9, 14].

RR dimension	Harris criterion	Griffiths singularities	Critical behavior
$d_{\mathrm{RR}} < d^-$	$d\nu > 2$	weak	clean
$d_{\mathrm{RR}} < d^-$	$d\nu < 2$	weak	conventional
$d_{\mathrm{RR}} = d^-$	$d\nu > 2$	power-law, z' finite	clean
$d_{\mathrm{RR}} = d^-$	$d\nu < 2$	power-law, z' diverges	infinite disorder
$d_{\mathrm{RR}} > d^-$		RR freeze	smeared transition

(b) Finally, disorder strength goes to infinity at the large length scales. As a result of infinite randomness, critical points show unconventional activated scaling behavior. Intsead of power-law relation, correlation length and imaginary time are related by an exponential relation.

1.7.2. Rare Regions and Griffiths-McCoy Singularities. Now we will discuss the effects of rare strong disorder fluctuations on phase transitions. As an example consider the case of a dilute ferromagnet. Due to statistical fluctuations, there may exist a large disorder-free region. If the system overall is close to the critical temperature in the paramagnetic phase, this disorder free region would already be in the symmetry broken, ordered phase. It would thus make a large contribution to thermodynamic quantities. Singularities in the free energy caused by the rare regions are called Griffiths singularities.

Rare regions play a significant role if they change the behavior of thermodynamic obsevables. The probability for forming a rare region of size L_{RR} is exponentially small, $p(V_{\mathrm{RR}}) \sim \exp(-aV_{\mathrm{RR}})$, where V_{RR} is the volume of the rare region. One can imagine each rare region as a superspin, whose magnetic moment is proportional to the volume V_{RR}. Then the magnetic susceptibility $\chi(V_{\mathrm{RR}}) \sim V_{\mathrm{RR}}^2/T$. Thus, χ increases quadratically, while the probability $p(V_{\mathrm{RR}})$ decreases exponentially with the volume of rare region. In the thermodynamic limit, such Griffiths singularity will practically be unobsevable.

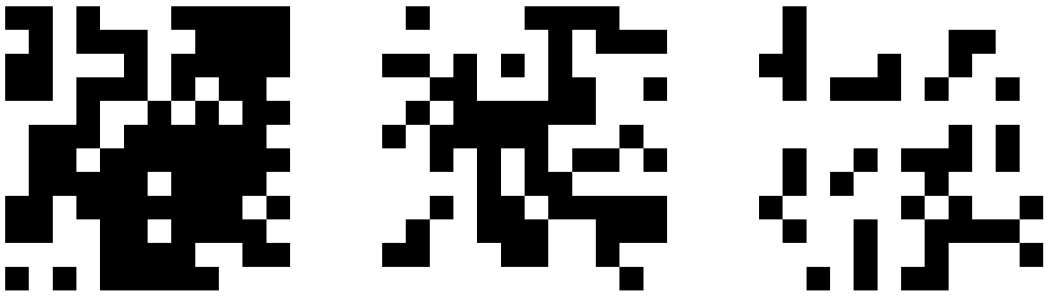

(a) $p = 0.3$ (b) $p = p_c \approx 0.59$ (c) $p = 0.7$

Figure 1.5. Example of site percolation on 12×12 square lattice, for various dilution p. Empty sites are denoted by white squares and occupied sites by black squares.

However, there are situations when the contribution of a rare region to the obsevables increases exponentially with its volume. The presence of rare regions in quantum systems might result in gapped spectrum, which leads to large response in susceptibility. Also, classical systems with extended defects have higher probabilities of forming rare regions, and might show stronger Griffiths singularities. The connection between rare regions and Harris criterion has been studied in the literature and a classification criterion similar to Harris is shown in the table 1.1.

1.7.3. Percolation Theory. Percolation theory studies the behavior of connected clusters in a random network or lattice. By adding or removing system components, one can study the changes in the connectivity. Figure 1.5 shows an example of a square lattice, where the probability of any given site to be unoccupied is denoted by p. A cluster is defined as a set of lattice sites which are connected by an edge. As p is increased, the number of finite clusters increases. The critical probability after which an infinite cluster (i.e. a cluster spanning the entire system in the infinite system limit) disappears, is called the percolation threshold p_c. For a square lattice $p_c \approx 0.59$[15]. Near the critical point p_c, many system properties follow power-law scaling, therefore the system is said to undergo a percolation phase transition at p_c.

Here, we will study the effects of percolation on dilute magnets at low temperatures. Consider a classical site-diluted Hamiltonian,

$$H = -J \sum_{\langle i,j \rangle} \epsilon_i \epsilon_j S_i S_j \tag{1.48}$$

where the presence or absence of the spin at a site is denoted using the variable ϵ,

$$\epsilon = \begin{cases} 0 & \text{with probability } p \\ 1 & \text{with probability } 1-p. \end{cases}$$

In the clean system, i.e. $p = 0$, phase transition occurs at T_c. As dilution p increases, the critical temperature decreases. The two distinct phases, magnetic order and thermal paramagnet, are separated by the phase boundary $T_c(p)$. Now, for high dilutions $p > p_c$, the system consists of finite disconnected clusters. At low temperatures, each of these clusters can independently prefer up or down orientation, resulting in net zero magnetization. Therefore, the magnetic order cannot exist for $p > p_c$. A schematic phase diagram is shown in Fig. 1.6.

1.8. TOPOLOGICAL PHASE TRANSITION

So far we studied the phase transitions according to Landau's paradigm, where the symmetry of an order parameter is broken at the phase transition. These concepts can be extended to include zero-temperature quantum phase transitions. However there are other phase transitions that are not associated with broken symmetry and do not have an identifiable order parameter. These phase transitions are driven by topological defects and called topological phase transitions. Topological phase transitions can be accompanied by

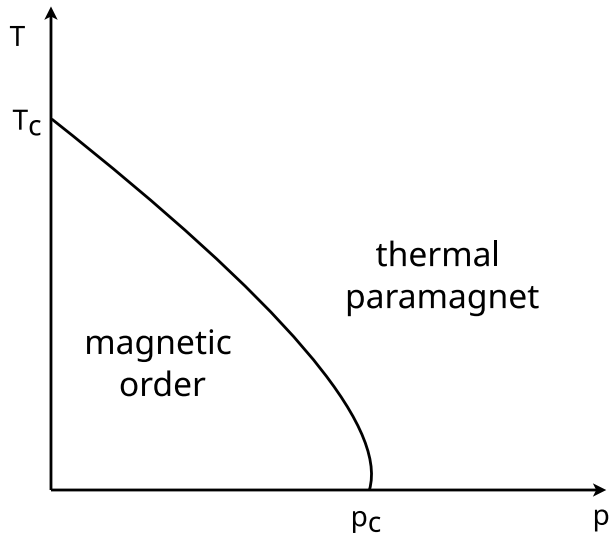

Figure 1.6. Schematic phase diagram of a dilute magnet. As dilution p is increased, critical temperature decreases. At zero temperature, phase transition occurs at critical dilution p_c, called percolation threshold.

singularities in thermodynamic properties and diverging correlation length, and the concepts of scaling relations, universality, critical exponents are still applicable near topological phase transitions.

Early experiments on $2d$ Helium films provided evidence of a superfluid transition. However, according to the Mermin-Wagner theorem, long-range ordered superfluidity is prohibited in this system [4]. The Mermin-Wagner theorem states that, in dimension $d \leq 2$, continuous symmetries cannot be spontaneously broken at finite temperatures. In 1972-73, Berezinskii, Kosterlitz, and Thouless explained the superfluid transition in Helium films using topological defects [5, 6].

In this section we will discuss the topological phase transition in the $2d$ classical XY model. First we show that there exists a phase transition at finite temperature by comparing the asymptotic behavior at high temperature and low temperature expansions of the partition

function. The Hamiltonian of the 2d square lattice XY model reads,

$$H = -J \sum_{\langle ij \rangle} \cos(\theta_i - \theta_j), \tag{1.49}$$

where we used the parametrization of the spins, $\mathbf{S} = (\cos\theta, \sin\theta)$. The partition function is given by,

$$Z = \int_0^{2\pi} \prod_i \frac{d\theta_i}{2\pi} e^{-\beta H} = \int_0^{2\pi} \prod_i \frac{d\theta_i}{2\pi} e^{K \sum_{\langle ij \rangle} \cos(\theta_i - \theta_j)}, \tag{1.50}$$

where, $K = \beta J$. At high temperatures, we can expand Z in powers of K,

$$Z = \int_0^{2\pi} \prod_i \frac{d\theta_i}{2\pi} \prod_{\langle ij \rangle} [1 + K\cos(\theta_i - \theta_j) + O(K^2)]. \tag{1.51}$$

Each term in the product can be considered as a bond between sites i and j. As $\int_0^{2\pi} d\theta_1 K \cos(\theta_1 - \theta_2) = 0$, all the contributions coming from a single bond are zero. Further, because $\int_0^{2\pi} d\theta_2 K \cos(\theta_1 - \theta_2)\cos(\theta_2 - \theta_3) = K\cos(\theta_1 - \theta_3)/2$, only non-vanishing contributions to the partition function arise from closed loops that encircle a single plaquette. Now we can use the partition function to evaluate spin-spin correlations then read,

$$\langle \mathbf{S}_{\vec{r}} . \mathbf{S}_{\vec{r}'} \rangle = \langle \cos(\theta_{\vec{r}} - \theta_{\vec{r}'}) \rangle. \tag{1.52}$$

First consider the case that the two sites are nearest neighbors. The only non-zero contribution comes from the bond between two sites, i.e. $\int_0^{2\pi} d\theta_0 K \cos^2(\theta_{\vec{r}} - \theta_0) = K/2$. See Fig. 1.7. Therefore, the leading contribution to correlation function is from all the sites that lie on the paths joining origin to $\vec{r}$,

$$\langle \mathbf{S}_{\vec{r}} . \mathbf{S}_{\vec{r}'} \rangle = \left(\frac{K}{2}\right)^{|\vec{r} - \vec{r}'|} \sim \exp\left(-\frac{|\vec{r} - \vec{r}'|}{\xi}\right) \tag{1.53}$$

with correlation length $\xi^{-1} = \ln(2/K)$. This exponential decay of correlation means the high temperature phase is paramagnetic.

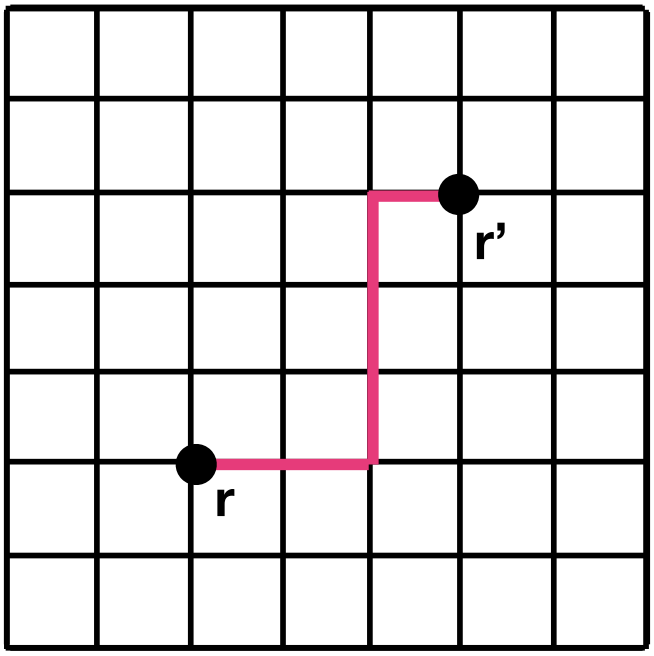

Figure 1.7. Bonds that contribute in evaluation of spin-spin correlation function in eq. (1.52).

Conversely, at the zero temperature, the ground state configuration corresponds to all spins aligned parallel to each other. The thermal fluctuations at very low temperatures would cause small perturbation in the angles θ. At large distances, we can treat these perturbations in a continuum limit as long-wavelength excitations. Therefore,

$$-\beta H = K \sum_{\langle ij \rangle} \mathbf{S}_i . \mathbf{S}_j = \frac{K}{2} \sum_{\langle ij \rangle} \left[(\mathbf{S}_i - \mathbf{S}_j)^2 - 2 \right] \tag{1.54}$$

$$-\beta H = \frac{K}{2} \int d^2\vec{r} (\nabla\theta)^2 - \beta E_0. \tag{1.55}$$

Ignoring the constant background energy,

$$Z = \int_{-\infty}^{\infty} D\theta \exp\left(\frac{K}{2} \int d^2\vec{r} (\nabla\theta)^2 \right), \tag{1.56}$$

where limits of integration can be extended to infinity because angular fluctuations are expected to be very small. Spin-spin correlation,

$$\langle \mathbf{S}_{\vec{r}}.\mathbf{S}_{\vec{r}'} \rangle = \langle e^{i[\theta_{\vec{r}} - \theta_{\vec{r}'}]} \rangle = e^{-\frac{1}{2}\langle(\theta_{\vec{r}} - \theta_{\vec{r}'})^2\rangle} \tag{1.57}$$

where second equality holds because Z is Gaussian. Evaluating the exponent in Fourier basis, $\langle|\theta(q)|^2\rangle = \frac{1}{Kq^2}$. Inverse Fourier transform gives us,

$$\langle(\theta_{\vec{r}} - \theta_{\vec{r}'})^2\rangle = \frac{1}{2\pi K} \ln\left(\frac{|\vec{r} - \vec{r}'|}{a}\right). \tag{1.58}$$

Therefore, spin-spin correlation,

$$\langle \mathbf{S}_{\vec{r}}.\mathbf{S}_{\vec{r}'} \rangle = \left(\frac{|\vec{r} - \vec{r}'|}{a}\right)^{-\frac{1}{2\pi K}} \sim |\vec{r} - \vec{r}'|^{-\eta}. \tag{1.59}$$

The spin-spin correlation goes to 0 as $r \to \infty$, i.e. there is no long-range order. However, compared to exponential decay at high temperatures, this power law decay is much slower. This distinction at the two asymptotic limits allows the possibility of phase transition at finite temperature. The mechanism of the phase transition was explained by Berezinskii, Kosterlitz and Thouless using vortex-antivortex pair unbinding. Lets discuss some features of the vortices below.

In the long-wavelength approximation in eq. (1.56), the contribution from singular spin configurations such as vortices was neglected. A vortex has the property that a closed loop integral,

$$\oint d\vec{r}.\nabla\theta = 2\pi n \Rightarrow \nabla\theta = \frac{n}{r}\hat{\mathbf{e}}_r \times \hat{\mathbf{e}}_z, \tag{1.60}$$

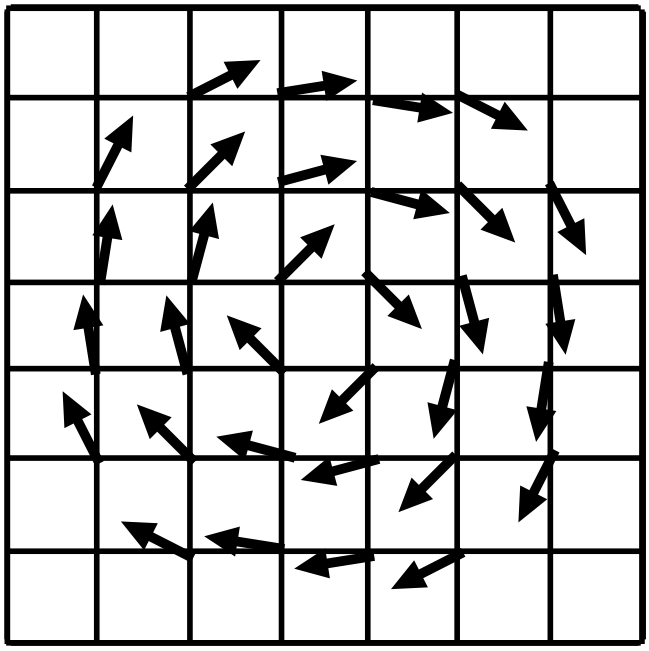

Figure 1.8. A vortex with winding number $n = 1$.

where n is an integer, called the winding number, $\hat{\mathbf{e}}_r, \hat{\mathbf{e}}_z$ are unit vectors in-plane and perpendicular to the plane of spins respectively. See Fig. 1.8. The energy of a vortex of winding number n, placed at the origin,

$$E_n = E_n^0(a) + \frac{J}{2}\int (\nabla\theta)^2 d^2r = E_n^0(a) + \frac{J}{2}\int \frac{n^2}{r^2} d^2r \tag{1.61}$$

$$E_n = E_n^0(a) + \pi J n^2 \ln\left(\frac{L}{a}\right). \tag{1.62}$$

$E_n^0(a)$ is energy of a core of size a, and L is the linear size of the system. Therefore, energy of a single vortex of winding number unity in an infinite system diverges. However, energy of a pair of vortices with opposite winding numbers separated by distance r,

$$E_{\text{pair}}(r) = 2\pi J n^2 \ln\left(\frac{r}{a}\right). \tag{1.63}$$

Thus, a bound vortex-antivortex pair costs finite energy. Kosterlitz and Thouless suggested that bound pairs of vortices are present at low temperature, and as temperature increases proliferation of unbound vortices drives the system to disordered phase. To understand this mechanism, consider free energy change to add a vortex. A vortex of core size a can be placed at $(L/a)^2$ locations, therefore entropy of a single vortex,

$$S_1 = k_B \ln\left(\frac{L^2}{a^2}\right) = 2k_B \ln\left(\frac{L}{a}\right). \tag{1.64}$$

Then free energy,

$$F_1 = (\pi J - 2k_B T) \ln\left(\frac{L}{a}\right). \tag{1.65}$$

As already discussed, free energy cost to add a vortex at low temperature diverges as $L \to \infty$, but at temperatures above T_c, free energy is lowered by adding a vortex,

$$T_c = \frac{\pi J}{2k_b}. \tag{1.66}$$

This simple estimate provides a qualitative argument for the phase transition. Including more vortices and interactions between them is necessary to understand the full picture.

1.9. OUTLINE OF THE DISSERTATION

In this dissertation, we will present results regarding phase transitions in three closely related systems. In PAPER I, we investigate the behavior of diluted hexaferrites with varying levels of dilution. We study the unusual phase diagram observed in experiments on hexaferrite materials through a percolation scenario, using large-scale Monte Carlo simulations. Next, in PAPER II, we examine the response of the two-dimensional XY model to a finite twist in the boundary conditions. We explain the unexpected deviation observed in the free energy difference between periodic and twisted boundary conditions. These results are relevant in certain experimental contexts and for computational methods.

Then, in PAPER III, we explore the phase diagram of the disordered quantum clock model in one dimension. We characterize the critical behavior across all phase boundaries and verify theoretical predictions in the strong disorder limit.

The summary and implications of this work are presented in the final section.

PAPER

I. PHASE BOUNDARY NEAR A MAGNETIC PERCOLATION TRANSITION

Gaurav Khairnar, Cameron Lerch, Thomas Vojta
Department of Physics
Missouri University of Science and Technology
Rolla, Missouri 65409
Email: grktmk@mst.edu, vojtat@mst.edu[2]

ABSTRACT

Motivated by recent experimental observations [Phys. Rev. **96**, 020407 (2017)] on hexagonal ferrites, we revisit the phase diagrams of diluted magnets close to the lattice percolation threshold. We perform large-scale Monte Carlo simulations of XY and Heisenberg models on both simple cubic lattices and lattices representing the crystal structure of the hexagonal ferrites. Close to the percolation threshold p_c, we find that the magnetic ordering temperature T_c depends on the dilution p via the power law $T_c \sim |p - p_c|^\phi$ with exponent $\phi = 1.09$, in agreement with classical percolation theory. However, this asymptotic critical region is very narrow, $|p - p_c| \lesssim 0.04$. Outside of it, the shape of the phase boundary is well described, over a wide range of dilutions, by a nonuniversal power law with an exponent somewhat below unity. Nonetheless, the percolation scenario does not reproduce the experimentally observed relation $T_c \sim (x_c - x)^{2/3}$ in $PbFe_{12-x}Ga_xO_{19}$. We discuss the generality of our findings as well as implications for the physics of diluted hexagonal ferrites.

[2]Published: The European Physical Journal B, 94, 43 (2021)

1. INTRODUCTION

Disordered many-body systems feature three different types of fluctuations, viz., static random fluctuations due to the quenched disorder, thermal fluctuations, and quantum fluctuations. Their interplay can greatly affect the properties of phase transitions, with possible consequences ranging from a simple change of universality class [16] to exotic infinite-randomness criticality [17, 18], classical [19] and quantum [20, 21] Griffiths singularities, as well as the destruction of the transition by smearing [22, 23, 24, 25]. Recent reviews of some of these phenomena can be found in Refs. [14, 26, 27]. Randomly diluted magnetic materials are a particularly interesting class of systems in which the above interplay is realized. Here, the disorder fluctuations correspond to the geometric fluctuations of the underlying lattices which can undergo a geometric percolation transition between a disconnected phase and a connected (percolating) phase [7].

Recently, the behavior of diluted magnets close to the percolation transition has reattracted attention because of the unexpected shape of the phase boundary observed in the diluted hexagonal ferrite (hexaferrite) $PbFe_{12-x}Ga_xO_{19}$ [1]. Pure $PbFe_{12}O_{19}$ orders ferrimagnetically at temperatures below about 720 K [28]. The ordering temperature T_c can be suppressed by randomly substituting nonmagnetic Ga ions for Fe ions in $PbFe_{12-x}Ga_xO_{19}$. It vanishes when x reaches the critical value $x_c \approx 8.6$. This value is very close the percolation threshold $x_p = 8.846$ of the underlying lattice[3], suggesting that the transition at x_c is of percolation type [1]. Remarkably, the phase boundary follows the power law $T_c(x) = T_c(0)(1 - x/x_c)^\phi$ with $\phi = 2/3$ over the entire x-range from 0 to x_c. This disagrees with the prediction from classical percolation theory [7, 29] which yields a crossover exponent of $\phi > 1$ for continuous symmetry magnets, at least for dilutions close to x_c.

In this paper, we therefore reinvestigate the phase boundary close to the percolation transition of diluted classical planar and Heisenberg magnets by means of large-scale Monte Carlo simulations. The purpose of the paper is twofold. First, we wish to test and verify

[3]The lattice in question is the lattice of exchange interactions between the Fe ions.

the percolation theory predictions, focusing not only on the asymptotic critical behavior but also on the width of the critical region and the preasymptotic properties. Second, we wish to explore whether the classical percolation scenario can explain the experimental observations in $PbFe_{12-x}Ga_xO_{19}$ [1].

Our paper is organized as follows. In Sec. 2, we introduce the diluted XY and Heisenberg models and discuss their qualitative behavior. Section 3 summarizes the predictions of percolation theory. Our Monte Carlo simulation method is described in Sec. 4. Sections 5.1 and 5.2 report our results for model systems on cubic lattices and for systems defined on the hexagonal ferrite lattice, respectively. We conclude in Sec. 6.

2. THE MODELS

Consistent with the dual purpose of studying the critical behavior of the phase boundary close to a magnetic percolation transition and of addressing the experimental observations in diluted hexaferrites [1], we consider two models, viz., (i) site-diluted classical XY and Heisenberg models on simple cubic lattices and (ii) a classical Heisenberg Hamiltonian based on the hexaferrite crystal structure using realistic exchange interactions. Comparing the results of these different models will also allow us to explore the universality of the critical behavior.

2.1. SITE-DILUTED XY AND HEISENBERG MODELS ON CUBIC LATTICES

We consider a simple cubic lattice of $N = L^3$ sites. Each site is either occupied by a vacancy or by a classical spin, i.e., an n-component unit vector $\mathbf{S}_i$ ($n = 2$ for the XY model and $n = 3$ for the Heisenberg case). The Hamiltonian reads

$$H = -J \sum_{<i,j>} \epsilon_i \epsilon_j \mathbf{S}_i \cdot \mathbf{S}_j \ . \tag{1}$$

Here, the sum is over pairs of nearest-neighbor sites, and $J > 0$ denotes the ferromagnetic exchange interaction. (In the following, we set J to unity for the cubic lattice simulations.) The quenched independent random variables ϵ_i implement the site dilution. They take the values 0 (vacancy) with probability p and 1 (occupied site) with probability $1 - p$. We employ periodic boundary conditions. Magnetic long-range order can be characterized by the order parameter, the total magnetization

$$\mathbf{m} = \frac{1}{N} \sum_i \mathbf{S}_i \ . \tag{2}$$

The qualitative behavior of this model as a function of temperature T and dilution p is well understood (see, e.g., Ref. [30] for an overview). For sufficiently small dilution, the system orders magnetically below a critical temperature $T_c(p)$. The critical temperature decreases continuously with p until it reaches zero at the percolation threshold p_c of the lattice. For dilutions beyond the percolation threshold, magnetic long-range order is impossible because the system breaks down into finite noninteracting clusters. The point $p = p_c, T = 0$ is a multicritical point at which both the geometric fluctuations of the lattice and the thermal fluctuations become long-ranged.

2.2. HEXAFERRITE HEISENBERG MODEL

$PbFe_{12}O_{19}$ crystallizes in the magnetoplumbite structure, as illustrated in Fig. 1. A double unit cell contains 24 Fe^{3+} ions in five distinct sublattices; they are in the spin state $S = 5/2$. Below a temperature of about $720K$, the material orders ferrimagnetically, with 16 of the Fe spins pointing up and the remaining 8 Fe ions pointing down [28]. Note that the high critical temperature and the high spin value suggest that a classical description should provide a good approximation.

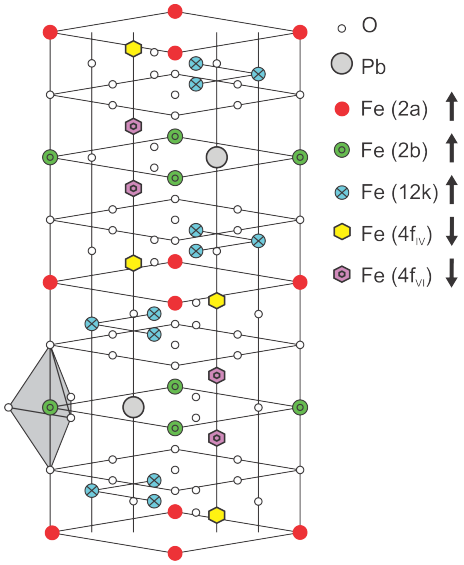

Figure 1. Double unit cell of $PbFe_{12}O_{19}$. 24 Fe^{3+} ions are located on five distinct sublattices.

In $PbFe_{12-x}Ga_xO_{19}$, the randomly substituted Ga ions, which replace the Fe ions, act as quenched spinless impurities. To model this system, we start from the hexaferrite crystal structure and randomly place either a vacancy (with probability p) or a classical Heisenberg spin $\mathbf{S}_i$ (with probability $1-p$) at each Fe site. The dilution p is related to the number x of Ga ions in the unit cell by $p = x/12$. The Hamiltonian reads

$$H = -\sum_{i,j} J_{ij}\epsilon_i\epsilon_j\mathbf{S}_i\mathbf{S}_j \ . \tag{3}$$

The quenched random variables ϵ_i distinguish vacancies and spins, as before. The values of the exchange interactions J_{ij} stem from the density functional calculation in Ref. [31]; they are scaled by a common factor to approximately reproduce the critical temperature $T_c = 720K$ of the undiluted material. In most of our Monte Carlo simulations, we include only the leading (strongest) interactions which are between the following sublattice pairs:

2a-4f$_{IV}$, 2b-4f$_{VI}$, 12k-4f$_{IV}$, 12k-4f$_{VI}$. These interactions are non-frustrated and establish the ferrimagnetic order. We also perform a few test calculations to explore the effects of additional couplings which are significantly weaker but frustrate the ferrimagnetic order.

The qualitative features of the phase diagram of the model (3) are expected to be similar to those discussed in the previous section. With increasing dilution p, the critical temperature $T_c(p)$ is continuously suppressed and reaches zero at the site percolation threshold. The value of the percolation threshold of the lattice spanned by the leading non-frustrated interactions between the Fe ions was determined in Ref. [1] by means of Monte Carlo simulations. They yielded $p_c = 0.7372(5)$, corresponding to $x_c = 8.846(6)$ Ga ions per unit cell. (The numbers in brackets show the error estimate of the last digit.)

3. PREDICTIONS OF PERCOLATION THEORY

In this section, we briefly summarize the predictions of classical percolation theory for the shape of the phase boundary $T_c(p)$ close to multicritical point $p = p_c, T = 0$ [7, 29, 32]. Close to this point, two length scales are at play, the percolation correlation length, ξ_p which characterizes the size of finite isolated clusters of lattice sites and the magnetic thermal correlation length on the critical infinite percolating cluster at p_c denoted by ξ_T. The percolation correlation length ξ_p diverges as $\xi_p \sim |p - p_c|^{-\nu_p}$ as the percolation threshold is approached. The magnetic thermal correlation length behaves as $\xi_T \sim T^{-\nu_T}$ for continuous-symmetry magnets described by the n-vector model with $n > 1$.

To find the phase boundary, consider the magnetization near the critical point. It fulfills the scaling form,

$$m(p - p_c, T) = |p - p_c|^{\beta} \, X\left(\xi_T/\xi_p\right). \tag{4}$$

For $p < p_c$, the magnetic phase transition occurs at a particular value x_c of the argument of the scaling function X. At the magnetic transition, we therefore have $\xi_T = x_c \xi_p$. This yields the power law relation

$$T_c(p) \sim |p - p_c|^{\phi} \, . \tag{5}$$

The crossover exponent ϕ takes the value $\phi = \nu_p/\nu_T$. (In contrast, ξ_T diverges exponentially, $\xi_T \sim (e^{-2J/T})^{-\nu_T}$, for Ising magnets, leading to a logarithmic dependence $T_c(p) \sim \ln^{-1}(1/|p - p_c|)$.)

Using a renormalization group calculation, Coniglio [29] established the relation $\nu_T = 1/\tilde{\zeta}_R$. Here, $\tilde{\zeta}_R$ characterizes the resistance R of a random resistor network on a critical percolation cluster of linear size L via $R \sim L^{\tilde{\zeta}_R}$.

The exponent $\tilde{\zeta}_R$ can be related to the well-known conductivity critical exponent t which describes how the conductivity σ of the resistor network depends on the distance from the percolation threshold, $\sigma \sim |p - p_c|^t$. To do so, consider a resistor network on a percolating lattice close to p_c but on the percolating side. Its behavior is critical for clusters of size less than ξ_p and Ohmic for sizes beyond ξ_p. For a d-dimensional system of linear size $L \gg \xi_p$, we can employ Ohm's law to combine blocks of size ξ_p, yielding

$$R(L) = R(\xi_p) \left(\frac{L}{\xi_p}\right) \left(\frac{L}{\xi_p}\right)^{-(d-1)} \sim \xi_p^{\tilde{\zeta}_R} \xi_p^{d-2} L^{2-d} \, . \tag{6}$$

The conductivity on the percolating side thus behaves as $\sigma \sim \xi_p^{-(d-2+\tilde{\zeta}_R)} \sim |p-p_c|^{\nu_p(d-2+\tilde{\zeta}_R)}$. Thus, we obtain the hyperscaling relation, $t = (d - 2 + \tilde{\zeta}_R)\nu_p$ or $\tilde{\zeta}_R = t/\nu_p - d + 2$. Using the numerical estimates $t/\nu_p = 2.28(2)$ and $\nu_p = 0.876(2)$ [33, 34] for three-dimensional systems yields $\tilde{\zeta}_R = 1.28(2)$, predicting a crossover exponent of $\phi = \nu_p/\nu_T = \nu_p \tilde{\zeta}_R = 1.12(2)$. [4]

[4] The crossover exponent has also been computed within an expansion in powers of $\epsilon = 6 - d$ yielding $\phi = 1 + \epsilon/42$ to first order in ϵ [35, 36]. The resulting value, $\phi = 1.071$, is surprisingly close to the best numerical estimate $\phi = 1.12(2)$.

4. NUMERICAL SIMULATIONS

4.1. MONTE CARLO METHOD

To find the critical temperature for a given dilution of the system, we perform large-scale Monte Carlo (MC) simulations. These simulations employ the Wolff [37] and Metropolis [38] algorithms. Specifically, a full MC sweep consists of a Wolff sweep followed by a Metropolis sweep. The Wolff algorithm is a cluster-flip algorithm which is beneficial in reducing critical slowing down of the system near criticality. The Metropolis algorithm is a single spin-flip algorithm. It is required to achieve equilibration of small isolated clusters of lattice sites which might form as a result of dilution.

For the cubic lattice calculations, we consider system sizes ranging from $L^3 = 10^3$ to $L^3 = 112^3$. We have simulated $4000 - 40000$ independent disorder configurations for each size. For the hexaferrite lattice, we simulate systems consisting of 10^3 to 40^3 double unit cells (each double unit cell contains 24 Fe sites) using $100 - 300$ independent disorder configurations for each size. All physical quantities of interest, such as energy, magnetization, correlation length, etc. are averaged over the disorder configurations. Statistical errors are obtained from the variations of the results between the configurations.

Measurements of observables must be performed after the system reaches thermal equilibrium. We determine the number of Monte Carlo sweeps required for the system to equilibrate by comparing the results of runs with hot starts (for which the spins initially point in random directions) and with cold starts (for which all spins are initially aligned). An example of such a test for a cubic lattice XY system close to multicritical point is shown in Fig. 2. The energy and order parameter attain their respective equilibrium values after roughly 50 Monte Carlo sweeps. Similar numerical checks were performed for other parameter values as well as for the cases of Heisenberg spins on cubic and hexaferrite lattices. Based on these tests, we have chosen 150 equilibration sweeps (using a hot start) and 500 measurement sweeps per disorder configuration for the cubic lattice simulations.

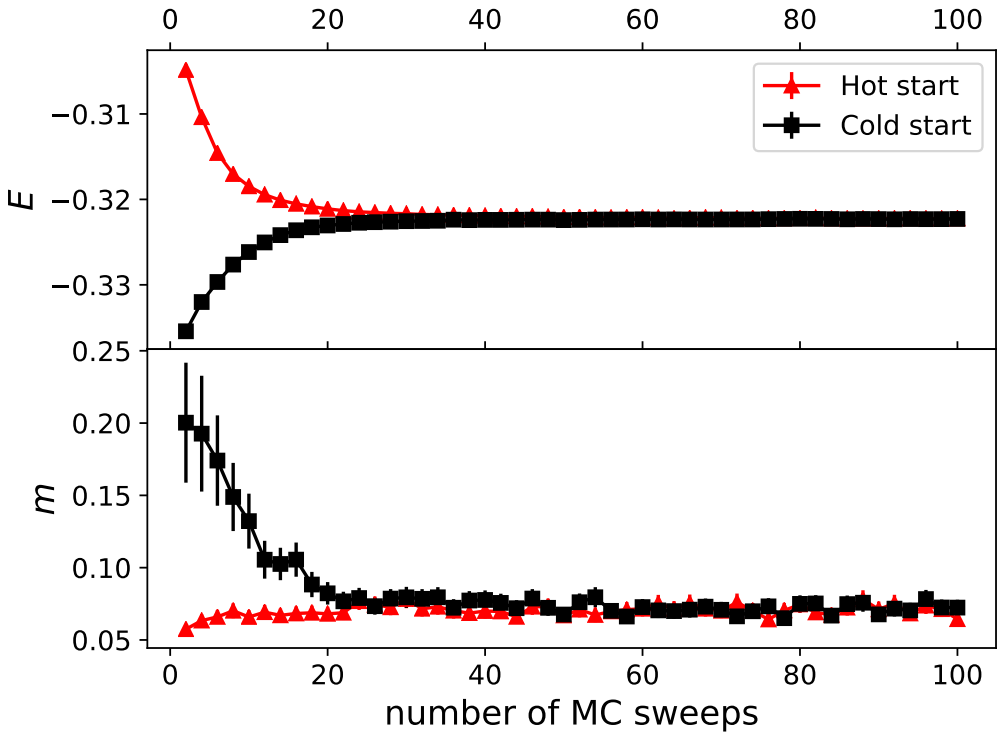

Figure 2. Equilibration of the energy per site E and the magnetization m for a cubic lattice XY model of size $L = 56$, dilution $p = 0.66$, and temperature $T = 0.156$ averaged over 20 disorder configurations. The comparison of hot and cold starts shows that the system equilibrates after roughly 50 Monte Carlo sweeps despite being close to the multicritical point.

For the hexaferrite lattice, we perform 1000 equilibration sweeps and 2000 measurement sweeps (using a hot start). Note that the combination of relatively short Monte Carlo runs and a large number of disorder configurations leads to an overall reduction of statistical error [39, 40, 41].

4.2. DATA ANALYSIS

We employ the Binder cumulant [42] to precisely estimate the critical temperature T_c. It is defined as

$$g = \left[1 - \frac{\langle |\mathbf{m}|^4 \rangle}{3\langle |\mathbf{m}|^2 \rangle^2}\right]_{dis} \tag{7}$$

where $\langle ... \rangle$ denotes the thermodynamic (Monte Carlo) average and $[...]_{dis}$ denotes the disorder average. The Binder cumulant g is a dimensionless quantity, it therefore fulfills the finite-size scaling form

$$g(t, L, u) = g(t\lambda^{-1/\nu}, L\lambda, u\lambda^{\delta}) \ . \tag{8}$$

Here, λ is an arbitrary scale factor, $t = (T - T_c)/T_c$ denotes the reduced temperature, and ν is the correlation length exponent of the (magnetic) finite-temperature phase transition. We have included the irrelevant variable u characterized by the exponent $\delta > 0$ to describe the corrections from the leading scaling behavior observed in our data. Setting the scale factor $\lambda = L^{-1}$, we obtain $g(t, L, u) = F(tL^{1/\nu}, uL^{-\delta})$ where F is a dimensionless scaling function. Expanding F in its second argument yields

$$g(t, L, u) = \Phi(tL^{\frac{1}{\nu}}) + uL^{-\delta}\Phi_u(tL^{\frac{1}{\nu}}) \ . \tag{9}$$

In the absence of corrections to scaling ($u = 0$), the Binder cumulants at $t = 0$ corresponding to different system sizes have the universal value $\Phi(0)$, i.e., the critical temperature is marked by a crossing of all Binder cumulant curves. If corrections to scaling cannot be neglected ($u \neq 0$), this is not the case (see, e.g., Ref. [43]) because $g(0, L, u)$ is not independent of L but takes the value $g(0, L, u) = \Phi(0) + uL^{-\delta}\Phi_u(0)$. Instead, the crossing point shifts with L and approaches $t = 0$ as $L \to \infty$. The functional form of this shift can be worked out explicitly by expanding the scaling functions Φ and Φ_u,

$$g(t, L, u) = \Phi(0) + tL^{\frac{1}{\nu}}\Phi'(0) + uL^{-\delta}\Phi_u(0) \ . \tag{10}$$

Using this expression to evaluate the crossing temperature $T^*(L)$ between the Binder cumulant curves for sizes L and cL (where c is a constant) yields

$$T^*(L) = T_c + bL^{-\omega} \quad \text{with} \qquad \omega = \delta + \frac{1}{\nu} \tag{11}$$

where $b \sim u$ is a non-universal amplitude.

To determine the crossing temperature, we fit the g vs T data sets corresponding to different system sizes with separate quartic polynomials.(Quartic polynomials provide reasonable fits within the temperature range of interest while avoiding spurious oscillations.) The intersection point of these polynomials yields the crossing temperature T^*. To estimate the errors of the crossing temperature we use an ensemble method. For each $g(T)$ curve, we create an ensemble of artificial data sets $g_a(T)$ by adding noise to the data

$$g_a(T) = g(T) + \Delta g(T)\, r \ . \tag{12}$$

Here, r is a random number chosen from a normal distribution of zero mean and unit variance, and $\Delta g(T)$ is the statistical error of the Monte Carlo data for $g(T)$. Note that we use the same random number r for the entire $g(T)$ curve, leading to an upward or downward shift of the curve. This stems from the fact that the statistical error $\Delta g(T)$ is dominated by the disorder noise while the Monte Carlo noise is much weaker. This implies that the deviations at different temperatures of the Binder cumulant from the true average are correlated. Repeating the crossing analysis with these ensembles of curves, we get ensembles of crossing temperatures. Their mean and standard deviation yield T^* and the associated error ΔT^*, respectively.

5. RESULTS

In this section we report the results of our simulations for cubic and hexaferrite lattices occupied by XY or Heisenberg spins.

5.1. CUBIC LATTICES

We investigate the behavior of both XY and Heisenberg models on cubic lattices. To check the validity of our simulations, we first consider clean (undiluted) lattices. We find critical temperatures of $T_c = 2.2017(1)$ and $T_c = 1.44298(2)$ for XY and Heisenberg spins, respectively. They agree well with previously known numerical results [44, 45].

We now turn to diluted systems, starting with the XY case. For reference, the site percolation threshold of the simple cubic lattice is at the vacancy probability $p_c = 0.6883923(2)$ [34]. For low dilutions ($p < 0.64$), the Binder cumulant vs. temperature curves for all simulated system sizes cross through exactly the same point within their statistical errors, implying that corrections to the leading finite-size scaling behavior are not important. Therefore, we determine T_c from the crossing of the $g(T)$ curves of the two largest system sizes, $L^3 = 80^3$ and $L^3 = 112^3$. The ensemble method is applied to find the error of T_c. Fig. 3 shows an example of this situation for dilution $p = 0.1$.

For higher dilutions ($p \geq 0.64$) in the vicinity of the percolation threshold p_c, the crossing of the Binder cumulant vs. temperature curves is less sharp. Specifically, the crossing temperature $T^*(L)$ of the curves for linear system sizes L and $\sqrt{2}L$ shifts visibly towards higher temperatures as the system sizes are increased. An example (for $p = 0.65$) is demonstrated in Fig. 4. As shown in the previous section, this shift is caused by corrections to the leading finite-size scaling behavior. According to Eq. (11), it can be modeled as $T^*(L) = T_c + bL^{-\omega}$. To find the asymptotic (infinite system size) value of T_c, we thus fit the crossing temperature $T^*(L)$ to Eq. (11). As ω is expected to be universal, i.e., to take the same value for all dilutions near p_c, we perform a combined fit for all dilutions $p \geq 0.64$

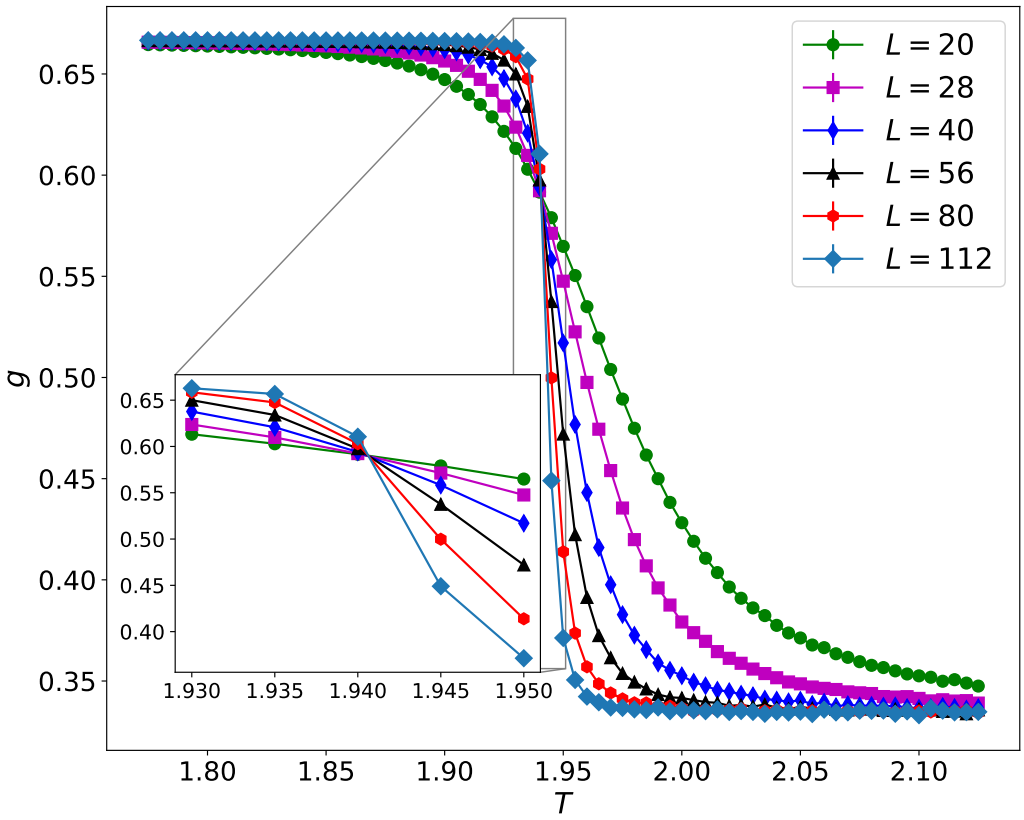

Figure 3. Binder cumulant g vs temperature T for the cubic lattice XY model with dilution $p = 0.10$. The statistical errors arising from the Monte Carlo simulation are smaller than the symbol size. The inset show the intersection region of the curves more closely. All curves cross at the same point within their statistical errors.

and treat ω as a fitting parameter. This combined fit produces $\omega = 1.5 \pm 0.4$. An example of the resulting extrapolation is presented in Fig. 5 for $p = 0.65$. The figure shows that the finite-size shifts of the crossing temperature are not very strong. This is further confirmed in Fig. 6 which presents an overview of the fits for all dilutions from $p = 0.64$ to $p = 0.6825$.

The resulting phase boundary $T_c(p)$ of the site-diluted XY model on a cubic lattice is shown in Fig. 7. The overview given in the inset demonstrates that $T_c(p)$ is indeed continuously suppressed with increasing p and approaches zero as $p \to p_c$. To analyze the functional form of $T_c(p)$ close to p_c, the main panel of Fig. 7 shows a log-log plot of T_c vs. $|p - p_c|$. We observe that the phase boundary follows two different power laws, close

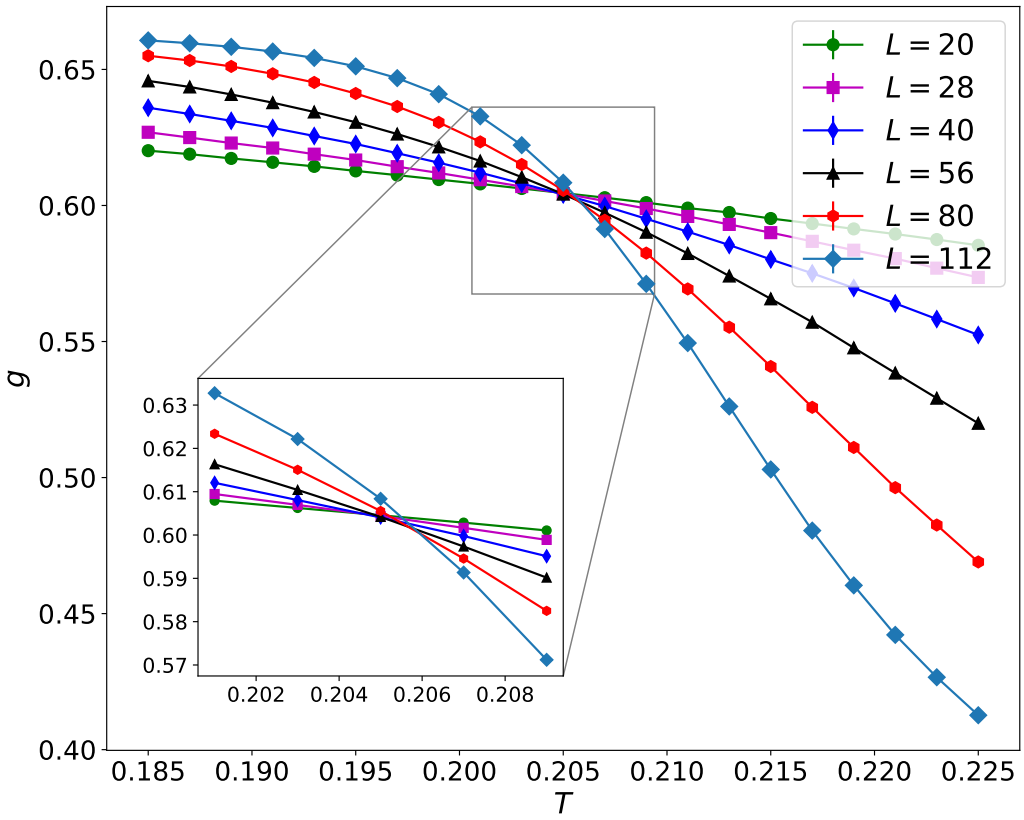

Figure 4. Binder cumulant g vs temperature T for the XY model on a cubic lattice for dilution $p = 0.65$, i.e. close to p_c. The curves do not all cross at the same temperature. Instead, the crossing progressively shifts as L increases. The statistical errors arising from the Monte Carlo simulation are smaller than the symbol size.

to the percolation threshold p_c and further away from p_c. The asymptotic value of ϕ is determined from a fit of the data closest to p_c (viz. p between 0.678 to 0.6825), yielding a crossover exponent of $\phi = 1.09(2)$. Its error estimate is a combination of the statistical error from the fit and a systematic error estimated from the robustness of the value against changes of the fit interval. The asymptotic value of ϕ agrees reasonably well with the prediction of percolation theory. The asymptotic power law describes the data for dilutions above about $p = 0.65$. The asymptotic critical region thus ranges from about $p = 0.65$ to $p_c = 0.6883923$.

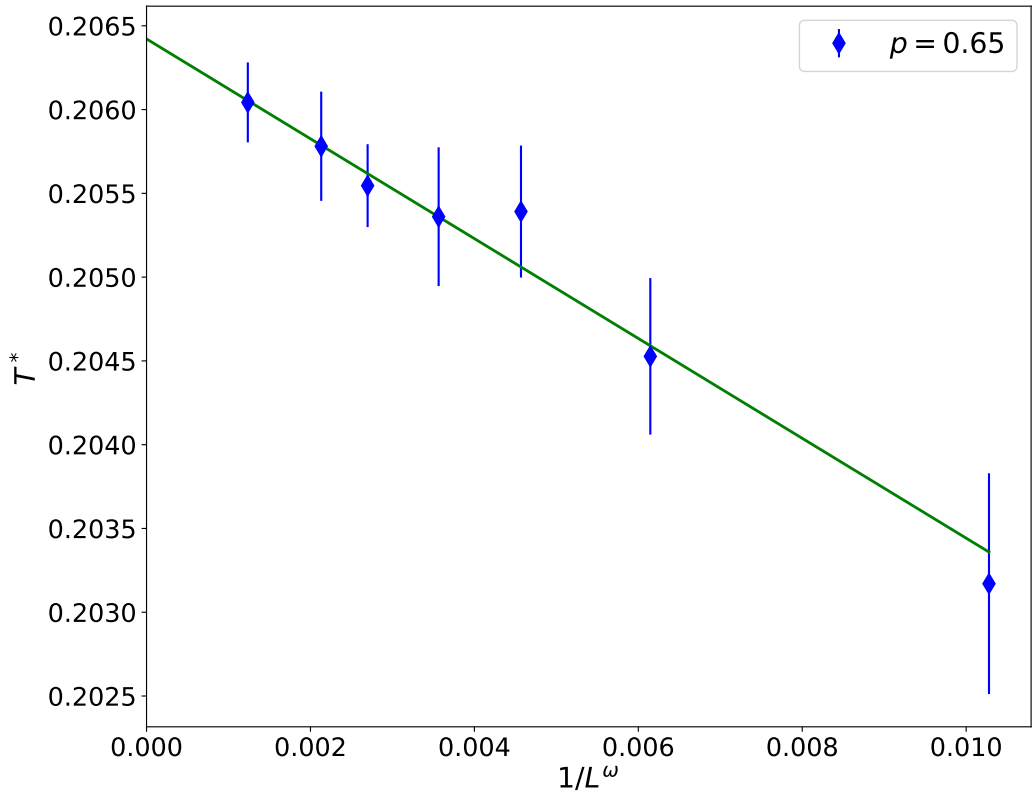

Figure 5. Extrapolation to infinite system size of the crossing temperature T^* of the Binder cumulant curves for system sizes L and $\sqrt{2}L$ using $\omega = 1.5$. The dilution is $p = 0.65$. A fit to Eq. (11) gives $T_c = 0.2064(4)$. The error bars of T^* have been determined using the ensemble method described in Sec. 4.2.

The preasymptotic behavior of $T_c(p)$ for p between $p = 0$ to $p = 0.64$ also follows a power law in good approximation. However, the exponent is significantly below unity, $\phi = 0.80(1)$.

We proceed in the same manner for the Heisenberg model on the cubic lattice. Starting from the clean case, we gradually increase dilution and find $T_c(p)$. In the case of Heisenberg spins, we find that the corrections to finite-size scaling are weaker than in the XY case. Even in the vicinity of p_c, all Binder cumulant curves intersect in a single point within their statistical errors. As an example, the g vs T data for $p = 0.65$ are shown in Fig. 8. The critical temperatures $T_c(p)$ and its error are therefore determined from the Binder cumulant crossing for system sizes $L^3 = 80^3$ and $L^3 = 112^3$, the largest systems simulated.

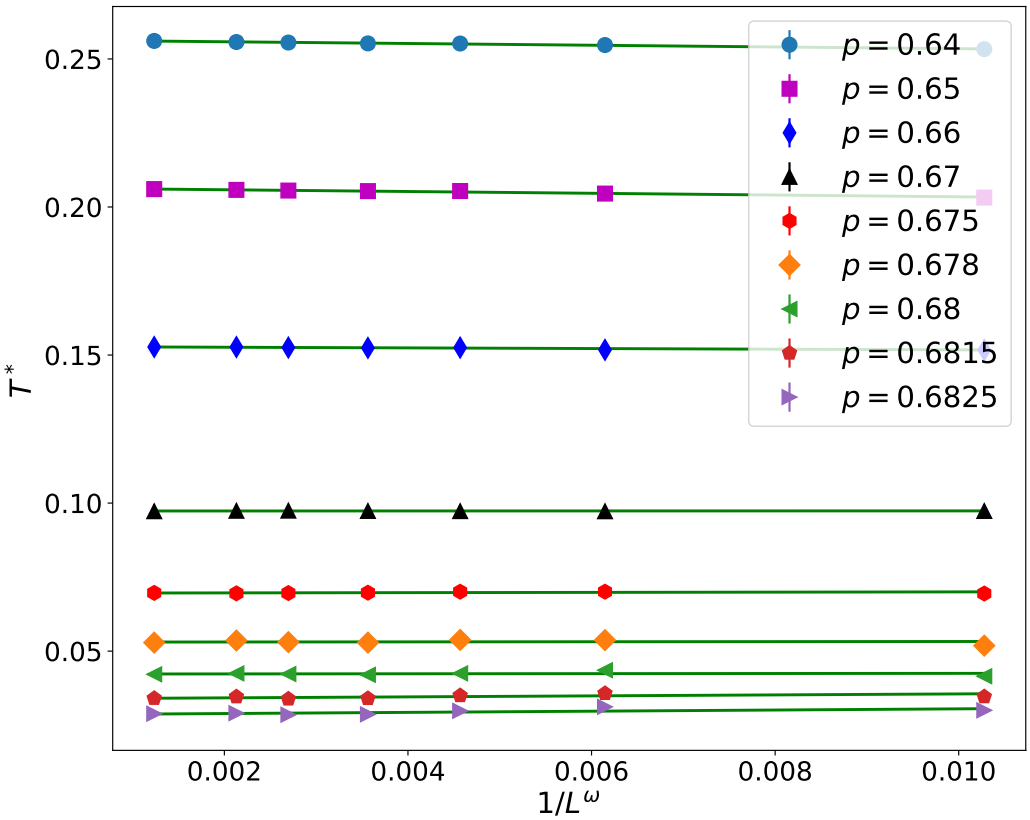

Figure 6. Overview of the extrapolations of the crossing temperatures T^* for several dilutions near p_c using $\omega = 1.5$. The error bars ΔT^* are smaller than the symbols.

The phase boundary of the site-diluted Heisenberg model on a cubic lattice is constructed from these data and shown in Fig. 9. Similar to the XY case, we observe two separate power law exponents governing the phase boundary. The dilutions $p \gtrsim 0.65$ constitute the asymptotic critical region with crossover exponent $\phi = 1.08(2)$, in agreement with the percolation theory prediction. The nonuniversal preasymptotic crossover exponent obtained for dilutions $p \lesssim 0.62$ is again smaller than unity, $\phi = 0.86(1)$, but somewhat larger than in the XY case.

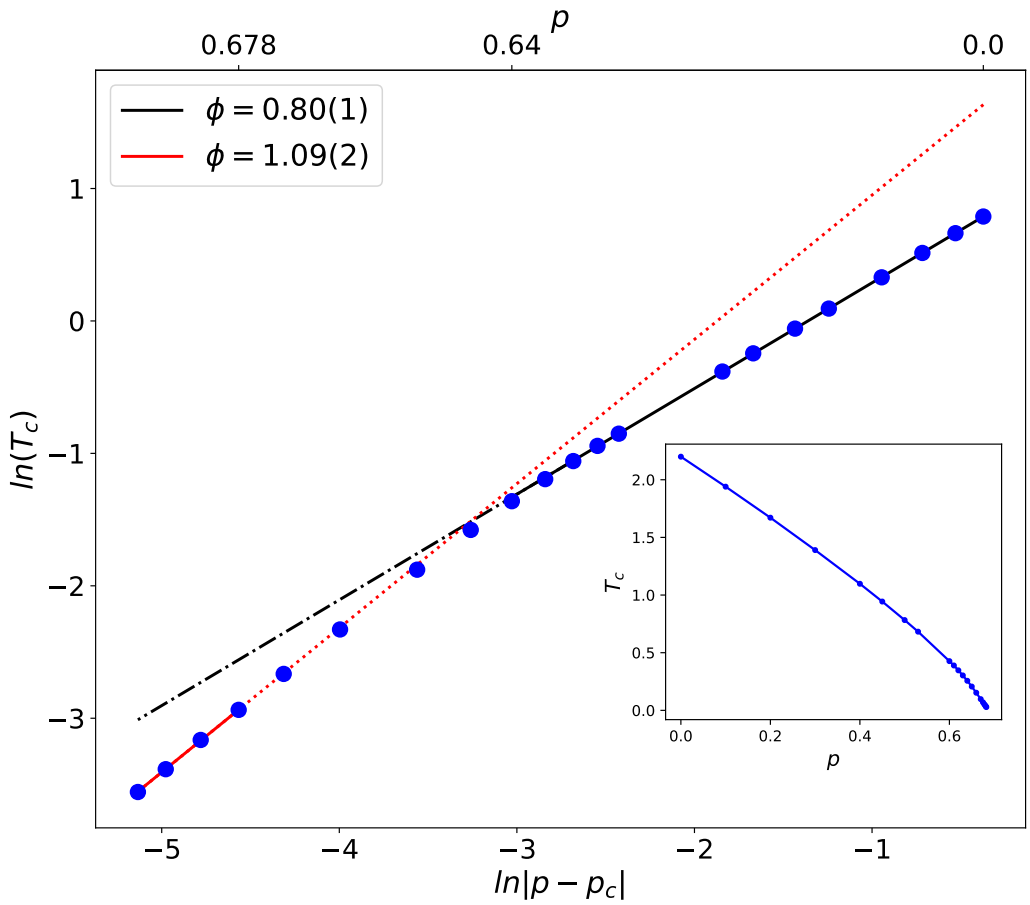

Figure 7. Phase boundary of the site-diluted XY model on a cubic lattice. Main panel: Log-log plot of T_c vs. $|p - p_c|$. The straight lines are power-law fits, $T_c \sim |p - p_c|^{\phi}$. They are shown as solid lines within the fit range. The dotted and dash-dotted lines are extrapolations. For details see text. Inset: Overview presented as linear plot of T_c vs. p. All error bars of the data points are smaller than the symbol size.

5.2. HEXAGONAL FERRITE LATTICE

Whereas the asymptotic critical behavior of the phase boundary close to the percolation threshold is expected to be universal, its behavior outside the asymptotic critical region does not have to be universal. For a better quantitative understanding of the magnetic phase boundary of the diluted hexaferrites, we therefore also perform simulations of the Heisenberg model (3) using the hexaferrite crystal structure and realistic exchange interac-

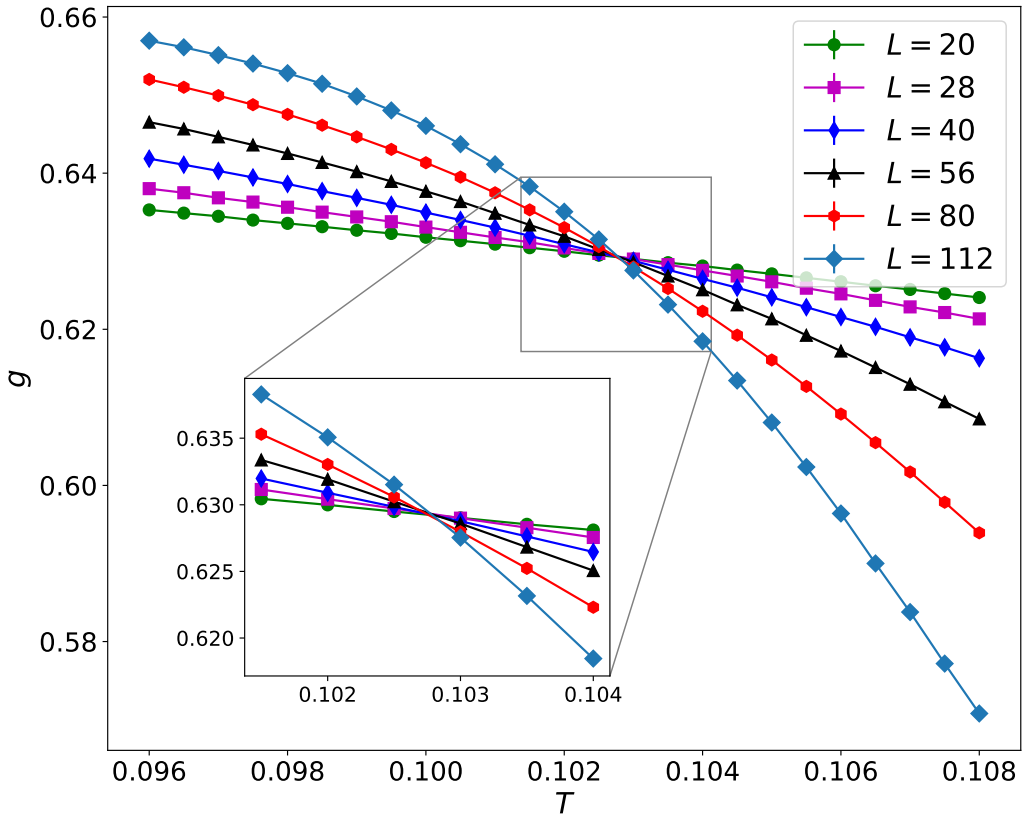

Figure 8. Binder cumulant g vs temperature T for dilution $p = 0.65$ on cubic lattice and Heisenberg spins. All curves cross at the same temperature. Error bars are smaller than the symbol size.

tions. In the calculations, we focus on the leading non-frustrated interactions, as outlined in Sec. 2.2. The site percolation threshold for the lattice spanned by these interactions is $p_c = 0.7372(5)$ [1].

As before, the critical temperature T_c for a given dilution is determined from the Binder cumulant crossings. Corrections to the finite-size scaling were found to be negligible within the statistical errors. Thus, we used the Binder cumulant crossing of the two largest system sizes (28^3 and 40^3 double unit cells) to find T_c. The resulting phase boundary is shown in Fig. 10. The behavior of this phase boundary is very similar to the cubic lattice results. High dilutions, $p \gtrsim 0.68$, fall into the asymptotic critical region with a crossover exponent of $\phi = 1.12(3)$, in excellent agreement with the percolation theory predictions.

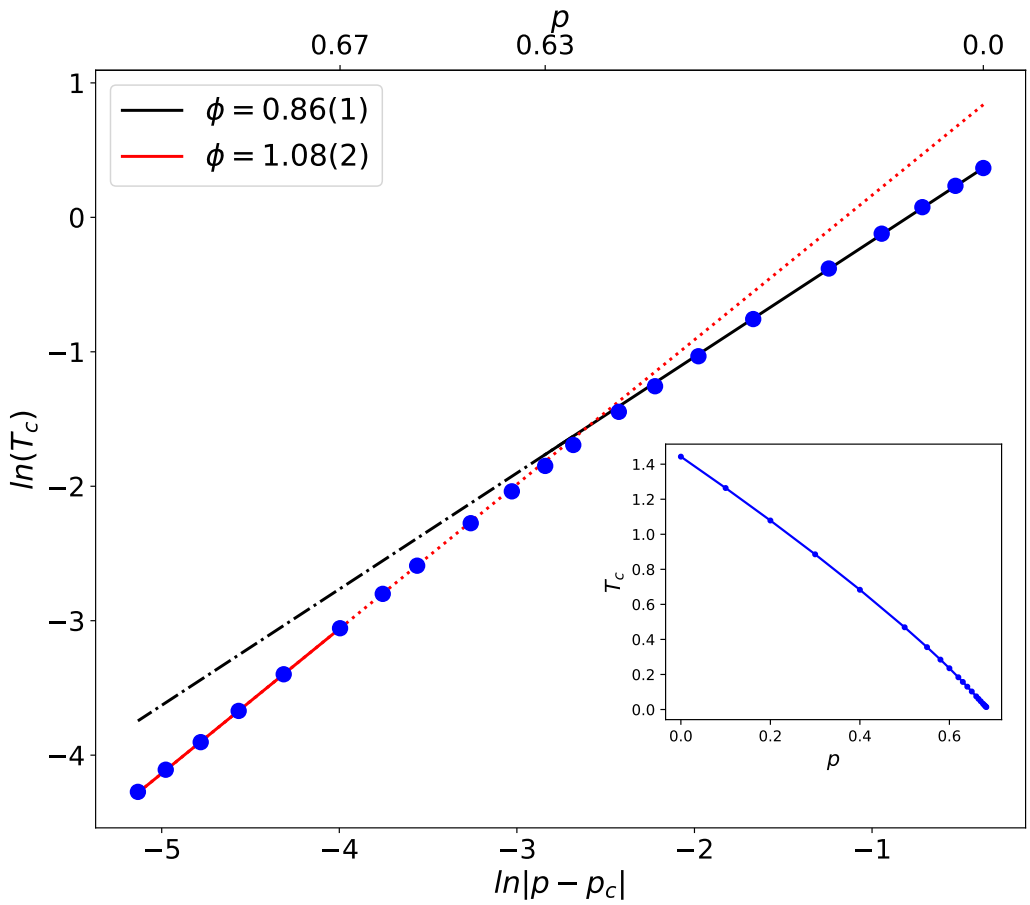

Figure 9. Phase boundary of the site-diluted Heisenberg model on a cubic lattice. Main panel: Log-log plot of T_c vs. $|p - p_c|$. The straight lines are power-law fits, $T_c \sim |p - p_c|^{\phi}$. They are shown as solid lines within the fit range. The dotted and dash-dotted lines are extrapolations. For details see text. Inset: Overview presented as linear plot of T_c vs. p. All error bars of the data points are smaller than the symbol sizes.

This also confirms the universality of the asymptotic crossover exponent. The preasymptotic exponent $\phi = 0.88(2)$ that governs the behavior for dilutions below about 0.65 is smaller than unity and takes roughly the same value as for the Heisenberg model on the cubic lattice.

Our numerical results disagree with the experimentally observed 2/3 power law, $T_c(x) = T_c(0)(1 - x/x_c)^{2/3}$. In the simulations, the transition temperature T_c is suppressed more rapidly with x than in the experimental data (see Fig. 11). To explore possible reasons for this discrepancy, we also perform test simulations that include additional weaker exchange interactions [31] that frustrate the ferrimagnetic order. The results of these

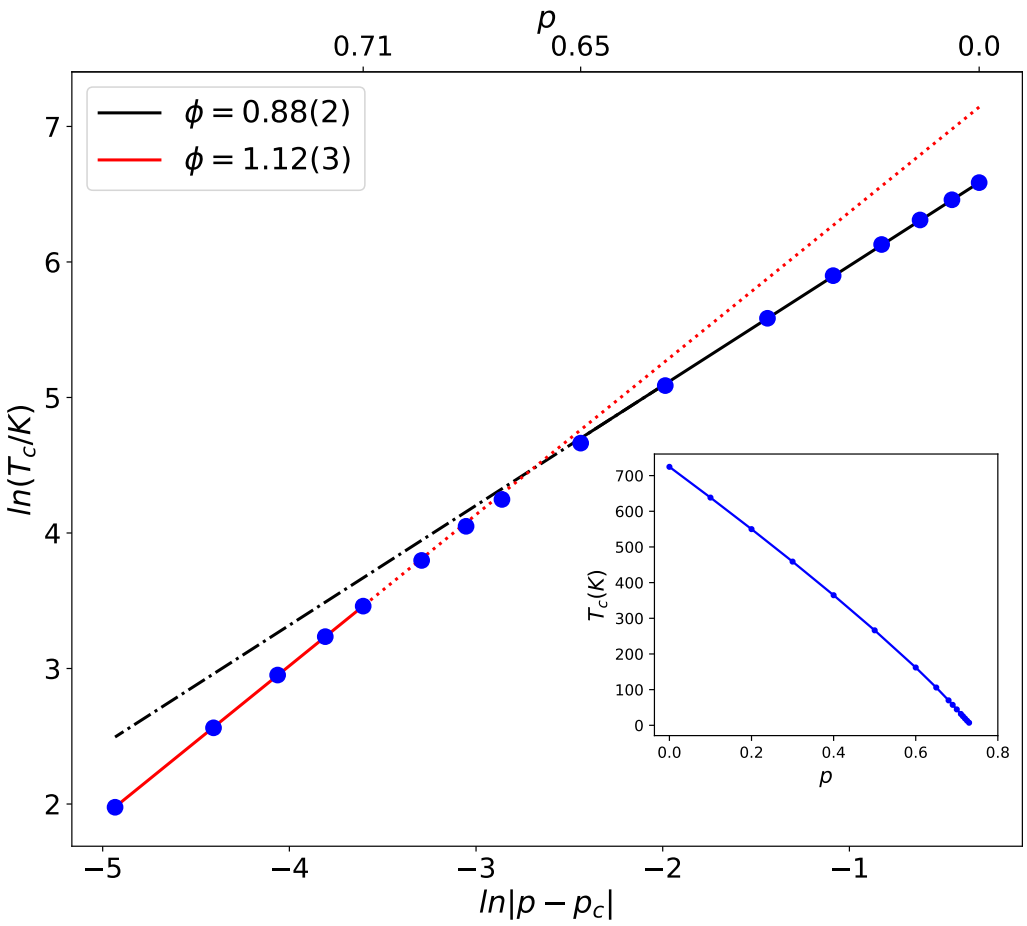

Figure 10. Phase boundary for the Heisenberg model on a hexagonal ferrite lattice. The main panel shows the log-log plot of T_c vs. $|p - p_c|$. The statistical errors of the data (determined by the ensemble method) are smaller than the symbol size. The straight lines are fits to $T_c \sim |p - p_c|^{\phi}$. They are shown as solid lines within the fit range. The dotted and dash-dotted lines are extrapolations. For details see text. The inset shows a linear plot the complete phase boundary $T_c(p)$.

simulations, which are included in Fig. 11, show that these weaker frustrating interactions have little effect at low dilutions. At higher dilutions, when the ferrimagnetic order is already weakened, the frustrating interactions further suppress the transition temperature. They thus further increase the discrepancy between the experimental data and the Monte Carlo results.

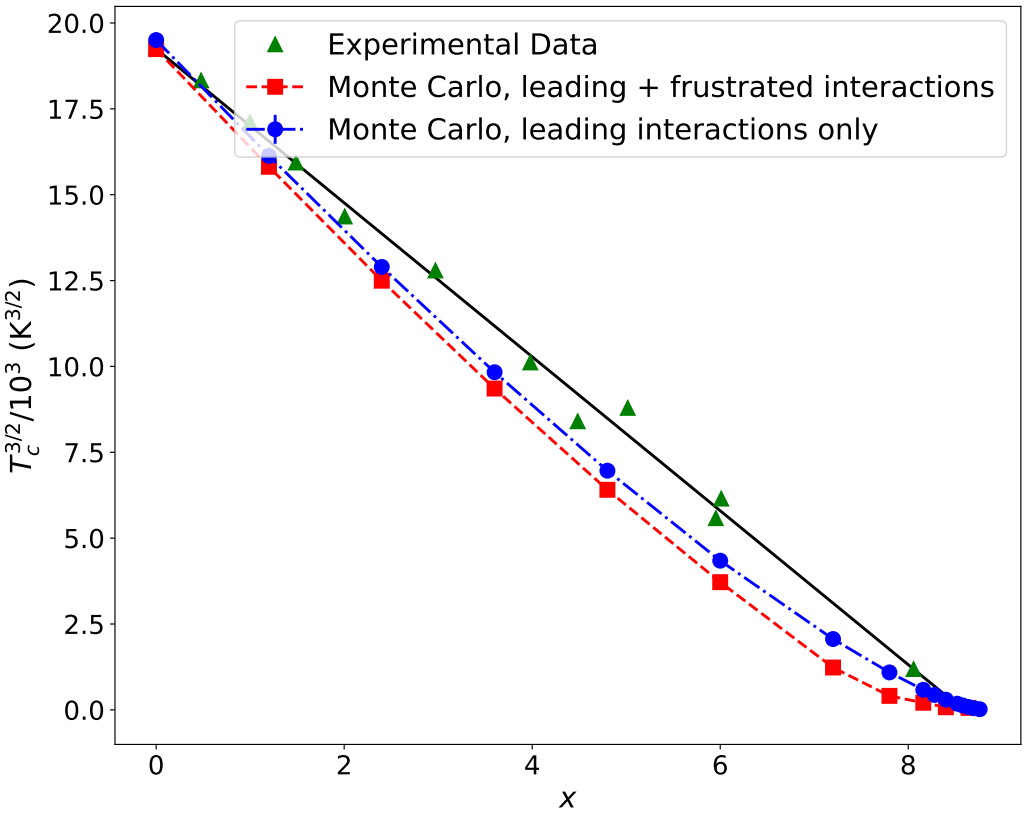

Figure 11. Comparison between the numerically determined phase boundary $T_c(x)$ and the experimental data for $PbFe_{12-x}Ga_xO_{19}$ [1]. The tuning parameter x is related to the dilution by $x/12 = p$. The Monte Carlo simulations show a more rapid suppression of T_c with x. Including additional weak frustrated interactions increases the discrepancy.

6. CONCLUSION

To summarize, motivated by recent experimental observations on hexagonal ferrites, we have studied classical site-diluted XY and Heisenberg models by means of large-scale Monte Carlo simulations, focusing on the shape of the magnetic phase boundary. We have obtained two main results.

First, for high dilutions close to the lattice percolation threshold, the critical temperature depends on the dilution via the power law $T_c \sim |p - p_c|^{\phi}$ in all studied systems. In this asymptotic region, we have found the values $\phi = 1.09(2)$ and $1.08(2)$ for XY and Heisenberg spins on cubic lattices, respectively. For the Heisenberg model on the hexa-

ferrite lattice, $\phi = 1.12(3)$. These values agree with each other and with the prediction $\phi = 1.12(2)$ of classical percolation theory. The crossover exponent ϕ thus appears to be super-universal, i.e., it takes the same value not just for different lattices but also for XY and Heisenberg symmetry.

Interestingly, the asymptotic critical region of the percolation transition is very narrow, as the asymptotic power-laws only hold in the range $|p - p_c| \lesssim 0.04$. At lower dilutions, the phase boundary still follows a power law in $|p - p_c|$, but with an exponent that appears to be non-universal and below unity (in the range between 0.8 and 0.9).

Our second main result concerns the origin of the $2/3$ power law, $T_c(x) = T_c(0)(1 - x/x_c)^{2/3}$, that was experimentally observed in $PbFe_{12-x}Ga_xO_{19}$ over the entire concentration range between 0 and close to the percolation threshold [1]. Neither the asymptotic nor the preasymptotic power laws identified in the simulations match the experimental result. In fact, in all simulations, the critical temperature is suppressed more rapidly with increasing dilution than in the experiment. The observed shape of the magnetic phase boundary in $PbFe_{12-x}Ga_xO_{19}$ thus remains unexplained.

Potential reasons for the unusual behavior may include the interplay between magnetism and ferroelectricity in these materials [46] or the presence of quantum fluctuations (arising from the frustrated magnetic interactions mentioned above), even though it is hard to imagine that these stay relevant at temperatures as high as 720 K. Another possible explanation could be a statistically unequal occupation of the different iron sites in the unit cell by Ga ions. Exploring these possibilities remains a task for the future. Disentangling these effects may also require additional experiments introducing further tuning parameters such as pressure or magnetic field in addition to chemical composition.

ACKNOWLEDGEMENTS

We acknowledge support from the NSF under Grant nos. DMR-1506152, DMR-1828489, and OAC-1919789. The simulations were performed on the Pegasus and Foundry clusters at Missouri S & T. We also thank Martin Puschmann for helpful discussions.

II. HELICITY MODULUS AND CHIRAL SYMMETRY BREAKING FOR BOUNDARY CONDITIONS WITH FINITE TWIST

Gaurav Khairnar, Thomas Vojta
Department of Physics, Missouri University of Science and Technology, Rolla, Missouri 65409, USA. Email: grktmk@mst.edu [5]

ABSTRACT

We study the response of a two-dimensional classical XY model to a finite (non-infinitesimal) twist of the boundary conditions. We use Monte Carlo simulations to evaluate the free energy difference between periodic and twisted-periodic boundary conditions and find deviations from the expected quadratic dependence on the twist angle. Consequently, the helicity modulus (spin-stiffness) shows a non-trivial dependence on the twist angle. We show that the deviation from the expected behavior arises because of the mixing of states with opposite chirality which leads to an additional entropy contribution in the quasi-long-range ordered phase. We give an improved prescription for the numerical evaluation of the helicity modulus for a finite twist, and we discuss the spontaneous breaking of the chiral symmetry for the anti-periodic boundary conditions. We also discuss applications to discrete spin systems and some experimental scenarios where boundary conditions with finite twist are necessary.

1. INTRODUCTION

The study of magnetic materials with the help of spin models such as the Ising or Heisenberg models has resulted in tremendous progress in condensed matter physics. For clean systems with short-range interactions, surface energies are negligible, and the choice of boundary conditions does not affect the thermodynamic bulk behavior. On the other

[5]Published: Physical Review E 111, 024114 (2025)

hand, in disordered systems such as spin glasses, effects of various boundary conditions have been a topic of active interest [47, 48, 49]. In the presence of long-range interactions in an Ising spin system, different choices of boundary condition lead to seemingly different thermodynamic behaviors. By choosing artificial coupling-dependent boundary condition, an uncountable number of exotic spin states of the ground state can be generated at any temperature, whereas free boundary conditions, which are considered physical, do not generate the same effect [50]. In XY or Heisenberg spin glasses, small rotations at the boundary are expected to yield non-smooth changes in the ground state [51]. In these systems, different boundary conditions are advantageous for revealing the numerous phases and their physical properties [52, 53, 54].

Even in system in which the boundary conditions do not affect the bulk behavior, they can have interesting and observable consequences. For example, thermodynamic Casimir forces [55], which arise due to the confinement of critical order parameter fluctuations, were found to be affected by the boundary conditions [56, 57, 58, 59, 60] (for a recent review of exact results see Ref. [61]). An analogous force, the Helmholtz force, arises in the canonical ensemble and also shows a strong dependence on the boundary conditions [62]. Moreover, the response of a system to a change in boundary conditions can be employed as a tool to measure (bulk) equilibrium properties.

In this paper, we reconsider the seemingly simple but surprisingly complex effects of a finite (non-infinitesimal) twist of the boundary conditions on a ferromagnetic XY system. Brown and Ciftan [45] suggested, in the context of the three-dimensional Heisenberg model, that the mixing of states with differing chirality plays an important role and affects the observed helicity modulus. However, a quantitative understanding of this effect and its origins has not been achieved yet. We therefore study this question in detail for the two-dimensional classical XY model by means of large-scale Monte Carlo simulations.

We find that the free energy cost of a non-infinitesimal twist in the boundary condition in the quasi long-range ordered (QLRO) low-temperature phase deviates from the expected quadratic dependence on the twist angle. Mixing of states with opposite chirality provides an extra entropy contribution which takes the value $\ln(2)$ (in units in which $k_B = 1$) for a π-twist. Beyond their intrinsic interest, our results potentially apply to experiments aimed at detecting the Berezinskii–Kosterlitz–Thouless (BKT) transition [5, 6]. They are also important for systems with discrete $Z(N)$ (clock) order parameter symmetry where any twist in the boundary conditions is necessarily non-infinitesimal. In addition, our findings enable novel numerical algorithms for computing the helicity modulus in simulations with a finite twist.

Our paper is organized as follows. In section 2, we introduce the XY Hamiltonian under boundary conditions with an arbitrary twist, and we define the helicity modulus. Section 3 contains the details of the numerical simulations. In section 4, we present our results for the dependence of the free energy on the twist angle and discuss the resulting helicity modulus. We also analyze the spontaneous breaking of the chiral symmetry that occurs for antiperiodic boundary conditions below the BKT transition. We conclude in section 5.

2. THE MODEL

We are interested in the classical XY model, a system of planar spins described by the Hamiltonian

$$H = -J \sum_{<ij>} \mathbf{S}_i \cdot \mathbf{S}_j = -J \sum_{<ij>} \cos(\phi_i - \phi_j) \ . \tag{1}$$

Here, $J > 0$ denotes the ferromagnetic exchange interaction (which will be set to unity in the simulations), the sum is over pairs of nearest neighbors on a d-dimensional hypercubic lattice, and $\mathbf{S} = (S_x, S_y)$ is a two-component unit vector. Equivalently, the XY spins can be represented by their phases ϕ, defined via $S_x = \cos\phi$, $S_y = \sin\phi$. Twisted boundary

conditions can be implemented by fixing the spins at two opposite boundaries at specific orientations (phases) with a fixed angle Θ between them. Alternatively, we consider the Hamiltonian (1) with periodic boundary conditions and modify the interactions across one of the boundaries to introduce the twist. This is achieved by replacing the interaction terms across the chosen boundary by $-J\cos(\phi_i - \phi_j - \Theta)$. We call these boundary conditions twisted-periodic, and the usual periodic boundary conditions are recovered for $\Theta = 0$.

The phase diagram of the classical XY model is well-understood. Long-range order is impossible in one and two dimensions at any nonzero temperature due to the Mermin-Wagner theorem [63]. In three and higher dimensions, there is a phase transition between a paramagnetic high-temperature phase and a ferromagnetic low-temperature phase. The two-dimensional XY model is special because the system undergoes a BKT phase transition into a quasi long-range ordered low-temperature phase.

In a long-range ordered or quasi long-range ordered phase, a twist in the boundary conditions increases the system's free energy. The system can lower its free energy by distributing the total twist (angular difference) Θ over the entire sample, i.e., by gradually changing the average orientation of the spins in the bulk. For a system of linear size L, the lowest free energy is expected when the average phase changes by Θ/L between neighboring sites (in the direction the twist is applied). For large L, this local phase change is small, which suggests that the free energy can be expanded in powers of Θ/L. As the free energy difference ΔF between the twisted and untwisted systems must be an even function of Θ, the expansion is expected to take the form

$$\Delta F = F_\Theta - F_0 = \frac{\rho_s}{2}\left(\frac{\Theta}{L}\right)^2 L^d \tag{2}$$

to quadratic order in Θ/L. This relation can be understood as a definition of the helicity modulus (or spin stiffness) ρ_s,

$$\rho_s(\Theta) = \frac{2\Delta F}{\Theta^2} L^{2-d} \ . \tag{3}$$

This definition still depends on the value of the imposed twist angle Θ. Some papers in the literature including the seminal work by Fisher, Barber, and Jasnow [64] define the helicity modulus via a twist angle of π, i.e., via the free energy difference between periodic and antiperiodic boundary conditions (in analogy with the study of interfacial energies in Ising models). Other authors define the helicity modulus via the response to an infinitesimal twist (in the spirit of linear response theory),

$$\rho_{s0} = \rho_s(0) = \left(\frac{\partial^2 F}{\partial \Theta^2} \right)_{\Theta=0} L^{2-d} \ . \tag{4}$$

It has generally been assumed that the two definitions lead to the same stiffness values because the local, layer-to-layer twist Θ/L is small in either case (in the thermodynamic limit), justifying the expansion (2) of the free energy [65, 66]. However, we will see that this is not the case, at least not in two space dimensions.

The definition (4) has the advantage that the second derivative of the free energy can be expressed in terms of appropriate correlation functions of the untwisted system. This leads to the formula [67, 68]

$$\begin{aligned} \left(\tfrac{\partial^2 F}{\partial \Theta^2} \right)_{\Theta=0} &= \tfrac{1}{L^2} \textstyle\sum_{<ij>} J \left\langle \cos(\phi_i - \phi_j) \right\rangle (x_i - x_j)^2 \\ &\quad - \tfrac{\beta}{L^2} \left\langle \left\{ \textstyle\sum_{<ij>} J \sin(\phi_i - \phi_j)(x_i - x_j) \right\}^2 \right\rangle \end{aligned} \tag{5}$$

where x_i is the coordinate of site i in the twisted direction, and $\langle ... \rangle$ denotes the thermodynamic average evaluated at $\Theta = 0$. For a derivation of Eq. (5), see Appendix 5. This formula allows the evaluation of the helicity modulus without actually having to apply twisted boundary conditions.

As the paramagnetic phase is insensitive to the boundary conditions, the free energy difference decays exponentially with system size, $\Delta F \sim e^{-L/\xi}$, where ξ is the correlation length. This implies $\rho_s = 0$ in the paramagnetic phase in the thermodynamic limit. In contrast, ΔF is expected to scale as L^{d-2} in an ordered or quasi long-range ordered phase, and the helicity modulus is finite. In two dimensions, ρ_s is known to have an universal jump at the BKT phase transition. For $d > 2$, ρ_s vanishes continuously at T_c, governed by the critical behavior of the phase transition. In the rest of the paper, we focus on two dimensions, but we will comment on higher dimensions in the concluding section.

3. NUMERICAL SIMULATIONS

We perform large-scale Monte Carlo simulations to evaluate the free energy difference between systems with periodic and twisted-periodic boundary conditions. The free energy cannot be measured directly in a standard Monte Carlo simulation. Instead, it can be evaluated explicitly by integrating the internal energy $U = \langle H \rangle$ over the inverse temperature $\beta = 1/T$,

$$F(T) = F(T_0) + T \int_{\beta_0}^{\beta} d\beta' U(\beta') \ . \tag{6}$$

We choose the starting temperature T_0 sufficiently high (well above the BKT transition) such that the free energies of the twisted and untwisted systems agree with each other within the statistical errors. This ensures that $F(T_0)$ drops out of the free energy difference (2). We note that there are alternative approaches that allow one to directly measure the free energy difference between different boundary conditions in a simulation. This is achieved

by including appropriate boundary terms as dynamical variables in the Monte Carlo scheme (see, e.g., Refs. [69, 70]). The challenge in these approaches is to ensure a sufficiently rapid relaxation of the boundary variables, especially in the absence of cluster algorithms.

Our simulations employ both the single spin-flip Metropolis algorithm [71, 72] and the Wolff cluster-flip algorithm [37]. For systems with periodic boundary conditions, the efficient Wolff algorithm greatly reduces critical slowing down. Thus, a full MC sweep consists of one Metropolis sweep followed by one Wolff sweep for the case of periodic boundary conditions. However, for twisted-periodic boundary conditions with twist angle $0 < \Theta < \pi$, the Wolff algorithm cannot be employed. This stems from the fact that the angle between two spins of a Wolff cluster is not preserved (but rather changes sign) when the cluster is flipped. Consequently, the cluster flip changes the energy of a twisted bond inside the cluster, invalidating the algorithm. In the case of twisted-periodic boundary conditions with $0 < \Theta < \pi$, we therefore only employ Metropolis sweeps. For a twist angle of exactly π, the twisted bonds effectively become antiferromagnetic as $\cos(\Delta\phi - \pi) = -\cos(\Delta\phi)$. The energy of an antiferromagnetic bond is invariant under a sign change of $\Delta\phi$, and the Wolff algorithm can be used.

To facilitate the numerical integration (6) for the free energy, we initiate the simulations at the highest temperature T_0 (using a "hot" start, i.e., all spins are randomly oriented at the beginning of the simulation). The temperature is then reduced in small steps dT until the desired final temperature is reached. Most production simulations started from $T_0 = 30$, much higher than the BKT transition temperature of $T_c = 0.89290(5)$ [73]. The temperature step dT is gradually decreased from $dT = 0.5$ at T_0 to $dT = 0.02$ in the transition region and below. To check how sensitive the free energy difference ΔF is to these parameters, we performed tests with T_0 as high as 90 and dT as low as 0.01. The free energy differences resulting from these test calculations agreed with the production results within their statistical errors.

For periodic boundary conditions, we perform up to 2000 full equilibration sweeps (each consisting of a Metropolis sweep followed by a Wolff sweep) and up to 8000 full measurement sweeps at each temperature step. For twisted-periodic boundary conditions, we perform up to about 80 000 (Metropolis only) equilibration sweeps and up to about 160 000 measurement sweeps. (As usual, the quality of the equilibration was confirmed by comparing the results of hot and cold starts.) We simulate systems of linear sizes up to $L^2 = 80^2$ and average the results over about 5000 samples. Each sample is subjected to periodic and twisted-periodic boundary conditions, and the resulting free energies are compared to evaluate the helicity modulus from eq. (3).

We use an ensemble method (see, e.g., Ref. [74]) to estimate the error of the free energy. We generate a large ensemble of synthetic internal energy curves $U_i(T) = U(T) + r(T)\Delta U(T)$, where ΔU is the statistical error obtained from Monte Carlo and $r(T)$ is a random number chosen from a normal distribution of unit variance. Integrating these curves via (6) generates an ensemble of free energies F_i. Mean and standard deviation of this ensemble are then propagated through eq. (3) to find the helicity modulus and the associated error.

4. RESULTS

4.1. FREE ENERGY RESPONSE TO FINITE TWIST

We now turn to our results for the response of the two-dimensional XY model to various twists in the boundary conditions. Figure 1(a) shows the helicity modulus $\rho_s(\Theta)$ as a function of temperature for an infinitesimal twist as well as a twist of $\Theta = \pi/3$. For the infinitesimal twist, ρ_s is measured in the untwisted system via eq. (5). For a finite twist, ρ_s is obtained from the free energy difference between simulations with twisted and untwisted

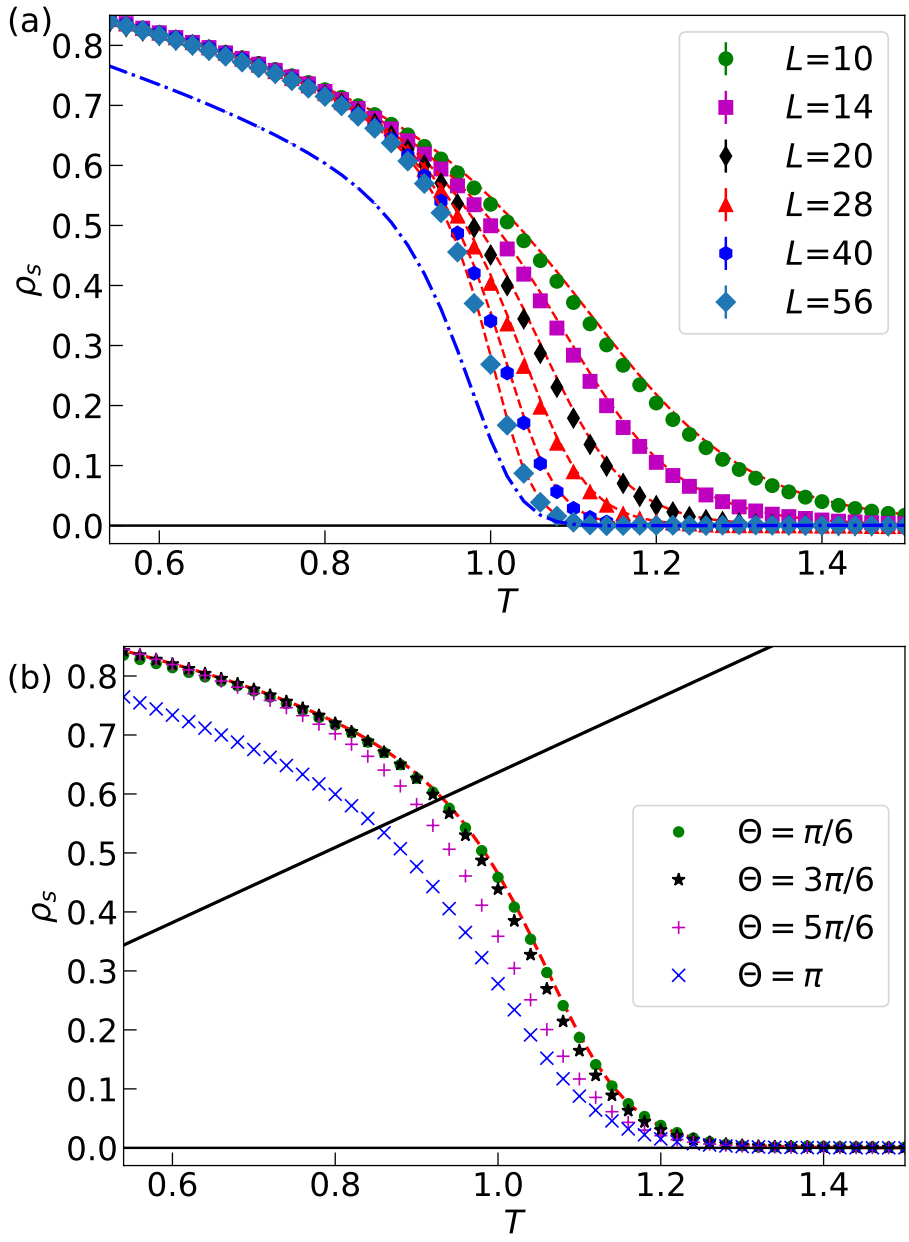

Figure 1. (a) Helicity modulus $\rho_s(\Theta)$ as a function of temperature T for different system sizes L. The filled symbols show ρ_s for a twist of $\Theta = \pi/3$, obtained via Eqs. (3) and (6). The dotted lines show ρ_{s0} for an infinitesimal twist measured in the untwisted system via Eq. (5). The straight solid line corresponds to $\rho_s = 2T/\pi$, it intersects the stiffness curves at temperatures $T^*(L)$. The critical temperature T_c is obtained by extrapolating $T^*(L)$ to the thermodynamic limit according to Eq. (7). This extrapolation gives $T_c = 0.891(7)$. In contrast, the helicity modulus values for a twist of $\Theta = \pi$, shown as dash-dotted line for $L = 56$, are significantly lower than the other data. (b) Helicity modulus $\rho_s(\Theta)$ as a function of temperature T at fixed $L = 40$ for different twist angles Θ. The statistical errors in both panels are comparable to or smaller than the symbol sizes.

boundary conditions, as explained in Sec. 3. The resulting ρ_s values for the infinitesimal twist and $\Theta = \pi/3$ agree within their statistical errors, giving us additional confidence in our numerical approach.

The helicity modulus curves can be used to find the critical temperature. In the thermodynamic limit, ρ_s vanishes in the disordered phase whereas it is nonzero in the quasi long-range ordered phase. The BKT transition is marked by a universal jump in ρ_s. Using the Kosterlitz-Nelson relation, T_c can be identified by the intersection of the infinite-system ρ_s vs. T curve with a straight line of slope $2/\pi$ [75]. As the correlation length increases exponentially for $T \to T_c$ at a BKT transition, finite-size corrections take a logarithmic form. Thus, T_c is found by extrapolating $T^*(L)$, the temperature at which the ρ_s vs. T curve for size L intersects the line of slope $2/\pi$, according to

$$T^*(L) = T_c + \frac{A}{\ln^2(bL)} \tag{7}$$

where A, b are non-universal fitting parameters. We find $T_c = 0.891(7)$ from twisted boundary conditions with $\Theta = \pi/6$, which agrees with high-accuracy results in the literature [73, 76, 77, 78].

Figure 1(a) also shows data for $\Theta = \pi$. Unexpectedly, the helicity modulus values resulting from eq. (3) in this case are significantly below the values for smaller Θ. This is further illustrated in Fig. 1(b) which compares the helicity modulus for different twist angles Θ. Whereas the data for $\Theta = 0, \pi/6$, and $\pi/2$ all agree within their error bars, some deviations appear for $\Theta = 5\pi/6$ close to the BKT transition. They become more pronounced for $\Theta = \pi$ and persist in the entire quasi-long-range ordered phase. It is worth emphasizing that this happens even though the layer-to-layer twist Θ/L remains small compared to unity, justifying the expansion that leads to eq. (2). What is the reason for this surprising discrepancy? Arguments put forward in Ref. [45] suggest that the chirality of the twist plays an important role.

So far we have considered thermodynamic states that fulfill the global twist Θ in, say, the clockwise direction by introducing an average clockwise twist of Θ/L between neighboring layers. However, the same global twist can be achieved by a counter-clockwise twist with local angle of $(2\pi - \Theta)/L$ between consecutive layers. At low temperatures, the additional free energy for a twist in the "wrong" direction is much larger than $k_B T$. Therefore, this state is exponentially suppressed. Local twist angles corresponding to higher winding numbers can also be ruled out using the same argument. However, with increasing temperature, states of both chiralities (and higher winding numbers) will be mixed, leading to an extra entropic contribution to the free energy. Importantly, $\Theta = \pi$ is a special case that allows the mixing of opposite chiralities even at $T = 0$. Let us now quantitatively study the mixing of the states as twist, temperature and system size is varied.

According to eq. (2), we expect the free energy difference between the twisted and untwisted systems to behave as $\Delta F \propto \Theta^2$, at least as long as higher-order terms in Θ/L can be neglected. We have studied the Θ dependence of ΔF systematically at various temperatures in the quasi long-range ordered phase close to T_c; the results are presented in Fig. 2. The figure shows that ΔF follows the quadratic Θ dependence up to about $\Theta = 2\pi/3$ within the statistical errors of the data, but significant deviations are observed for larger twist angles.

The special case of anti-periodic boundary conditions ($\Theta = \pi$) right at the BKT transition temperature was already studied by Hasenbusch [79, 80]. He derived an expression for the ratio of the partition functions with periodic and antiperiodic boundary conditions in the two-dimensional XY model. It includes the leading finite-size corrections and reads

$$\frac{Z_{\Theta=\pi}}{Z_{\Theta=0}} = 0.08643(1) - \frac{0.1358(1)}{\ln(L) + C}\,, \tag{8}$$

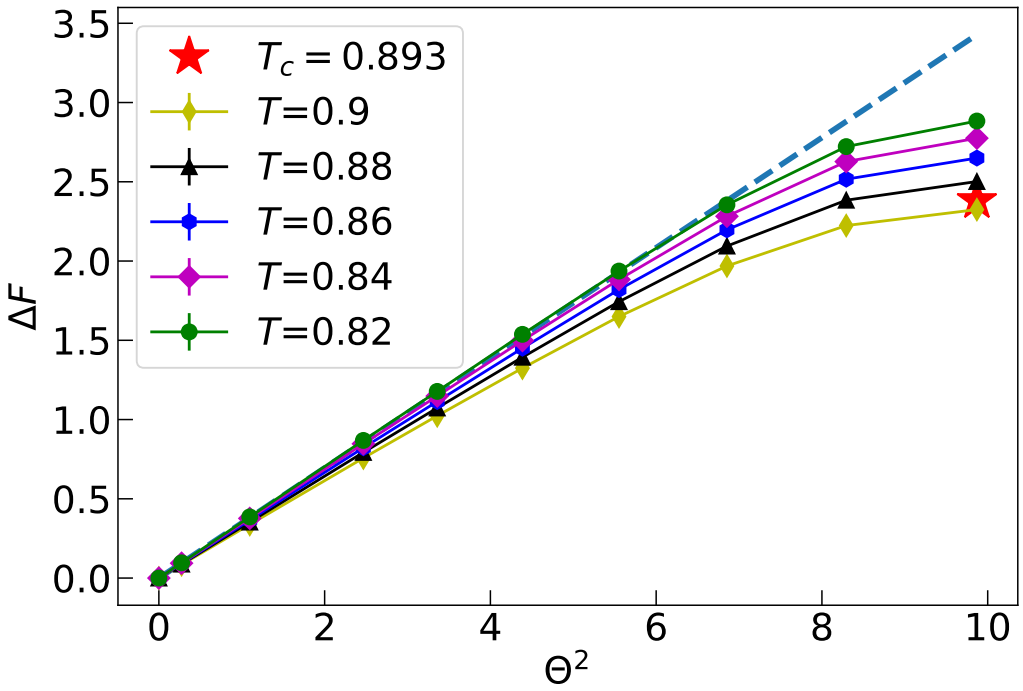

Figure 2. Free energy difference ΔF between systems with periodic and twisted-periodic boundary conditions vs. squared twist angle Θ^2 for size $L = 40$ and several temperatures close to T_c. The dashed line shows a fit of ΔF for $T = 0.82$ to a quadratic Θ dependence in the range $0 \le \Theta^2 \le (2\pi/3)^2$. ΔF at $T_c \approx 0.893$, obtained using eq. (8) is marked by the star symbol. Statistical errors are comparable to the symbol size or smaller.

where the constant C approximately captures contributions from higher order terms. For the purpose of comparing with our Monte Carlo results, we set $C = 4.3$ as in Ref. [79]. The free energy difference ΔF resulting from this formula agrees well with our data, see Fig. 2.

We attribute the deviation of ΔF from the quadratic Θ dependence to the mixing of states of opposite chirality which becomes more pronounced as Θ approaches π. The extent of the mixing can be estimated by studying a simple two-state model consisting of a state with clockwise (CW) chirality of the twist and a state with counter-clockwise (CCW) chirality. At low temperatures and large L, the energy associated with the CW state reads $U_{\mathrm{CW}} = -JL^2[1 + \cos(\Theta/L)] \approx -2JL^2 + J\Theta^2/2$, whereas the energy of the CCW state is given by $U_{\mathrm{CCW}} = -JL^2[1 + \cos((2\pi - \Theta)/L)] \approx -2JL^2 + J(2\pi - \Theta)^2/2$. At higher temperatures, fluctuations about the perfect spin-wave states become important. Their effect

can be approximately captured by replacing J in the above formulas for U_{CW} and U_{CCW} by the (renormalized) helicity modulus $\rho_s(T)$. The corresponding canonical probabilities of CW and CCW states read

$$p_{\mathrm{CW}} = \frac{1}{Z} e^{-\frac{\rho_s \Theta^2}{2T}} , \quad p_{\mathrm{CCW}} = \frac{1}{Z} e^{-\frac{\rho_s (2\pi-\Theta)^2}{2T}} \tag{9}$$

with

$$Z = e^{-\frac{\rho_s \Theta^2}{2T}} + e^{-\frac{\rho_s (2\pi-\Theta)^2}{2T}} . \tag{10}$$

As discussed earlier, this implies that the CCW state is exponentially suppressed as $T \to 0$ for any $\Theta < \pi$ whereas both states contribute equally at all temperatures below T_c for $\Theta = \pi$.

The helicity modulus right at the BKT transition temperature T_c is known from the Kosterlitz-Nelson relation, $\rho_s(T_c) = \frac{2T_c}{\pi}$. Inserting this into eq. (9) gives the canonical probabilities shown in the inset of Fig. 3. The contribution of the CCW state to the mixture increases with Θ and becomes significant for $\Theta \gtrapprox 2\pi/3$. The free energy difference ΔF between systems with periodic and twisted-periodic boundary conditions can also be computed within the two-state model,

$$\Delta F = \langle \Delta U \rangle - TS \tag{11}$$

where S is the Von-Neumann entropy. The main panel of Fig. 3 shows ΔF as a function of Θ at the BKT transition temperature. The deviation of ΔF from the quadratic dependence on Θ resembles the corresponding Monte Carlo result in Fig. 2. Moreover, ΔF from Eq. (8) in the thermodynamic limit $L = \infty$ (marked by the star symbol) agrees well with the model results. The simple two-state system thus captures the important features present in Fig. 2. This supports the notion that the mixing of states with opposite chiralities leads to the deviation of ΔF from the quadratic Θ dependence.

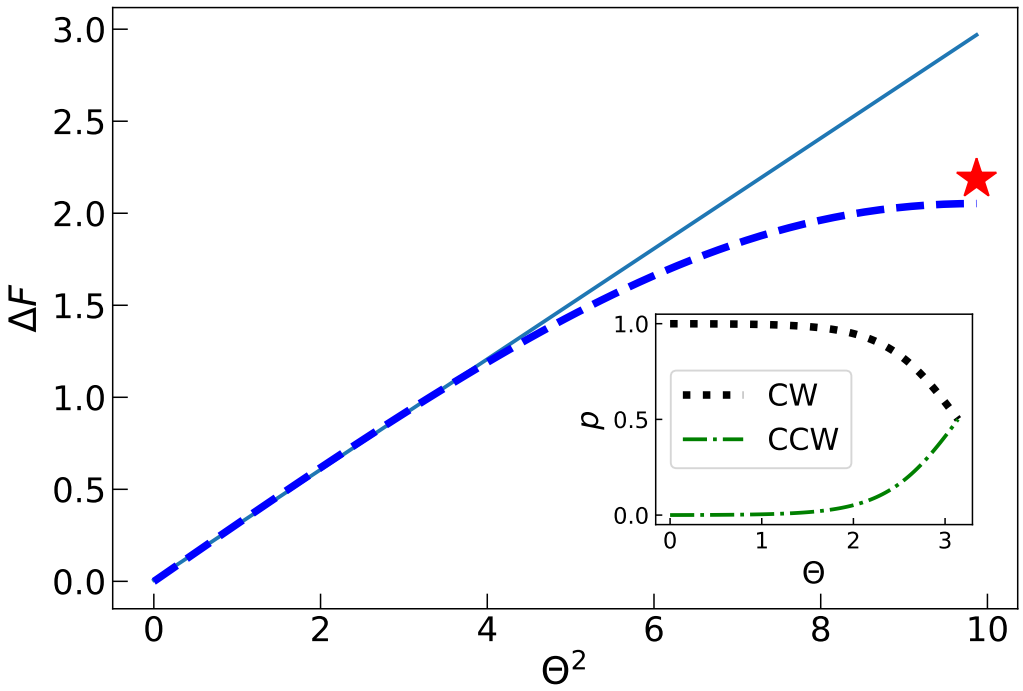

Figure 3. Free energy difference ΔF at the BKT transition temperature T_c between systems with periodic and twisted-periodic boundary conditions, as evaluated using the two-state model (dashed line). The solid line corresponds to a quadratic fit in the range $0 \leq \Theta^2 \leq (2\pi/3)^2$. The value of ΔF from eq. (8) in the thermodynamic limit is marked by the star symbol. The canonical probabilities of the two states are shown in the inset as functions of Θ.

We now move beyond the two-state model and quantify the mixing of chiralities in the Monte Carlo data. To determine the excess free energy due to the mixing, we first fit a quadratic function to $\Delta F(\Theta)$ in the range $0 \leq \Theta \leq 2\pi/3$ (separately for each system size). Denoting the fit function by $\Delta F_{\text{fit}}(L, T, \Theta)$, we define the excess free energy $\delta\Delta F$ at twist angle π as the difference between $\Delta F_{\text{fit}}(L, T, \pi)$ and the $\Delta F_{\text{MC}}(L, T, \pi)$ obtained from MC,

$$\delta\Delta F(L, T, \pi) = \Delta F_{\text{fit}}(L, T, \pi) - \Delta F_{\text{MC}}(L, T, \pi). \tag{12}$$

In other words, ΔF_{fit} is the free energy cost of the twist expected if only states of one chirality contribute, whereas $\delta\Delta F$ captures the additional free energy due to chirality mixing.

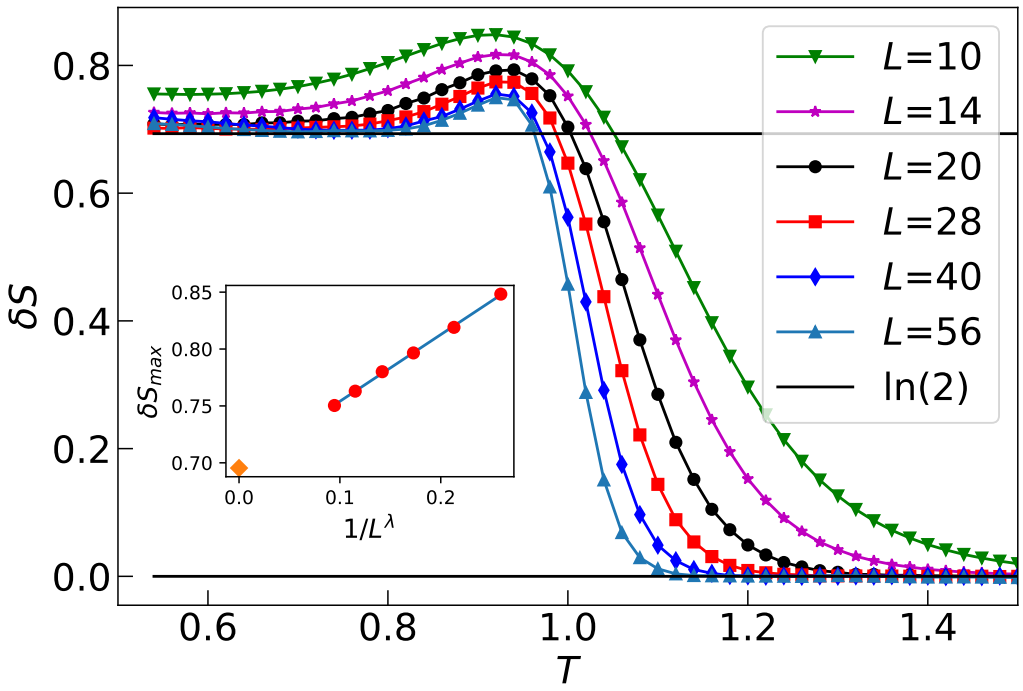

Figure 4. Excess entropy δS due to the mixing of chiralities vs. temperature T for different system sizes. The solid horizontal line corresponds to $\delta S = \ln(2)$. The inset shows the extrapolation of the maximum value of each δS vs. T curve to infinite system size. The extrapolation gives $\delta S_{\max}(L = \infty) = 0.69(1)$ and agrees with $\ln(2)$.

As the excess free energy is expected to be entropic in nature, we define $\delta S = \delta \Delta F / T$ as the excess entropy due to the mixing of chiralities. Our numerical results for the excess entropy are presented in Fig. 4. The figure shows that δS approaches zero with increasing system size for high temperatures while it appears to approach a constant for low temperatures. In fact, the figure suggests that δS approaches a step function in the thermodynamic limit. To determine the step height and position, we extrapolate the peak value $\delta S_{\max}$ of the δS vs. T curves using,

$$\delta S_{\max}(L) = \delta S_{\max}(\infty) + aL^{-\lambda} \tag{13}$$

where a, λ are fitting parameters. (We determine $\delta S_{\max}$ as an extremum of a quadratic curve fitted in the vicinity of the peak.) The extrapolation is shown in the inset of Fig. 4 and yields $\delta S_\infty = 0.69(1) \approx \ln(2)$, in agreement with the expectation of contributions from two degenerate states. Additionally, an extrapolation of the temperature at which the δS vs. T curves cross the $\delta S = \ln(2)$ line matches with T_c within the error bars. Thus, our numerical data extrapolate to $\delta S = \ln(2)\Theta(T_c - T)$ where Θ is the Heavyside step function. We note that the arguments predicting the excess $\ln(2)$ entropy due to the chirality mixing do not include states with higher winding numbers. These states are known to renormalize the helicity modulus in two dimensions [77, 81], but the effect is tiny and only visible in high-accuracy simulations beyond our numerical precision.

The excess entropy due to the chirality mixing reduces the free energy cost of a π twist by $T\ln(2)$. Consequently, the helicity modulus $\rho_s(\pi)$ computed from eq. (3) is reduced by $2\ln(2)T/\pi^2$ compared to the infinitesimal twist value arising from eq. (4). This explains the observation in Fig. 1 of a lower helicity modulus for the π twist. Consequently, if one wishes find the critical temperature from simulations employing a π twist (i.e., anti-periodic boundary conditions), the reduction of ρ_s has to be accounted for. This can be achieved by adding the correction to the Kosterlitz-Nelson relation by changing the slope of the line crossing the ρ_s curves from $2/\pi$ to $2/\pi - 2\ \ln(2)/\pi^2$. The resulting analysis is presented in Fig. 5 which shows the helicity modulus for a π twist as a function of temperature for different system sizes. To find T_c we extrapolate, using eq. (7), the intersection temperature of the ρ_s curves with a line of modified slope, and obtain $T_c = 0.897(2)$. This is in reasonable agreement with the literature value [77].

4.2. BREAKING OF THE CHIRAL SYMMETRY

In Sec. 4.1, we have established that, for an imposed twist $\Theta = \pi$, the thermodynamic ensemble contains an equal mixture of states with clockwise and counter-clockwise local twists. Now we explore the question whether a single given macroscopic system fluctuates

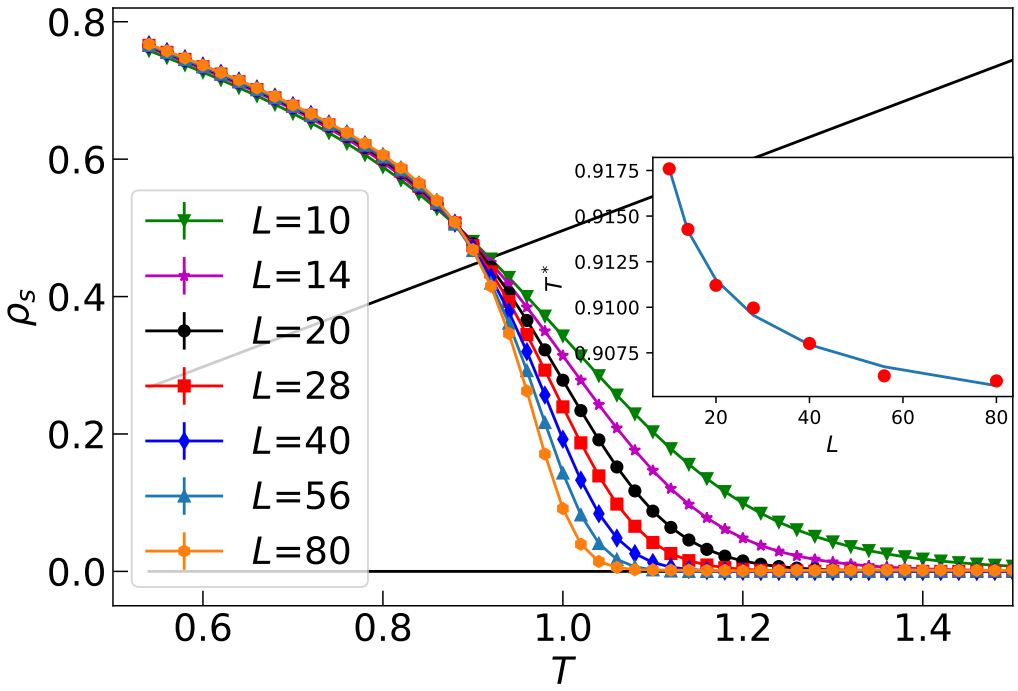

Figure 5. Helicity modulus $\rho_s(\pi)$ for a twist of $\Theta = \pi$ (anti-periodic boundary conditions). The inset shows the intersection temperatures T^* of the helicity modulus curves with the modified Kosterlitz-Nelson line of slope $2/\pi - 2\ \ln(2)/\pi^2$. An extrapolation according to eq. (7) yields $T_c = 0.897(2)$.

between clockwise and counter-clockwise orientations or whether it spontaneously breaks the chiral symmetry below T_c by freezing into one orientation. As the classical XY Hamiltonian does not contain any dynamic terms, the answer to this question will depend on the assumed dynamics of the system. Here, we focus on dissipative local model-A dynamics according to the Hohenberg-Halperin classification [82], i.e., a purely relaxational dynamics without conservation laws. However, the results should hold qualitatively for other local dynamics as well.

To analyze chiral fluctuations, we define the bulk chirality h via the vector product between nearest-neighbor spins along the direction of the twist. Assuming a twist in the x-direction, h is given by

$$h = \frac{1}{L} \sum_{\langle ij \rangle_x} \hat{\mathbf{k}} \cdot \left(\mathbf{S}_i \times \mathbf{S}_j \right) \tag{14}$$

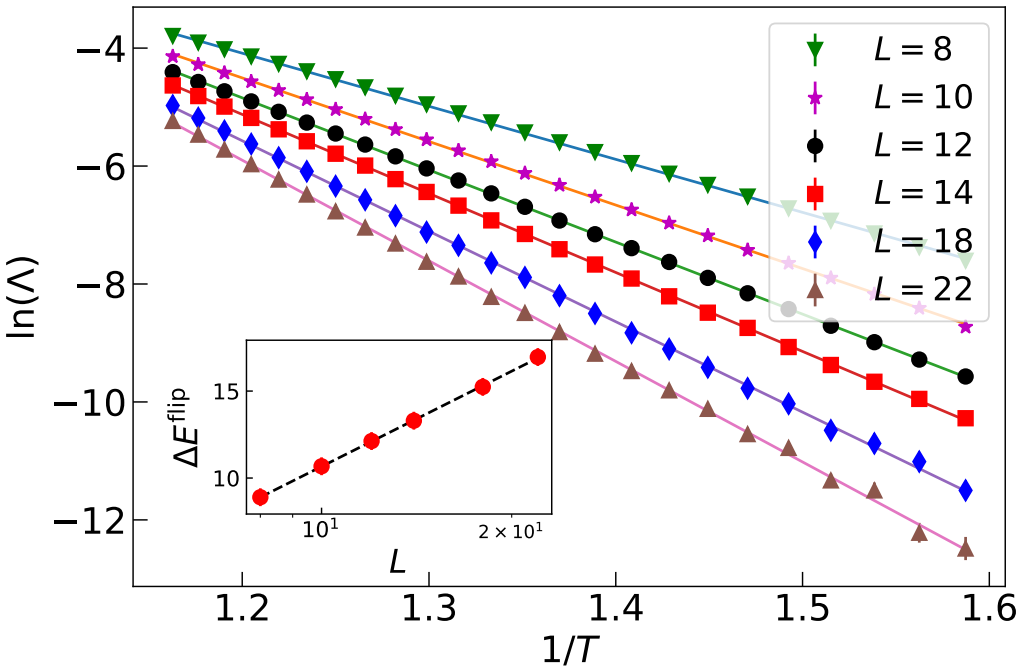

Figure 6. Flip rate Λ of the bulk chirality h as a function of the inverse temperature $1/T$ for different system sizes L. The solid lines are fits to the ansatz (15). The resulting system size dependence of the activation energy ΔE^{flip} is shown in the inset in a semi-logarithmic plot. The dotted line is a fit to the function, $\Delta E^{\text{flip}} = E_0 \ln(k_0 L)$, giving fit parameters $E_0 = 7.91(6)$ and $k_0 = 0.39(1)$.

where site j is the nearest neighbor of site i in the positive x direction, and $\hat{\mathbf{k}}$ is the unit vector in the z-direction. This means positive h correspond to a counter-clockwise twist and negative h correspond to a clockwise twist.

We monitor the time evolution of the bulk chirality h in long Monte Carlo runs that perform only local Metropolis updates (implementing model-A dynamics). Specifically, we measure the rate Λ at which the chirality changes sign during such a simulation. Figure 6 shows the flip rate Λ as a function of temperature for different system sizes observed for runs of 1.2×10^6 Metropolis sweeps averaged over 400 samples. The data clearly suggest an exponential dependence of the flip rate on the inverse temperature. Indeed, if chirality flips are governed by activation over an energy barrier ΔE^{flip}, the flip rate is expected to

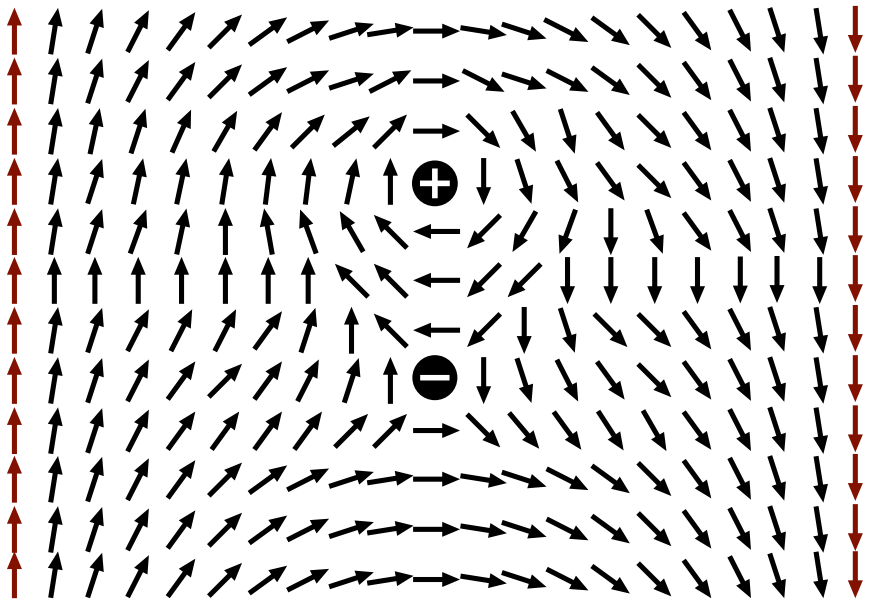

Figure 7. Schematic illustrating how a vortex-antivortex pair can flip the bulk chirality. For details see text.

follow the ansatz

$$\Lambda = cT^b \exp(-\Delta E^{\text{flip}}/T) \; . \tag{15}$$

where b and c are fit parameters. Figure 6 demonstrates that the observed flip rates indeed follow this ansatz within their statistical errors. The activation energies ΔE^{flip} obtained from the fits in Fig. 6 are presented in the inset as a function of the system size in a semi-logarithmic plot. The data are well described by the logarithmic function

$$\Delta E^{\text{flip}} = E_0 \ln(k_0 L) \tag{16}$$

with $E_0 = 7.91(6)$ and $k_0 = 0.39(1)$. This logarithmic dependence suggests that flips of the bulk chirality are facilitated by a vortex mechanism.

Figure 7 illustrates how the creation and annihilation of a vortex-antivortex pair can reverse the sign of the bulk chirality. Imagine a system with fixed boundaries in the x-direction that impose a π twist and periodic boundary conditions in the y-direction. Initially,

the system features a uniform clockwise twist to satisfy the boundary conditions. When a vortex-antivortex pair is introduced as shown in the figure, the spins between the vortices now rotate in the opposite direction. Now imagine that the + vortex travels upwards across the (periodic) boundary, approaches the − vortex from below, and finally annihilates. The end result is a state with a uniform counter-clockwise twist, i.e., the chirality h has changed sign. The activation energy of this process is given by the energy of a vortex-antivortex pair at the largest distance $L/2$. In the continuum limit, the energy of a vortex-antivortex pair at distance D is given by $E_{\text{pair}} = E_{\text{core}} + 2\pi J \ln(D/a)$ where E_{core} is the vortex core energy and a the core size. Neglecting the core energy (which can be formally absorbed by a shift of a), a comparison with eq. (16) gives a reasonable agreement. This indicates that the leading contribution to ΔE^{flip} comes from the formation of a vortex-antivortex pair. Deviations can be attributed to finite-size effects, contributions from other flip processes and uncertainties in the sequence of fits leading to eq. (16) [6].

The results of this section demonstrate that the energy required to flip the bulk chirality diverges with system size in the thermodynamic limit. The divergence is only logarithmic in L in contrast to the case of a domain wall whose energy would diverge linearly in L in two dimensions. Nonetheless, it implies that a macroscopic system will not fluctuate between states of opposite bulk chirality during its time evolution (for local dynamics). In other words, the chiral symmetry is spontaneously broken below the BKT transition.

[6] If one considers open rather than periodic boundary conditions in the direction perpendicular to the twist, a single vortex moving across the system is sufficient to flip the bulk chirality. Test simulations with open boundary conditions lead to the same logarithmic dependence (16) of the activation energy ΔE^{flip} but with prefactor $E_0 = 3.7(1)$, indicating the formation of a single vortex.

5. CONCLUSION

To summarize, in this paper we have studied the effects of finite (non-infinitesimal) twists in the boundary conditions on a two-dimensional classical ferromagnetic XY model. The system's response to the twist has been studied by a direct evaluation of the free energy by means of large-scale Monte Carlo simulations. We have found that in the quasi long-range ordered phase below the BKT transition, the free energy cost of a non-infinitesimal twist deviates from the expected quadratic dependence on the twist angle. In the case of a π twist (anti-periodic boundary conditions), the mixing of states of opposite chiralities causes an excess entropy contribution of $\ln(2)$ that lowers the free energy cost of the twist. Thus, if the helicity modulus is calculated from the free energy of a π-twisted system (using eq. (4)), its value is reduced compared to the usual helicity modulus obtained from an infinitesimal twist. We note that our results have been obtained by comparing periodic and twisted-periodic boundary conditions. However, all our arguments are expected to hold as well for systems in which the boundary spins are held at fixed angles. We also note that our discussion has been based on the phase representation of the XY model, but the same results are expected in other representations [83, 84, 85, 86] provided they correctly reflect the chiral symmetry of the boundary conditions.

A macroscopic π-twisted system in the quasi long-range ordered phase spontaneously breaks the chiral symmetry between states with clockwise and counter-clockwise local twists (at least in the case of local dynamics). This implies that experiments on a single macroscopic system cannot observe the $\ln(2)$ entropy contribution from chirality mixing and the corresponding reduction of the apparent helicity modulus value. The excess entropy is expected to be observable in mesoscopic systems that are small enough to fluctuate between states with opposite chirality and in situations involving not just a single system but an entire (thermodynamic) ensemble.

Chirality mixing is important for computer simulations for at least two reasons. First, efficient simulations often involve nonlocal algorithms (such as the Wolff cluster algorithm) that can freely flip the bulk chirality of the system. Moreover, system sizes in computer simulations are sometimes not very large so that even algorithms with local updates (such as the Metropolis algorithm) may allow the system to fluctuate between different chiralities. Free energies of π-twisted systems computed in such simulations contain the $-T\ln(2)$ entropic free energy contribution due to chirality mixing. To compute the usual (infinitesimal-twist) helicity modulus ρ_{s0} from simulations with a π twist, this entropic contribution needs to be removed. When determining the BKT transition temperature from the helicity modulus data, one can, alternatively, modify the Kosterlitz-Nelson relation as discussed in Sec. 4.1.

The effects of twisted boundary conditions on an XY model in thin-film geometry were also studied in Ref. [59] using a mean-field theory. For a twist of $\Theta = \pi$, this work finds an additional singularity of the free energy below the bulk critical temperature. It is induced by the boundary conditions and leads to kink in the Casimir force. In our calculations, we do not observe such a singularity. We believe that this may stem from the fact that the mechanism proposed in Ref. [59], viz., a competition between a rotational state and a planar state to fulfill the boundary conditions, requires soft spin variables and does not hold for the hard spins (of fixed unit length) of our XY model. Alternatively, the lack of additional singularity might be because states with both directions of rotation are simultaneously realized in our simulations at all twist angles, whereas in Ref. [59], only one direction is considered in the calculations.

The partition function of a quantum system in d dimensions can often be mapped onto that of a classical system in $d + 1$ dimensions. Our results thus apply to a one-dimensional (particle-hole symmetric) quantum rotor model with twisted boundary conditions. Specifically, our findings imply that in a finite-size rotor model the states with opposite chirality hybridize. However in the thermodynamic limit, the ground state is

doubly degenerate because the hybridization goes to zero and the tunneling time between states of opposite chirality diverges with system size. Analogous results are expected in a field-theoretic approach based on the sine-Gordon model [87, 88].

The present paper has focused on two dimensions. Two dimensions are a special case because the free energy cost of a twist is independent of system size, see eq. (2). Thus, the excess entropy discussed above makes a non-negligible contribution even in the thermodynamic limit. In a higher dimensional XY model, the excess entropy would still take the value ln(2) for a π twist. However, its contribution to the helicity modulus, $2\ln(2)L^{2-d}/\pi^2$, would vanish in the thermodynamic limit.

Our work also relates to some of the questions raised by Brown and Ciftan [45]. They studied the effects of twisted-periodic and anti-periodic boundary conditions on a three-dimensional classical Heisenberg model and discussed the notion of mixing states of different chiralities in response to twisted-periodic boundary conditions. However, they analyzed the internal energy cost of the twist rather than the free energy cost. The authors report deviations from a quadratic twist angle dependence of the internal energy cost somewhat similar to what we find for ΔF, but the magnitude of the deviation in their case is much larger than $T\ln(2)$. Moreover, the internal energy cost (as opposed to ΔF) is not expected to contain the entropy due to the mixing of chiralities. This suggests that the deviations from a quadratic twist angle dependence of the internal energy cost in Ref. [45] have a different origin. Specifically, Heisenberg spins can reduce the energy cost of twisted-periodic boundary conditions by tilting out of the plane in which the twist is applied. In contrast, they cannot avoid antiperiodic boundary conditions, in agreement with the fact that the energy cost of anti-periodic boundary conditions in Ref. [45] is much larger than that of even the largest twist angles. A quantitative analysis of the effects of twisted-periodic boundary conditions in the Heisenberg case remains a task for the future.

Our results have potential implications for experiments proposed to detect the BKT phase transitions [89], in which anti-parallel external fields would be used to study charge-current cross correlations. Moreover, in discrete spin systems such as the $q-$state clock model [90], twists are necessarily non-infinitesimal, and corrections to the infinitesimal-twist helicity modulus must be considered.

APPENDIX: HELICITY MODULUS FOR AN INFINITESIMAL TWIST

In this Appendix, we derive the expression (5) for the second derivative of the free energy on the twist angle. This expression allows the evaluation of helicity modulus for an infinitesimal twist in terms of correlation functions of the untwisted system. The derivation follows Refs. [68, 91].

Consider an XY magnet in d dimensions, of linear size L. Applying twisted boundary conditions (BC) along x axis implies that the spins at $x = 0$ make an angle Θ w.r.t. the spins at $x = L$. The change in free energy due to the twist can be parameterized as

$$\Delta F = \frac{1}{2}\rho_s V \left(\frac{\Theta}{L}\right)^2, \tag{17}$$

where $V = L^d$. In the limit of $\Theta \to 0$,

$$\rho_s = \frac{L^2}{V}\left(\frac{\partial^2 F}{\partial \Theta^2}\right)_{\Theta=0}. \tag{18}$$

The second derivative of the free energy can be evaluated by treating Θ as a parameter of the partition function.

To this end, we start from the Hamiltonian

$$H = -\sum_{<ij>} J\cos(\phi_i - \phi_j) \tag{19}$$

with boundary conditions $\phi_i = 0$ at $x_i = 0$ and $\phi_i = \Theta$ at $x_i = L$. We now perform a variable transformation $\psi_i = \phi_i - \Theta x_i/L$. Note that ψ_i has untwisted BC, $\psi_i = \phi_i = 0$ at $x_i = 0$ and $x_i = L$. The dependence on the twist angle Θ has been moved to the Hamiltonian

$$H = -\sum_{<ij>} J\cos(\psi_i + \Theta\frac{x_i}{L} - \psi_j - \Theta\frac{x_j}{L}) \ , \tag{20}$$

$$H = -\sum_{<ij>} J\cos(\psi_i - \psi_j - \frac{\Theta}{L}(x_i - x_j)) \ . \tag{21}$$

The evaluation of $(\partial^2 F/\partial\Theta^2)$ is now straight forward, starting from

$$F = -k_B T \ln(Z(\Theta)) = -k_B T \ln\left(\mathrm{Tr} e^{-\beta H}\right) \ . \tag{22}$$

First,

$$\begin{aligned}\frac{\partial F}{\partial\Theta} =& -k_B T\frac{1}{Z}\left(\frac{\partial Z}{\partial\Theta}\right)\\ \frac{\partial F}{\partial\Theta} =& \frac{1}{Z}\mathrm{Tr}\left(\frac{\partial H}{\partial\Theta}e^{-\beta H}\right) = \left\langle\frac{\partial H}{\partial\Theta}\right\rangle .\end{aligned}$$

Then,

$$\begin{aligned}\frac{\partial^2 F}{\partial\Theta^2} =& \frac{\partial}{\partial\Theta}\left(\frac{1}{Z}\mathrm{Tr}\left(\frac{\partial H}{\partial\Theta}e^{-\beta H}\right)\right)\\ \frac{\partial^2 F}{\partial\Theta^2} =& \beta\left\langle\frac{\partial H}{\partial\Theta}\right\rangle^2 + \left\langle\frac{\partial^2 H}{\partial\Theta^2}\right\rangle - \beta\left\langle\left(\frac{\partial H}{\partial\Theta}\right)^2\right\rangle .\end{aligned}$$

Each derivative in the above equation can be evaluated from Eq. (21).

$$\left(\frac{\partial H}{\partial\Theta}\right)_{\Theta=0} = \frac{1}{L}\sum_{<ij>} J\sin(\psi_i - \psi_j)(x_i - x_j) \tag{23}$$

$$\left(\frac{\partial^2 H}{\partial\Theta^2}\right)_{\Theta=0} = \frac{1}{L^2}\sum_{<ij>} J\cos(\psi_i - \psi_j)(x_i - x_j)^2 . \tag{24}$$

Collecting all the terms,

$$\left(\frac{\partial^2 F}{\partial \Theta^2}\right)_{\Theta=0} = \beta \left\langle \frac{\partial H}{\partial \Theta} \right\rangle^2_{\Theta=0} + \left\langle \frac{\partial^2 H}{\partial \Theta^2} \right\rangle_{\Theta=0} - \beta \left\langle \left(\frac{\partial H}{\partial \Theta}\right)^2 \right\rangle_{\Theta=0}. \tag{25}$$

The first term vanishes due to symmetry, but

$$\begin{aligned}\left(\frac{\partial^2 F}{\partial \Theta^2}\right)_{\Theta=0} =& \frac{1}{L^2} \left\langle \sum_{<ij>} J \cos(\psi_i - \psi_j)(x_i - x_j)^2 \right\rangle \\ & - \frac{\beta}{L^2} \left\langle \sum_{<ij>} \left\{ J \sin(\psi_i - \psi_j)(x_i - x_j) \right\}^2 \right\rangle\end{aligned}$$

where the thermodynamic averages $\langle ... \rangle$ are defined for $\Theta = 0$. In vector notation, $\cos(\psi_i - \psi_j) = \vec{S}_i \cdot \vec{S}_j$, $\sin(\psi_i - \psi_j) = -\hat{k} \cdot (\vec{S}_i \times \vec{S}_j)$. Thus,

$$\begin{aligned}\left(\frac{\partial^2 F}{\partial \Theta^2}\right)_{\Theta=0} =& \frac{1}{L^2} \sum_{<ij>} J \langle \vec{S}_i \cdot \vec{S}_j \rangle (x_i - x_j)^2 \\ & - \frac{\beta}{L^2} \left\langle \left\{ \sum_{<ij>} J(\hat{k} \cdot (\vec{S}_i \times \vec{S}_j)(x_i - x_j)) \right\}^2 \right\rangle.\end{aligned}$$

The $\Theta \to 0$ limit thus allows a simple evaluation of $(\partial^2 F / \partial \Theta^2)$ and of the helicity modulus ρ_s. This completes the derivation of Eq. (5).

ACKNOWLEDGEMENTS

We acknowledge support from the National Science Foundation under grant nos. DMR-1506152, DMR-1828489, OAC-1919789. Simulations were performed on the Foundry and Pegasus Clusters at Missouri University of Science and Technology. We would also like to thank John Chalker, Eduardo Fradkin, and Martin Hasenbusch for helpful correspondence and W. Joe Meese for valuable discussions.

III. PHASES AND PHASE TRANSITIONS OF THE DISORDERED QUANTUM CLOCK MODEL

Pulloor Kuttanikkad Vishnu[1],Gaurav Khairnar[2], Rajesh Narayanan[1] ,Thomas Vojta[2]
[1] Department of Physics, Indian Institute of Technology Madras, Chennai 600036, India
[2] Department of Physics, Missouri University of Science and Technology, Rolla, Missouri 65409, USA. Email: vojtat@mst.edu [7]

ABSTRACT

We study the phases and phase transitions of a disordered one-dimensional quantum q-state clock Hamiltonian using large-scale Monte Carlo simulations. Making contact with earlier results, we confirm that the clean, translational invariant version of the model, for $q = 6$, hosts an intermediate emergent quasi-long-range ordered (QLRO) phase between the symmetry-broken true long-range ordered (TLRO) phase and the disordered (paramagnetic) phase. With increasing disorder strength, the quasi-long-range ordered phase shrinks and finally vanishes at a multi-critical point, beyond which there is a direct transition from the TLRO phase to the paramagnetic phase. After establishing the phase diagram, we characterize the critical behaviors of the various quantum phase transitions in the model. We find that weak disorder is an irrelevant perturbation of the Berezinskii-Kosterlitz-Thouless transitions that separate the QLRO phase from the TLRO and paramagnetic phases. For stronger disorder, some of the critical exponents become disorder-dependent already before the system reaches the multicritical point. We also show that beyond the multicritical point, the direct transition from the TLRO phase to the paramagnetic phase is governed by an infinite-randomness critical point in line with strong-disorder renormalization group predictions. While our numerical results are for $q = 6$, we expect the qualitative features of the behavior to hold for all $q > 4$.

[7]Published: Physical Review B 111, 094212 (2025)

1. INTRODUCTION

The impact of quenched disorder on both quantum and classical phase transitions is a subject matter with a long and rich history (see, e.g., Ref. [9, 14, 92] for recent reviews). These studies have produced a welter of results ranging from the celebrated Harris [93] and Imry-Ma [94] criteria that predict the stability of phases and phase transitions against quenched impurities to the discoveries of numerous exotic phenomena close to disordered quantum phase transitions. These include infinite-randomness critical points and the attendant quantum Griffiths phases [95, 96, 97, 98, 99, 100] as well as smeared phase transitions [22, 25, 101].

The vast majority of work within this area has centered on studying the effects of impurity-induced randomness on phases that follow the Landau symmetry classification and the corresponding symmetry-breaking phase transitions. Relatively little is known about the effects of random disorder on other types of transitions including topological transitions that do not break the symmetry of a local order parameter. A well-known example is the Berezinskii-Kosterlitz-Thouless (BKT) transition [6, 102] that frequently obtains in (1+1)-dimensional quantum many-body systems with $O(2)$ [or $U(1)$] order parameter symmetry or, equivalently, in the corresponding classical statistical models in two space dimensions, such as the two-dimensional XY model. These transitions correspond to the binding and unbinding of vortex/anti-vortex pairs and demarcate a phase with exponentially decaying order parameter correlations from a critical, quasi-long-range ordered (QLRO) phase characterized by power-law decay of the correlations.

Interestingly, such critical or massless phases, accompanied by BKT transitions, can also occur when the $O(2)$ order parameter symmetry is broken down into q discrete values, evenly spaced on the unit circle, resulting in a discrete Z_q symmetry. Extensive studies of the ferromagnetic q-state quantum clock model in one space dimension (and its two-dimensional classical analog) [103, 104, 105, 106, 107, 108, 109, 110, 110, 111, 112, 113, 114, 115, 116, 117, 118, 119, 120, 121, 122, 123, 124, 125, 126], have shown that

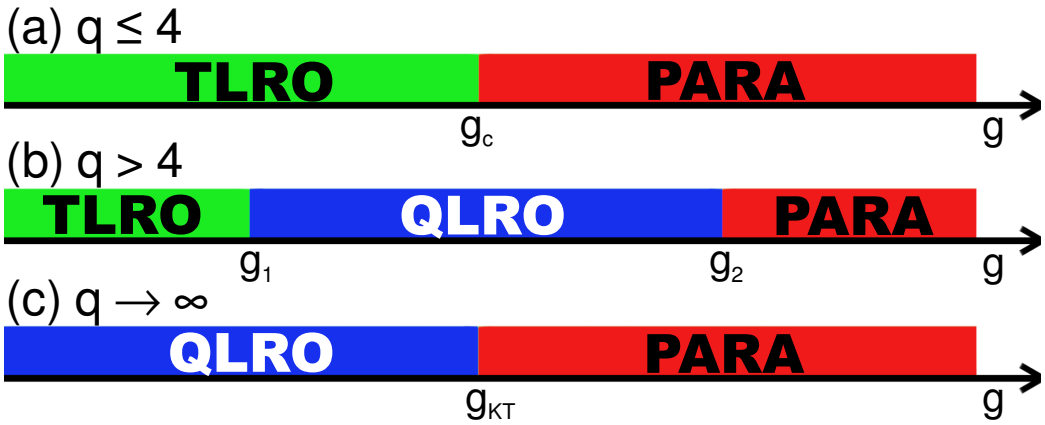

Figure 1. Phases of the one-dimensional q-state quantum clock model for (a) $q \leq 4$ (b) $q > 4$ and (c) $q \to \infty$ in the absence of quenched randomness. g denotes the parameter used to tune the system through the transition.

such systems host a QLRO phase that intervenes between a symmetry-broken truly long-range ordered (TLRO) phase, and a disordered (paramagnetic, in the language of magnetic systems) phase for all $q > 4$. This is illustrated in Fig. 1. In contrast, a direct transition from the symmetry-broken to the disordered phase obtains for all $q \leq 4$.

Physical realizations of the q-state clock model are manifold: For instance, the planar-to-buckled instability in two-dimensional lattices of ions can be understood via a mapping to a six-state clock model [127]. Other physical manifestations of the six-state clock model include the half-filled extended Hubbard model on a triangular lattice in the atomic limit [128], the displacive structural phase transition in certain two-dimensional solids [129], the two-dimensional frustrated Heisenberg antiferromagnet on a windmill lattice [130, 131, 132], the Blume-Capel antiferromagnet on a triangular lattice [133], a triangular-lattice antiferromagnetic Ising model with a spatially anisotropic next-nearest-neighbor ferromagnetic coupling [134], stacked triangular antiferromagnetic Ising models [135, 136], BKT phase transitions in a Kagome spin ice system [137, 138], the melting of

three-sublattice order in triangular and Kagome antiferromagnets [139], the domain pattern in certain layered hexagonal materials [140], and the melting of magnetic order in frustrated triangular rare earth magnets [141].

The impact of (weak) quenched disorder on a system exhibiting a BKT transition was studied in the seminal work by Giamarchi and Schulz [142], harnessing a perturbative renormalization group (RG). This approach was later extended to second order in the disorder strength by Ristivojevic et al. [143]. Set in the context of the superfluid-insulator transition of disordered 1D bosons, these studies concluded that the BKT transition features universal critical exponents and a universal value of the Luttinger parameter. In contrast, a strong-disorder renormalization group (SDRG) calculation by Altman et al. [144, 145, 146] predicted that the superfluid-insulator transition belongs to a disordered BKT universality class featuring non-universal, disorder-dependent exponents and a non-universal value of the Luttinger parameter, at least for sufficiently strong quenched disorder. In the following years, the question of whether or not quenched disorder can change the critical behavior of a BKT transition and, if so, the nature of the resulting transition was controversially discussed in the literature (see, e.g. Refs. [147, 148, 149, 150, 151] and references therein). To the best of our knowledge, a full resolution to this problem has not been achieved, yet. However, there seems to be a consensus that sufficiently strong disorder can lead to a transition that is different from the Giamarchi-Schulz scenario and governed by the physics of broadly distributed weak links. Most of the above work considered the one-dimensional Bose gas problem with diagonal disorder. Hrahsheh and Vojta [152] performed large-scale Monte-Carlo simulations for the particle-hole symmetric case with the off-diagonal disorder (which maps onto a classical XY-model with the columnar disorder). In analogy with the Bose glass results, they found that the critical behavior is universal (and identical to the clean case) for the weak disorder but becomes non-universal and disorder-dependent for the stronger disorder.

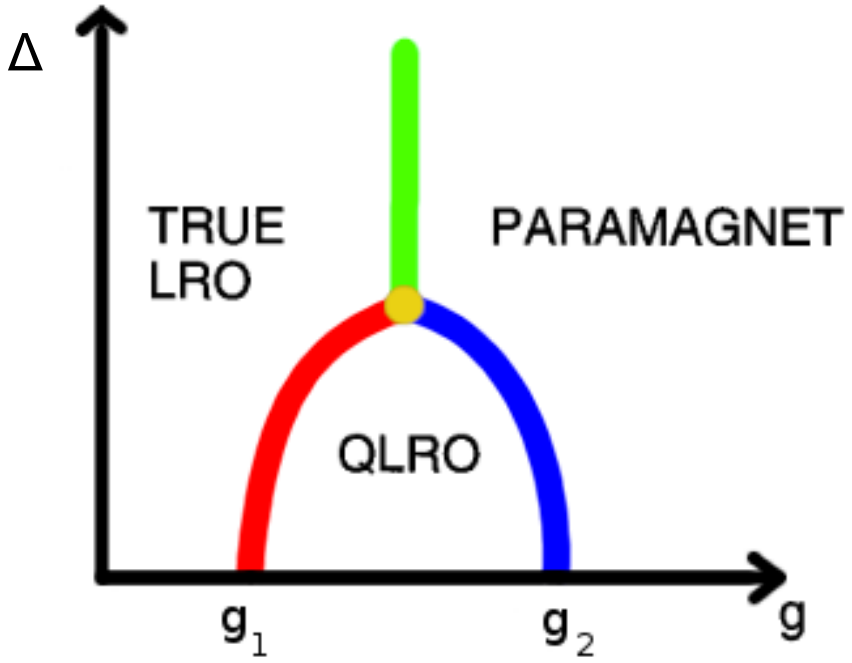

Figure 2. Schematic phase diagram for disordered quantum clock model as proposed in Ref. [153]. g denotes the quantum tuning parameter, and Δ is the disorder strength.

The effect of quenched impurities on the one-dimensional quantum clock model was analyzed by Senthil and Majumdar by laying recourse to an SDRG treatment [153]. Their results, valid for sufficiently strong randomness, yield a direct transition of infinite-randomness type from the disordered (paramagnetic) phase to the symmetry-broken (TLRO) phase. This suggests that the size of the intermediate QLRO phase decreases with increasing disorder strength, leading to the schematic phase diagram in Fig. 2, proposed in Ref. [153]. At lower disorder strengths (not compatible with the SDRG technique), an earlier DMRG study showed the existence of disorder-dependent exponents across the transition from the QLRO phase to the paramagnetic phase [154].

In the present manuscript, we report the results of a comprehensive study of the one-dimensional disordered quantum clock model (focusing on $q = 6$ as a prototypical case for all $q > 4$) by means of Monte Carlo simulations. We construct the phase diagram as a function of quantum fluctuation strength and disorder, spanning the range from the

clean limit all the way to the strong disorder regime. The paper is organized as follows: In Sec. 2, we introduce the quantum clock Hamiltonian and its mapping to a two-dimensional classical clock model. Details of the Monte-Carlo simulations are presented in Sec. 3 along with a discussion of the various observables and their expected scaling behavior. In Sec. 4, we discuss the results of our simulations, which encompasses a discussion of the phase diagram as well the properties of the various phase transitions in the weak and strong-disorder regimes. Finally, we set forth our conclusions in Sec. 5.

2. MODEL

To define the Hamiltonian of the one-dimensional disordered quantum clock model, consider a chain of lattice sites j. Each site is occupied by a q-state clock variable having eigenstates $|p_j\rangle$ with $p_j = 0, 1, \ldots, q-1$. Written in the clock-state basis, the Hamiltonian reads

$$H = -\sum_j J_j \cos\left[\frac{2\pi(p_j - p_{j+1})}{q}\right] - \sum_j \frac{h_j}{2}\left(\hat{\Gamma}_j + \hat{\Gamma}_j^\dagger\right) . \tag{1}$$

The raising and lowering operators are defined by $\hat{\Gamma}^\dagger|p\rangle = |(p+1) \mod q\rangle$ and $\hat{\Gamma}|p\rangle = |(p-1) \mod q\rangle$. The energies J_j and h_j represent the nearest-neighbor couplings and "transverse field" terms, respectively, at site j. In the limit $q \to \infty$, the Hamiltonian maps onto a quantum rotor model whereas the $q = 2$ case reduces to the transverse field Ising model.

In preparation for the Monte Carlo simulations we now employ the quantum-to-classical mapping method (see, e.g., Ref. [3]) that recasts the partition function of a d-dimensional quantum model as the partition function of an equivalent classical model in $D = d + 1$ dimensions. In our case, the mapping, which is detailed in Appendix A leads from the one-dimensional quantum Hamiltonian (1) to a classical clock model in $D = 2$

space dimensions. The resulting classical Hamiltonian reads

$$H_{\mathrm{cl}} = -\sum_{j,\tau} J_j^s \cos\left[\frac{2\pi(p_{j,\tau} - p_{j+1,\tau})}{q}\right] - \sum_{j,\tau} J_j^t \cos\left[\frac{2\pi(p_{j,\tau} - p_{j,\tau+1})}{q}\right] . \tag{2}$$

Here, the coordinates j and τ correspond to the real-space and imaginary-time positions, respectively, in the original quantum problem. In the following, we treat interactions J_j^s and J_j^t as constants and tune the strength of the fluctuations by varying the "classical" temperature T of the model (2). Thus, the classical temperature plays the role of the quantum tuning parameter g in Fig. 2, and T_{c1} and T_{c2} will denote the transition temperatures from the TLRO phase to the QLRO phase and from the QLRO phase to the disordered (paramagnetic) phase, respectively.

The universal features of the phase diagram and phase transitions are shared by the quantum model (1) and its classical counterpart (2). Analyzing the classical model by means of classical Monte Carlo simulations allows us to employ cluster algorithms that are highly efficient even in the presence of disorder, giving us the ability to study large system sizes that reduce finite-size effects and probe the thermodynamic limit [8].

Quenched random disorder can be introduced into the quantum Hamiltonian (1) by making J_j and h_j independent random variables. The quantum-to-classical mapping implies that such spatially uncorrelated disorder in the quantum Hamiltonian corresponds to columnar disorder in the classical model (2), i.e., disorder that is perfectly correlated along the imaginary time direction [155, 156][9]. Consequently, both interactions in the classical model, J_j^s and J_j^t, are only functions of the spatial index j. A pictorial representation of such a lattice with correlated impurities is shown in Fig. 3. As the disorder breaks the symmetry

[8] in contrast, the presence of quenched disorder tends to curtail the efficiency of other simulation techniques for quantum many-particle systems such as DMRG or tensor-network based methods.

[9] For the sake of completeness we refer the reader to [157], where the two-dimensional classical clock model is studied in the presence of completely uncorrelated quenched randomness.

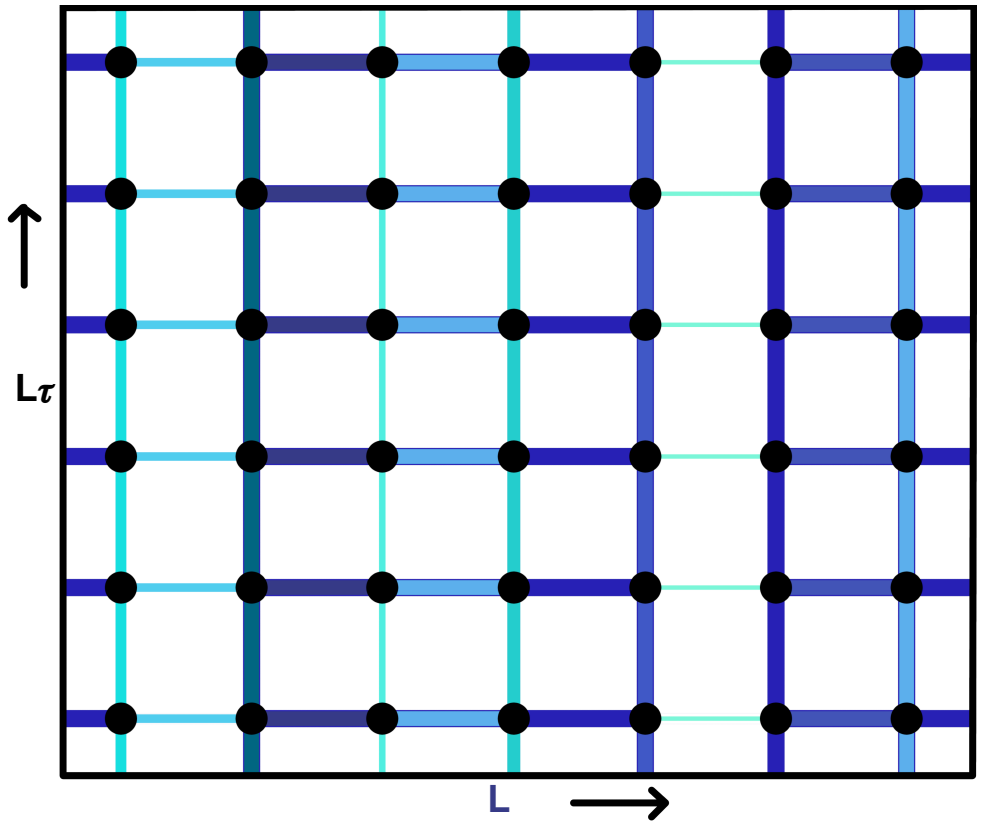

Figure 3. Schematic of a lattice with the correlated disorder in both horizontal (space-like) and vertical (imaginary-time-like) bonds. Different colors (shading) indicate different coupling strengths.

between the two directions, we need to specify two different linear system sizes L and L_τ in the space and imaginary-time directions, respectively, and treat them as independent parameters.

We assume the interactions J_j^s and J_j^t to be independent random variables, drawn from the power-law distribution

$$P(J) = \frac{1}{\Delta} J^{(-1+\frac{1}{\Delta})} . \tag{3}$$

with $0 < J \leq 1$. The parameter Δ can take values between 0 and ∞ and serves as a measure of the disorder strength. The clean limit (uniform J) is recovered when $\Delta = 0$ and the distribution becomes arbitrarily broad (on a logarithmic scale) in the limit $\Delta \to \infty$.

The universal features of the phase diagram and the phase transitions are expected to be independent of the details of the disorder distributions. To test this, we have also performed some calculations with a binary disorder distribution as used in Ref. [152]. We will return to this question in Sec. 5.

3. METHODS

3.1. SIMULATION DETAILS

We use large-scale Monte Carlo simulations to study the classical Hamiltonian (2) for $q = 6$, using interactions drawn from the distribution (3). The simulations combine the single-spin-flip Metropolis algorithm [71] and the Wolff cluster algorithm [37]. The Wolff cluster algorithm proves beneficial near phase transitions where a single-spin-flip algorithm suffers critical slowing down, and the Metropolis algorithm helps equilibrate small clusters of sites that are isolated from the rest of the chain by weak links. A full Monte Carlo sweep consists of one Metropolis sweep over the lattice followed by one Wolff cluster sweep (a number of cluster flips such that the total number of flipped spins equals the number of lattice sites).

The quality of the Monte Carlo equilibration is benchmarked, as usual, by comparing simulation runs with hot starts (the clock variables take random values initially) and cold starts (all clock variables take the same value initially). These tests do not show a significant dependence of the required equilibration times on the disorder strength. However, we moderately increase the number of Monte Carlo sweeps with increasing disorder strength to help reduce the additional statistical error stemming from the disorder fluctuations. Specifically, we employ 2000 equilibration sweeps and 5000 measurement sweeps for low disorder strengths, whereas we utilize 4000 equilibration sweeps and 10000 measurement sweeps for higher disorder strengths.

We simulate systems of linear sizes up to $L = 320$ in the space direction and up to $L_\tau = 15000$ in the imaginary-time direction, exploring disorder strength from $\Delta = 0$ to $\Delta = 2$. All results are averaged over a large number of disorder realizations, ranging from 2000 samples for lower disorder strengths to 10000 samples for higher disorder strengths.

3.2. OBSERVABLES

We now turn to the observables measured in the simulations. For definiteness, we are using the language of magnetic systems. First, we define the order parameter, the complex magnetization [158]

$$\mathbf{M} = \frac{1}{N} \sum_{j,\tau} e^{i\theta_{j,\tau}} = |\mathbf{M}| e^{i\phi} \,, \tag{4}$$

where $\theta_{j,\tau} = 2\pi p_{j,\tau}/q$ is the phase of the clock variable at the site (j, τ) and $N = L\, L_\tau$ denotes the total number of sites. This complex magnetization is the building block of several of our primary observables. The average magnetization m is given by

$$m = [\langle |\mathbf{M}| \rangle]_{\text{dis}} \,. \tag{5}$$

Here, the angular brackets $\langle \cdots \rangle$ indicate the thermodynamic (Monte Carlo) average, and $[\cdots]_{\text{dis}}$ denotes the average over the quenched disorder realizations. The corresponding, disorder averaged susceptibility is

$$\chi = (N/T) \left[\langle |\mathbf{M}|^2 \rangle - \langle |\mathbf{M}| \rangle^2 \right]_{\text{dis}} \,, \tag{6}$$

and the Binder cumulant [159] is given by

$$U_m = \left[1 - \frac{\langle |\mathbf{M}|^4 \rangle}{2 \langle |\mathbf{M}|^2 \rangle^2} \right]_{\text{dis}} \,. \tag{7}$$

To identify the transition between the QLRO and TLRO phases, we also define a clock order-parameter [158],

$$m_\phi = \left[\langle \cos(q\phi)\rangle\right]_{\rm dis} . \tag{8}$$

It vanishes in the paramagnetic phase as well as the QLRO phases, because the distribution of the global order parameter phase ϕ on the interval $[0, 2\pi)$ is uniform. In the TLRO phase, in contrast, the system spontaneously freezes in one of the q clock states which implies that the ϕ distribution develops maxima at multiples of $2\pi/q$, rendering m_ϕ nonzero.

In addition to these magnetization-based observables, we also measure the disorder-averaged specific heat,

$$C = (N/T^2)\left[(\langle E^2\rangle - \langle E\rangle^2)\right]_{\rm dis} , \tag{9}$$

and the correlation lengths in the spatial and imaginary-time directions. They are obtained from the second moment of the spin-spin correlation function and can be expressed as follows [160, 161, 162, 163],

$$\begin{aligned} \xi_s &= \left[\left(\frac{\tilde{G}(0,0) - \tilde{G}\left(k_{s0},0\right)}{k_{s0}^2 \tilde{G}\left(k_{s0},0\right)}\right)^{1/2}\right]_{\rm dis} , \\ \xi_\tau &= \left[\left(\frac{\tilde{G}(0,0) - \tilde{G}\left(0,k_{\tau 0}\right)}{k_{\tau 0}^2 \tilde{G}\left(0,k_{\tau 0}\right)}\right)^{1/2}\right]_{\rm dis} . \end{aligned} \tag{10}$$

Here, $\tilde{G}\left(k_{s0}, k_{\tau 0}\right)$ is the Fourier transform of the correlation function, while $k_{s0} = 2\pi/L$ and $k_{\tau 0} = 2\pi/L_\tau$ are the minimum values of the wave numbers in space and imaginary-time directions, respectively.

Finally, we also study the helicity modulus or spin stiffness, which measures the free energy cost of twisted boundary conditions, which can be implemented by fixing the spins at two opposite boundaries at specific phases, with a fixed angle Θ between them. For systems with a continuous $U(1)$ or $O(2)$ symmetry, the helicity modulus is usually defined

as the response to an infinitesimal twist via

$$\rho_s = \left(\frac{\partial^2 F}{\partial \Theta^2}\right)_{\Theta=0} L^{2-D} \,, \tag{11}$$

where F is the total free energy.

For the q-state clock model, any twists of the boundary conditions are necessarily non-infinitesimal. We, therefore define the helicity modulus as the response to a finite twist Θ,

$$\rho_s(\Theta) = \frac{2\Delta F}{\Theta^2} L^{2-D} \,, \tag{12}$$

where $\Delta F = F_\Theta - F_0$ is the difference between free energies of the twisted and untwisted systems [116]. In the Monte Carlo simulations, we do not implement fixed boundary conditions but rather compare the free energies of periodic and twisted-periodic boundary conditions. For the latter, we modify the interaction across one of the boundaries to $-J_j^s \cos\left[2\pi(p_{j,\tau} - p_{j+1,\tau})/q - \Theta\right]$.

The free energy cannot be measured directly in a Monte Carlo simulation. We evaluate the free energies explicitly by integrating the (disorder averaged) internal energy $U = [\langle H_{\rm cl}\rangle]_{\rm dis}$,

$$F(T) = F(T_0) + T\int_{\beta_0}^{\beta} d\beta' U(\beta') \,, \tag{13}$$

where $\beta = 1/T$. The starting point T_0 of the integration is chosen sufficiently high, i.e., deep in a paramagnetic phase where the twist in the boundary conditions does not matter, and $F(T_0)$ for the twisted and the untwisted systems are identical. This ensures that $F(T_0)$ drops out of the free energy difference ΔF in Eq. (12). For our helicity modulus calculations, we fix $T_0 = 30$ (much larger than the critical temperature of the clean system) and use a temperature step $dT = 0.02$ in the numerical integration (13). We have tested T_0 values as high as 50 and temperature steps as small as 0.01, with unchanged results.

To estimate the statistical error of F, we follow an ensemble method (see, e.g., Ref. [164]): After each Monte Carlo run, we generate 100 artificial internal energy data sets $U_a(T) = U(T) + r\delta U(T)$, where r is a random number taken from a normal distribution of unit variance and $\delta U(T)$ is the Monte Carlo error estimate of $U(T)$. We evaluate $F_a(T)$ for each $U_a(T)$ using the integration (13). The mean and standard deviation of the set of $F_a(T)$ give $\langle F(T)\rangle$ and its error $\delta F(T)$.

The helicity modulus can be used to identify the transition between the paramagnetic to QLRO phases as well as the transition between the QLRO and TLRO phases. In the paramagnetic phase, the free energy difference ΔF vanishes as $\Delta F \sim e^{-L/\xi}$, where ξ is correlation length. Consequently, $\rho_s = 0$ in the thermodynamic limit. In the ordered phase, due to the presence of domain walls, ρ_s diverges in the thermodynamic limit. In the intermediate QLRO phase, ρ_s is expected to be nonzero and finite.

As the classical Hamiltonian (2) is anisotropic in the presence of quenched disorder, we need to distinguish the helicity modulus ρ_s for a twist in the space direction from the helicity modulus ρ_τ for a twist in the imaginary time direction. In the quantum-to-classical mapping, the latter is related to the compressibility κ of the original quantum Hamiltonian (1). Correspondingly, the Luttinger parameter $\tilde{g} = \pi\sqrt{\rho_s\kappa}$ of the quantum Hamiltonian is given by $\tilde{g} = (\pi/T)\sqrt{\rho_s\rho_\tau}$ in our simulations. In the clean limit, the classical Hamiltonian is isotropic, implying $\rho_s = \rho_\tau$.

At a BKT transition, the value of the Luttinger parameter is expected to be universal. According Kosterlitz and Nelson [75], the Luttinger parameter at the paramagnetic-to-QLRO transition at T_{c2} is given by $\tilde{g} = 2$, or equivalently by $\sqrt{\rho_s\rho_\tau} = 2T_{c2}/\pi$. Analogously, the helicity moduli at the QLRO-TLRO transition at T_{c1} are expected to fulfill the relation $\sqrt{\rho_s\rho_\tau} = q^2T_{c1}/8\pi$ [103].

In our Monte Carlo calculations of the helicity modulus, we choose a twist of $\Theta = \pi$ which corresponds to anti-periodic boundary conditions. This has the advantage that the efficient Wolff cluster algorithm can be employed, whereas this would not be possible for

twisted bonds $-J_j^s \cos\left[2\pi(p_{j,\tau} - p_{j+1,\tau})/q - \Theta\right]$ with $0 < \Theta < \pi$. As pointed out in Ref. [164], at $\Theta = \pi$, the thermodynamic ensemble consists of an equal mixture of states with opposite chiralities. This leads to an additional $\ln(2)$ entropy contribution in the QLRO and TLRO phases and a corresponding correction to F. Including this correction in the definition (12), shows that the helicity moduli at $\Theta = \pi$ are reduced by

$$\Delta\rho_{s,\tau} = -\frac{2\ln 2}{\pi^2} T \tag{14}$$

compared to their values for small twist angles. This can be accounted for either by correcting the helicity modulus values arising from the simulations or by appropriately modifying the Jose-Kadanoff and Kosterlitz-Nelson relations.

3.3. FINITE-SIZE SCALING

In this section, we concentrate on the data analysis for the various observables introduced in Sec. 3.2 by means of finite-size scaling (FSS). As the quenched randomness breaks the symmetry between the space and imaginary time directions, the behavior close to a phase transition is governed by two independent scaling variables (dimensionless ratios between system size and correlation length), viz., L/ξ_s and L_τ/ξ_τ. At a conventional critical point, the correlation lengths in both space and imaginary time are expected to diverge as powers of the distance $r = (T - T_c)/T_c$ from criticality, $\xi_s \sim |t|^{-\nu}$ and $\xi_\tau \sim \xi^z \sim |t|^{-\nu z}$, where ν and z are the correlation length and dynamical critical exponents, respectively. The scaling form of dimensionless observables such as the Binder cumulant therefore reads

$$U_m(r, L, L_\tau) = \tilde{U}_m(rL^{1/\nu}, L_\tau/L^z) \; . \tag{15}$$

Here, $\tilde{U}_m$ is the scaling function. The clock order parameter m_ϕ at a conventional transition fulfills the same scaling form [165],

$$m_\phi(r, L, L_\tau) = \tilde{m}_\phi(rL^{1/\nu}, L_\tau/L^z) \ . \tag{16}$$

However, these scaling forms are not expected to hold at a BKT transition at which the correlation length depends exponentially on the distance from criticality, $\ln(\xi_s) \sim r^{-1/2}$ [102]. The exponential dependence is reflected in the scaling forms

$$U_m(r, L, L_\tau) = \tilde{U}_m(r \log(L/L_0)^2, L_\tau/L^z) \ , \tag{17}$$

$$m_\phi(r, L, L_\tau) = \tilde{m}_\phi(r \log(L/L_0)^2, L_\tau/L^z) \ , \tag{18}$$

where L_0 is a microscopic length scale.

Certain quantum phase transitions and nonequilibrium phase transitions in disordered systems feature exotic infinite-randomness critical points. Examples include the random transverse-field Ising ferromagnet [95, 96], the superconductor-metal quantum phase transition observed in thin nanowires [99, 100] and the disordered contact process [166, 167, 168]. In the infinite-randomness scenario, the power-law dependence of ξ_τ on ξ_s is replaced by an exponential (activated) scaling relation $\log(\xi_\tau) \sim \xi_s^\psi$, where ψ is the tunneling exponent. In such a scenario the scaling forms of U_m and m_ϕ are modified to read

$$U_m(r, L, L_\tau) = \tilde{U}_m(rL^{\frac{1}{\nu}}, \log(L_\tau/L_{\tau 0})/L^\psi) \ , \tag{19}$$

$$m_\phi(r, L, L_\tau) = \tilde{m}_\phi(rL^{\frac{1}{\nu}}, \log(L_\tau/L_{\tau 0})/L^\psi) \ . \tag{20}$$

The FSS of the clock order parameter and the Binder cumulant can be used to find the transition temperatures T_{c1} and T_{c2}, respectively. Focusing first on the Binder cumulant, we follow the treatment elucidated in Ref. [169]. It is based on the fact that U_m develops a maximum as a function of L_τ for fixed L and T. The position $L_\tau^{\max}$ of

this maximum characterizes the "optimal" sample shape at which the correlations extend equally in both directions. Setting $L_\tau = L_\tau^{\max}$ fixes the second argument of the scaling function $\tilde{U}_m$. Consequently, the peak value $U_m^{\max}$ is independent of the system size L at criticality, $r = 0$ ($T = T_{c2}$). Moreover, for the case of power-law dynamical scaling, one gets a scaling collapse of the Binder cumulant at $r = 0$ as a function of $L_\tau/L_\tau^{\max}$. If the dynamical scaling is instead of the activated type, a data collapse obtains if U_m is plotted as a function of the variable $\log(L_\tau)/\log(L_\tau^{\max})$. The clock order parameter can be analyzed in the same way to find the transition between the TLRO and QLRO phases at T_{c1}.

Further information about the phase transitions can be gained from the finite-size dependence of the disorder-averaged magnetization right at the transition point. At a conventional phase transition, it is expected to follow a power-law form and often characterized by means of the critical exponent combination β/ν,

$$m(T_c, L) \sim L^{-\beta/\nu} \tag{21}$$

where β is the order parameter exponent. β/ν can be connected to the anomalous (correlation function) exponent η via a scaling relation which reads $\eta = 2 - d - z + 2\beta/\nu$ in a quantum system with d space dimensions and dynamical exponent z. Thus, the finite-size dependence of the magnetization can also be expressed as

$$m(T_c, L) \sim L^{-(d+z-2+\eta)/2}\,. \tag{22}$$

This form is more convenient for BKT transitions for which ν is formally infinite, and β is not well defined as the order parameter vanishes on both sides of the transition.

For $d = 1$ and $z = 1$, eq. (22) reduces to the familiar relation $m \sim L^{-\frac{\eta}{2}}$ which is expected to hold in the entire QLRO phase and at the two BKT transitions at T_{c1} and T_{c2} [117, 158]. This allows us to extract the anomalous exponent η at both T_{c1} and T_{c2} as discussed in the Ref. [107]. In the absence of disorder, η is known to take the value $1/4$

at the transition between the QLRO and paramagnetic phases at T_{c2}. On the other hand, the theoretical estimate of the exponent at the transition between the TLRO and the QLRO transition is $\eta = 4/q^2$.

4. RESULTS AND DISCUSSIONS

In this section, we apply our simulation and data analysis techniques to the classical Hamiltonian (2). We first study the clean, translationally invariant case to test our methods. In Sec. 4.2, we establish the phase diagram of the disordered model. Finally, Sec. 4.3 and Sec. 4.4 are devoted to the study of the critical behavior of the model in the weak and strong disorder regimes, respectively.

4.1. CLEAN CASE

In order to identify the phase transitions of the clean ($\Delta = 0$) 6-state clock Hamiltonian (2), we analyze the clock order parameter m_ϕ and the Binder cumulant U_m. Figure 4 depicts m_ϕ and U_m as functions of the temperature T for different system sizes L. As the symmetry between the space and imaginary time directions is not broken in the clean case, fixing the dynamical exponent at $z = 1$, we use square, $L \times L$, samples. To extract the transition temperatures T_{c1}, and T_{c2}, we find the crossing point $T^*(L)$ of the curves of the relevant observable at two different system sizes, L and aL, where a is a constant. (We employ $a = \sqrt{2}$ in the following.) The crossing points shift as a function of system size because of corrections to scaling. At a BKT transition, this shift is expected to follow the functional form [158]

$$T^*(L) - T_c \sim (\ln L)^{-2} \, . \tag{23}$$

Here, T_c is the corresponding asymptotic critical temperature (T_{c1} for the crossings of m_ϕ and T_{c2} for the crossings of U_m). The extrapolations of $T^*(L)$ to infinite system size are shown in Fig. 5, they yield $T_{c1} = 0.695(8)$ and $T_{c2} = 0.895(8)$.

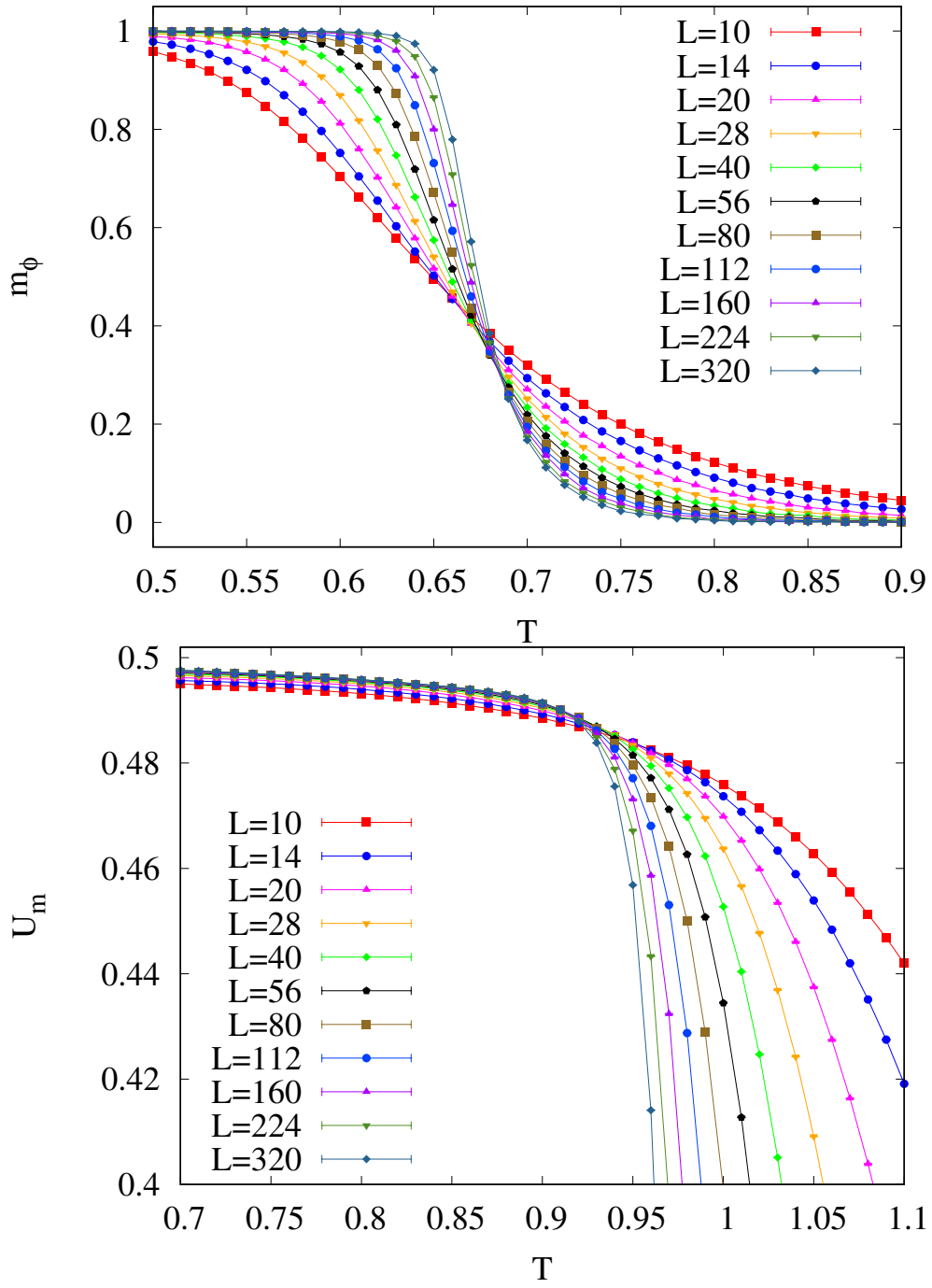

Figure 4. Clock order parameter m_ϕ and Binder cumulant U_m of the clean system ($\Delta = 0$) as functions of temperature T for several linear system sizes L. The statistical errors are smaller than the symbol size. The critical temperatures T_{c1}, T_{c2} can be determined from intersections of m_ϕ and U_m curves, respectively. Corrections to finite-size scaling systematically shift the intersection point T^*.

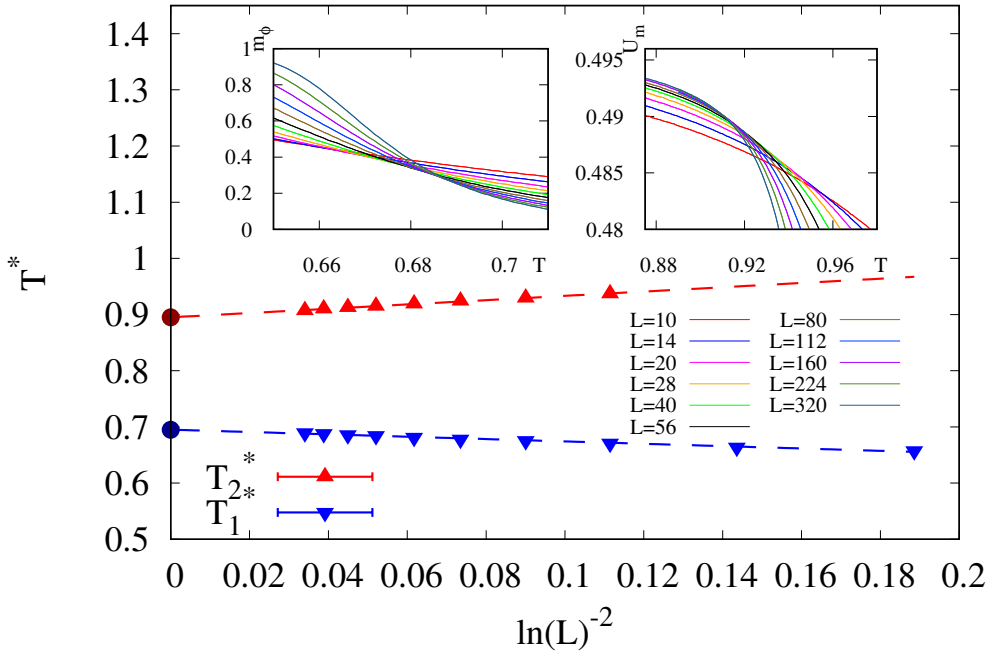

Figure 5. Extrapolation of the crossing temperatures $T^*(L)$ of m_ϕ (bottom, blue) and U_m (top, red) in the clean case to infinite system size. The transition temperatures are obtained as the intercepts on the y-axis from fits using $T^*(L) = T_c + A(\ln L)^{-2}$, yielding $T_{c1} = 0.695(8)$ and $T_{c2} = 0.895(8)$. The insets show m_ϕ (left) and U_m (right) close to the respective transitions.

Alternatively, we can lay recourse to the helicity modulus ρ_s to extract the transition temperatures T_{c1} and T_{c2}. As the clean system is isotropic, implying $\rho_\tau = \rho_s$, we only compute the spatial helicity modulus ρ_s. Our simulation results for $\rho_s(\pi)$ are shown in Fig. 6 as functions of temperature for various system sizes. Because we employ a twist of $\Theta = \pi$, we use the modified Jose-Kadanoff and Kosterlitz-Nelson relations, as discussed in Sec. 3.2. Due to the presence of finite size corrections, these lines do not intersect with the helicity modulus curves at a single point. Instead, there is a systematic shift of the intersection points with L. The critical temperatures are obtained by extrapolating the intersection temperatures $T^*(L)$ to the thermodynamic limit according to Eq. (23). From the fits, we obtain $T_{c1} = 0.707(2)$ and $T_{c2} = 0.895(6)$, which agrees with the results from

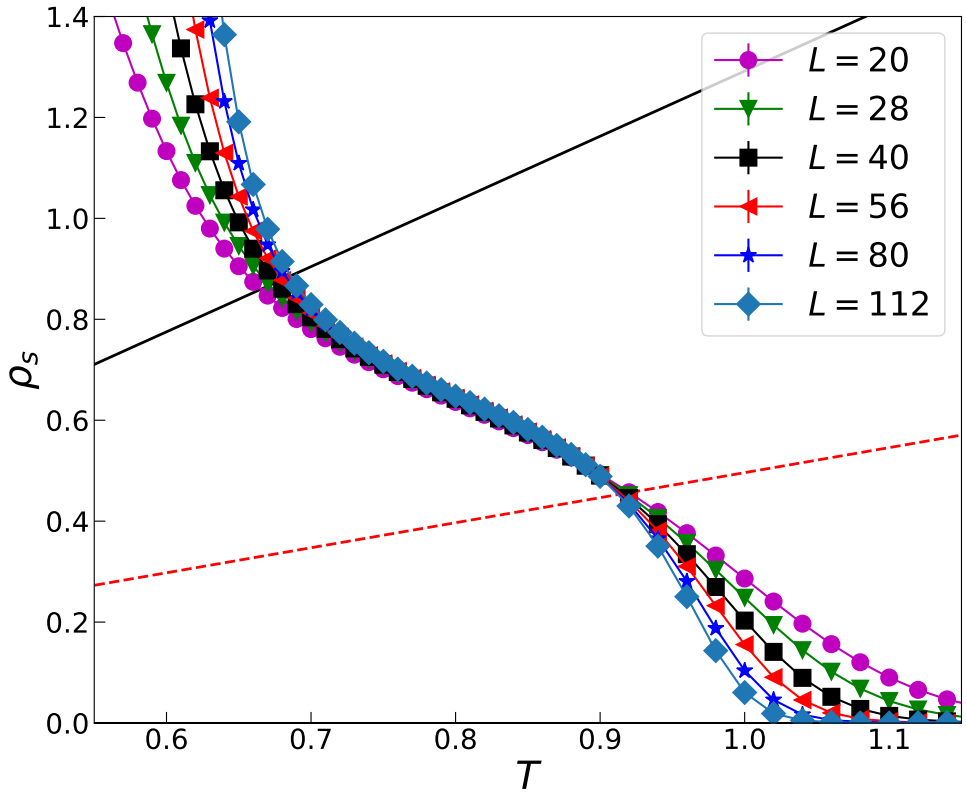

Figure 6. Helicity modulus ρ_s for twist angle $\Theta = \pi$ vs. temperature T for different linear system sizes L in the clean case, $\Delta = 0$. The solid (black) line corresponds to the modified Jose-Kadanoff relation $\rho_s = T(q^2/8\pi - 2\ln 2/\pi^2)$, and the dashed (red) line depicts the modified Kosterlitz-Nelson relation $\rho_s = T(2/\pi - 2\ln 2/\pi^2)$. The critical temperatures are obtained by extrapolating the crossing temperatures $T^*(L)$ between these lines and the data to $L \to \infty$ according to the BKT ansatz (23). We find $T_{c1} = 0.707(2)$ and $T_{c2} = 0.895(6)$.

m_ϕ and U_m. Moreover, these transition temperatures also agree reasonably well with recent high-accuracy results for the clean 6-state clock model in the literature, see, e.g., Table I in Ref. [124] [10]

[10] Some of the recent studies of the clean 6-state clock model quote very tight error bars for T_{c1} and T_{c2}. Note, however, that the error bars of different results often do not overlap, casting some doubt on the precision of at least some of the estimates.

4.2. DISORDERED CASE: PHASE DIAGRAM

We now turn our attention to the disordered clock model ($\Delta > 0$). We first study the specific heat as it is sensitive to all phase transitions in the system. Figure 7(a) presents the specific heat C for various disorder strengths as a function of temperature for a fixed system of size $L = L_\tau = 128$. In the clean limit, $\Delta = 0$, the specific heat clearly displays a double peak structure indicative of two phase transitions at T_{c1} and T_{c2}, identified in Sec. 4.1. Note that the specific heat at a BKT transition features only a weak (unobservable) essential singularity right at T_c, but a broad peak appears slightly above T_c due to the entropy release from the vortex-pair unbinding. Thus, the peak positions in Fig. 7(a) do not exactly coincide with the transition temperatures. The BKT character of the transition also implies that the specific heat shows only weak system-size effects. We have explicitly confirmed that the specific heat for $L = L_\tau = 256$ is almost identical to the result for $L = L_\tau = 128$ presented in the figure. The absence of a specific heat divergence at T_c is in line with the Harris criterion [93], as will be discussed in more detail in Sec. 4.3.

With increasing disorder strength Δ, the two peaks in the specific heat curves come closer to each other, indicating the shrinking and potential destruction of the QLRO phase. The behavior of the specific heat is mirrored by the behavior of the magnetization m in Fig. 7(b): For zero and weak disorder, we see a shoulder-like feature indicative of the intermediate QLRO phase [110]. This feature shrinks and disappears with increasing disorder strength, indicating the loss of the QLRO phase.

To construct the temperature-disorder phase diagram of the disordered clock model (2) quantitatively, we lay recourse to the methods employed for the clean case in Sec. 4.1, i.e., we determine the phase transition temperatures from the behavior of m_ϕ, U_m, ρ_s, and ρ_τ. A prototypical example for the analysis of m_ϕ and U_m in the disordered case is presented in Fig. 8 for $\Delta = 0.3$. It gives the transition temperatures $T_{c1} = 0.530(5)$ and $T_{c2} = 0.625(10)$. The helicity moduli can also be used to glean T_{c1}, and T_{c2}. In the presence of disorder, ρ_s and ρ_τ are not identical anymore. As discussed in Sec. 3.2, we therefore need to analyze the

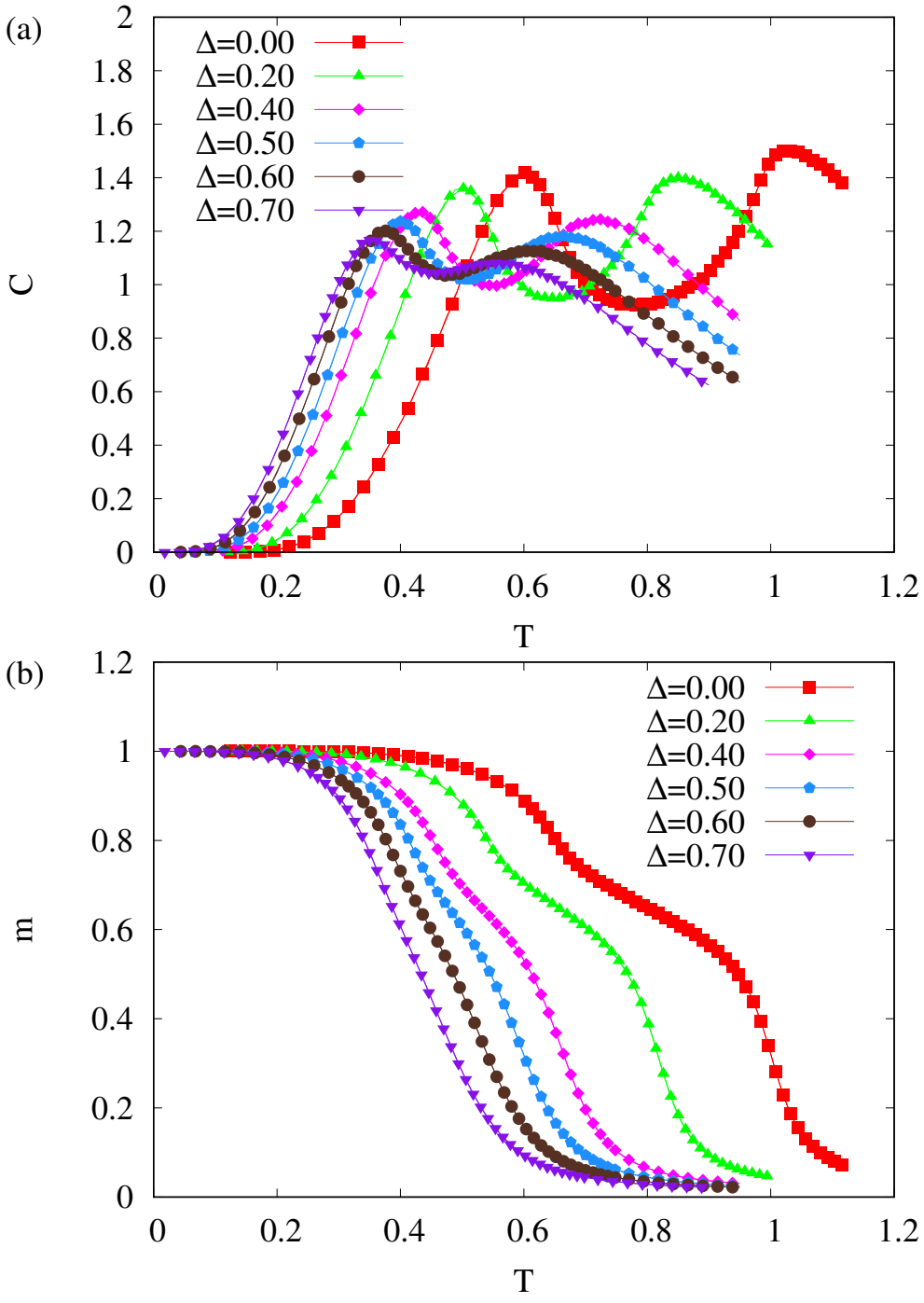

Figure 7. Specific heat C (a) and magnetization m (b) vs. temperature T for different disorder strengths Δ and linear system size $L = L_\tau = 128$. The temperature region between the two peaks gets narrower as the disorder increases, and the shoulder in $m(T)$ vanishes.

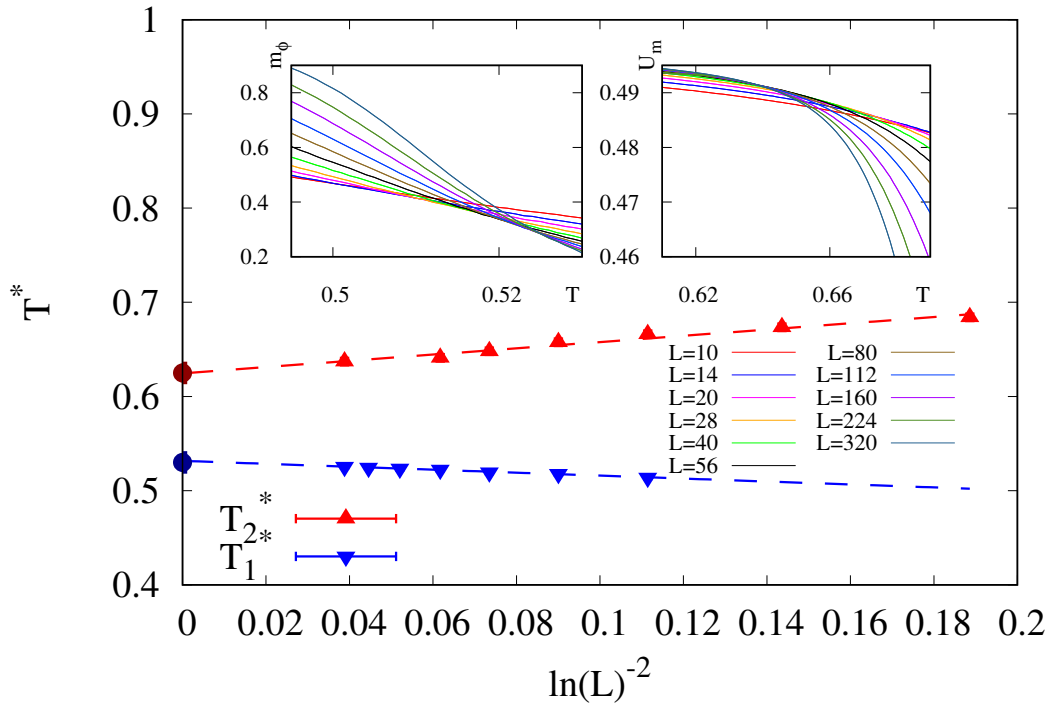

Figure 8. Extrapolation of crossing temperatures $T^*(L)$ of m_ϕ (bottom, blue) and U_m (top, red) for different system sizes and disorder strength $\Delta = 0.3$. The transition temperatures are obtained as the y-intercepts from fits using $T^*(L) = T_c + A(\ln L)^{-2}$. These yield $T_{c1} = 0.530(5)$ and $T_{c2} = 0.625(10)$. The insets show m_ϕ (left) and U_m (right) close to the respective transitions.

Luttinger parameter or, equivalently, the geometric mean $\sqrt{\rho_s \rho_\tau}$. A representative example for the same disorder strength $\Delta = 0.3$ is shown in Fig. 9. We find $T_{c1} = 0.53(1)$ and $T_{c2} = 0.63(1)$ for $\Delta = 0.3$ from the extrapolations using Eq. (23). These values agree with those obtained from the clock order parameter m_ϕ and the Binder cumulant U_m within their error bars.

The full phase diagram is obtained by repeating these procedures for various disorder strengths. For weak disorder up to $\Delta = 0.5$, we use square samples $L = L_\tau$. In the context of finite-size scaling, this assumes a dynamical exponent of $z = 1$ which will be confirmed in Sec. 4.3. For stronger disorder, we perform the full anisotropic scaling analysis discussed in Sec. 3.3 to determine the optimal shapes and the corresponding dynamical or tunneling exponent (see also Sec. 4.4). The phase diagram resulting from this analysis is shown in

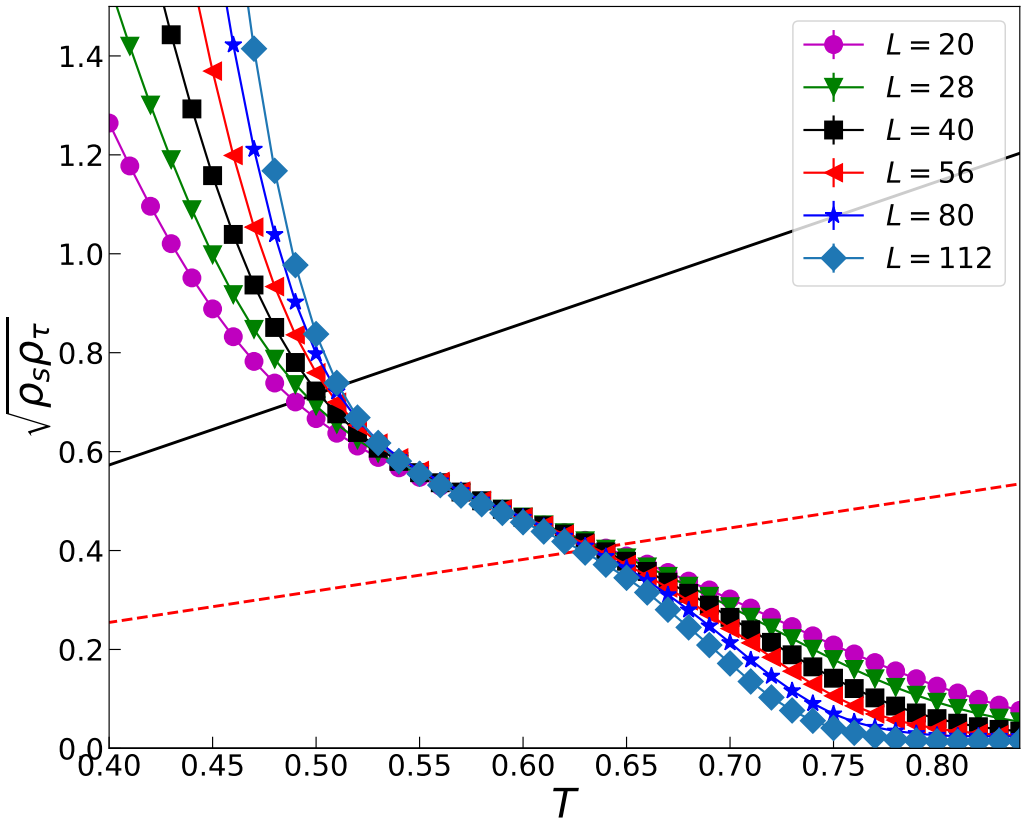

Figure 9. Helicity modulus combination $\sqrt{\rho_s \rho_\tau}$ vs. temperature T for different system sizes L at disorder strength $\Delta = 0.3$. Both ρ_s and ρ_τ have been corrected according to Eq. (14). The solid (black) line shows the Jose-Kadanoff relation $\sqrt{\rho_s \rho_\tau} = Tq^2/8\pi$, and the dashed (red) line depicts the Kosterlitz-Nelson relation $\sqrt{\rho_s \rho_\tau} = 2T/\pi$. T_{c1} and T_{c2} are determined by extrapolating the intersections of these lines with the data according to Eq. (23), resulting in $T_{c1} = 0.53(1)$ and $T_{c2} = 0.63(1)$.

Fig. 10. In line with our expectations gleaned from the study of the specific heat C and the magnetization m, we see that the intermediate QLRO phase shrinks with increasing disorder strength Δ. This means, the phase transitions at T_{c1} and T_{c2} come closer to each other as the Δ increases and finally merge at a multicritical point [11]. We estimate the multicritical point

[11] Thermodynamic considerations can restrict the possible topologies of phased diagrams with multicritical points [170]. In the case of the disordered clock model, the weak, essential singularity of the free energy at the BKT transitions at T_{c1} and T_{c2} makes the multicritical point thermodynamically possible.

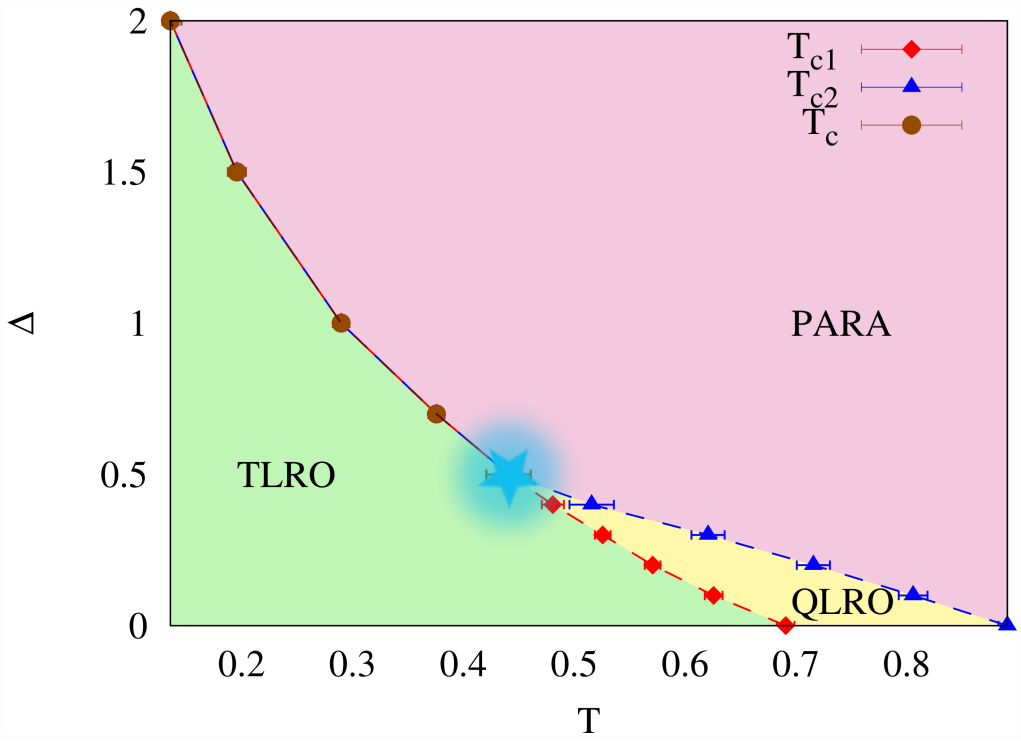

Figure 10. Phase diagram of the disordered 6-state clock model (2). The transition between the TLRO and QLRO phases occurs at T_{c1} (red squares), the transition between the QLRO and paramagnetic phase occurs at T_{c2} (blue triangles), and the direct transition between the TLRO and paramagnetic phases is denoted by T_c (brown circles). The multicritical point is located somewhere in the shaded region, near $\Delta = 0.5$, where T_{c1} and T_{c2} merge. The lines are guides to the eye only.

to be located at $\Delta \approx 0.5$; a more accurate determination is hampered by strong finite-size effects due to the crossovers between the different critical behaviors. Qualitatively, the phase diagram matches with the expectation sketched in Fig. 2.

4.3. CRITICAL BEHAVIOR IN THE WEAK-DISORDER REGIME

The correlation length exponent ν of a BKT transition is formally infinite and thus fulfills the Harris criterion $d\nu > 2$ [93]. Correspondingly, the specific heat exponent α, obtained from the scaling relation $2-\alpha = d\nu$ is formally $-\infty$, in agreement with the missing specific heat divergence discussed after Fig. 7. The Harris criterion thus implies that the

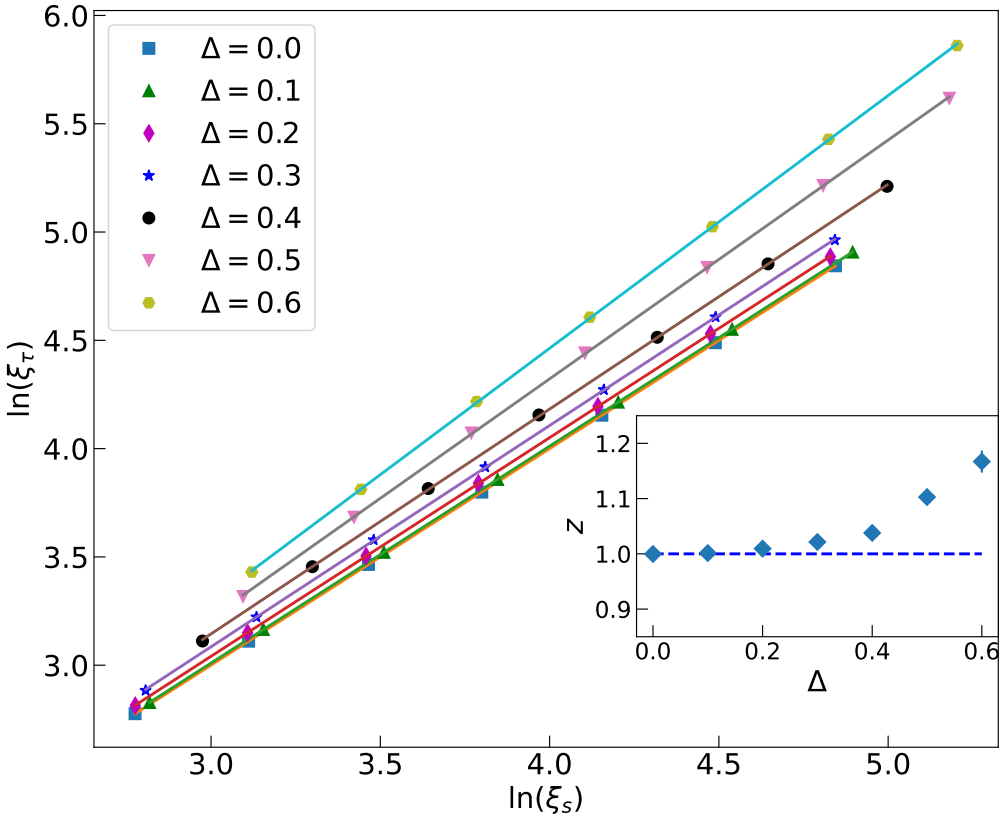

Figure 11. Correlation length ξ_s in space direction vs. correlation length ξ_τ in imaginary-time direction near T_{c2} for several disorder strengths Δ. The solid lines are fits to $\xi_\tau = A\xi_s^z$. Inset: Estimate of dynamical exponent z as a function of Δ. The dashed line denotes the clean critical value $z = 1$

critical behaviors of both transitions are expected to agree with the corresponding clean critical behaviors for sufficiently weak disorder. However, the Harris criterion does not forbid a change of critical behavior for stronger disorder.

We start by analyzing the dynamical scaling at the transition between the QLRO and paramagnetic phases. To this end, we study the relation between the spatial correlation length ξ_s and the imaginary time correlation length ξ_τ. Figure 11 presents ξ_τ as a function of ξ_s for various disorder strengths at T_{c2}. The data follow the power-law form $\xi_\tau \sim \xi_s^z$ expected for conventional dynamical scaling. The estimates of the dynamical exponent z that results from fits to this functional form are shown in the inset of the figure. For all

disorder strengths below the putative multicritical disorder $\Delta \approx 0.5$, the z values remain at or very close to the clean value $z = 1$. We believe that the small deviations can be attributed to finite-size effects in combination with the crossover induced by the multicritical point [12]. The fact that the dynamical exponent remains at $z = 1$ at the transition between the QLRO and paramagnetic phases agrees with the analogous result for the disordered $(1+1)$-dimensional quantum rotor model [152]. The fitted values of z for $\Delta \gtrapprox 0.5$ need to be understood as effective exponents as the behavior for these disorder strengths is strongly affected by the multi-critical point and the crossover between the weak and strong disorder regimes.

To investigate the dynamical scaling at the transition between the TLRO and QLRO phases, we perform the anisotropic finite-size scaling analysis of the clock order parameter m_ϕ, as discussed in Sec. 3.3. This means we compute m_ϕ as a function of L_τ for fixed L right at the critical temperature T_{c1}. A prototypical scaling plot of $m_\phi/m_\phi^{\max}$ vs. $L_\tau/L_\tau^{\max}$ for disorder strength $\Delta = 0.4$ is presented in Fig. 12. The data for other disorder strengths below the multicritical point are expected to behave analogously. As is evident from the figure, the scaling collapse in accordance with the conventional scaling ansatz (16) is very good, whereas the data do not collapse when analyzed according to the activated scaling ansatz (20), as shown in the top inset. This demonstrates that the dynamical scaling is of a power-law type. An estimate of the the dynamical exponent z can be extracted from fitting the $L_\tau^{\max}$ vs. L data shown in the bottom inset in Fig. 12 with $L_\tau^{\max} = aL^z$. This again yields a value very close to $z = 1$. As above, we believe that the small deviation from unity is caused by finite-size effects. We thus conclude that the dynamical scaling at both

[12] The finite size effects stem, at least partially, from the fact that ξ_s and ξ_τ are finite-size correlation lengths. Extrapolating them to infinite system size should mitigate the finite-size effects. We have attempted to estimate the bulk correlation lengths, $\xi_s^\infty, \xi_\tau^\infty$, following the protocol described in Ref. [171]. Unfortunately, the accumulation of errors during this procedure demands very high accuracy input data beyond our numerical capabilities.

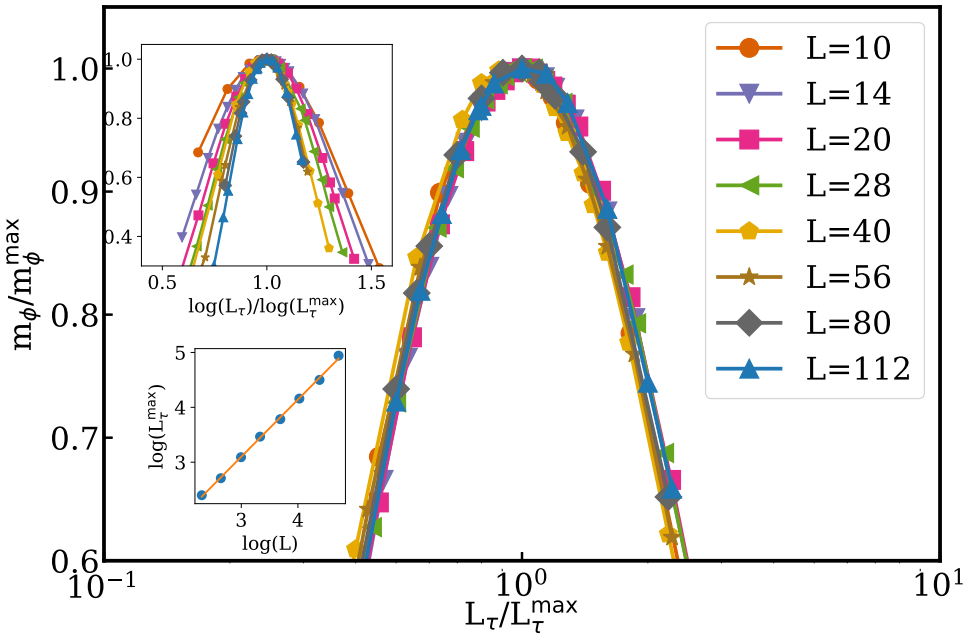

Figure 12. Anisotropic finite-size scaling of the clock order parameter m_ϕ near $T_{c1} \approx 0.485$ at $\Delta = 0.4$ using the power-law (conventional) scaling ansatz. Top inset: Same data analyzed using the activated scaling ansatz. Bottom inset: $\log(L)$ vs $\log(L_\tau^{\max})$, the straight line represents a fit with $L_\tau^{\max} = AL^z$. It yields $z = 1.04(2)$.

transitions below the multicritical disorder strength is of conventional power law type, and the (asymptotic) dynamical exponent retains the value $z = 1$, justifying the use of square samples in the rest of the simulations in the weak-disorder regime.

We now turn to measuring the anomalous exponent η. Figures 13(a) and 13(b) show the dependence of the magnetization m on the system size at T_{c1} and T_{c2}, respectively, for a range of disorder strengths. The data at both transitions agree very well with the expected power-law form (22). Using $d = z = 1$, Eq. (22) turns into the relation $m \sim L^{-\eta/2}$. The anomalous exponents η are extracted from fits of the data with this functional form, and their values are shown in the inset of Fig. 13(a) as functions of the disorder strength Δ. The behavior of η at the QLRO-to-paramagnetic transition is interesting. As the disorder strength Δ is increased from zero, η initially remains at its clean value (which is somewhat below the theoretical expectation of 1/4, likely due to finite-size effects). For $\Delta \gtrsim 0.3$,

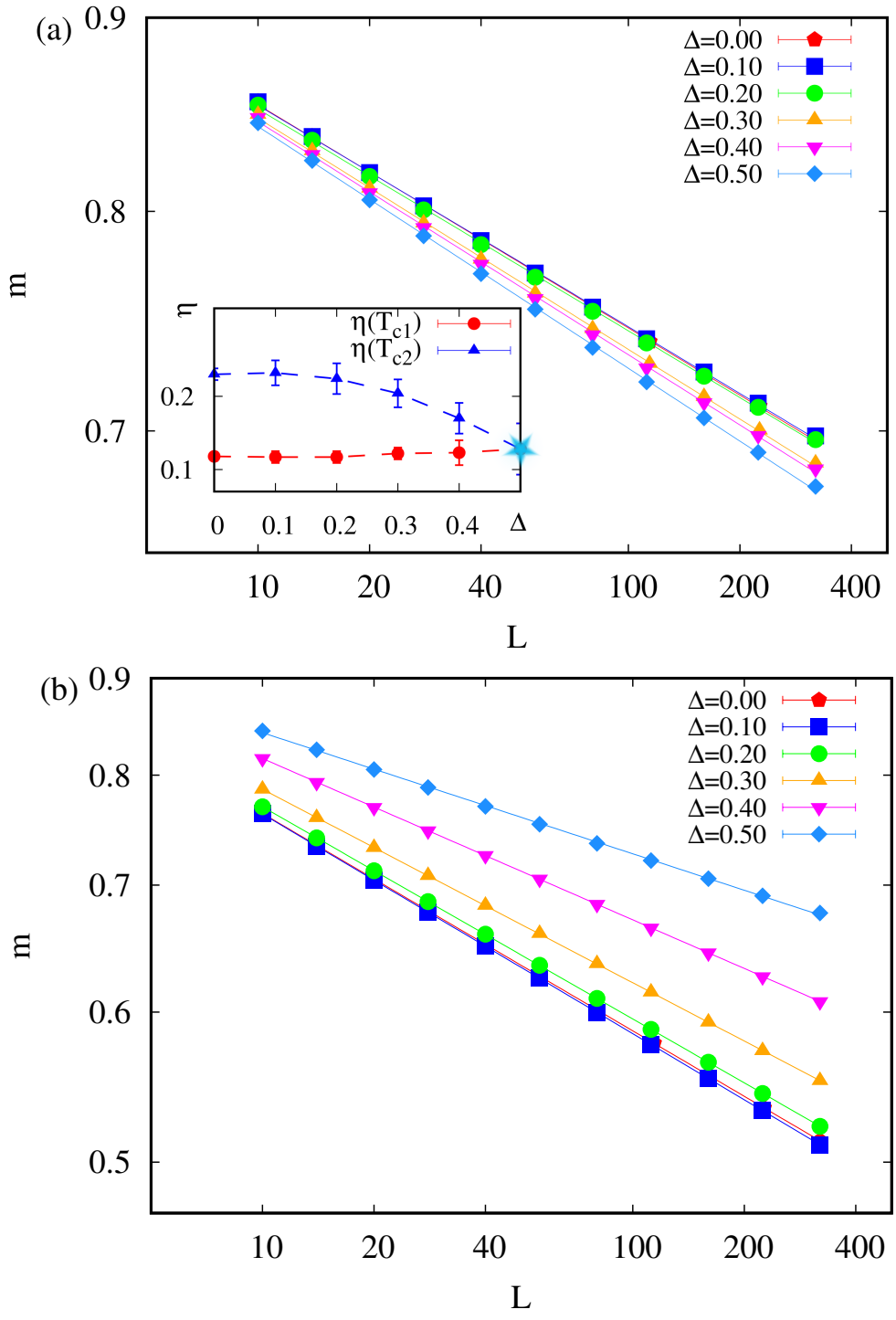

Figure 13. Magnetization m vs. system size L at (a) T_{c1} and (b) T_{c2}. The solid lines are fits to the relation $m \sim L^{-\eta/2}$. Inset: Exponents $\eta(T_{c1})$ and $\eta(T_{c2})$ vs. disorder strength Δ. The shaded region close to $\Delta = 0.5$ marks the location of the multicritical point. The lines are guides to the eye only.

in contrast, η decreases significantly and displays a prominent disorder dependence. This decrease in η is reminiscent of the behavior observed in a disordered $(1 + 1)$-dimensional XY model [152]. Our numerical accuracy is not sufficient to determine whether the change of η with Δ is a smooth crossover or a sharp transition somewhere around $\Delta = 0.3$.

The anomalous exponent at the TLRO-to-QLRO transition at T_{c1} also remains at its clean value for the weak disorder. For $\Delta \gtrapprox 0.3$, it rises slightly, but the increase is minuscule, smaller than the error bars. With the current numerical accuracy, we therefore cannot determine with certainty whether this exponent becomes disorder-dependent before the multicritical point is reached.

Finally, we confirm the BKT character of the paramagnetic-to-QLRO phase transition at T_{c2} by studying the dependence of the correlation length ξ_s on the distance from the transition point. Close to a BKT transition, ξ_s is expected to follow the functional form

$$\xi_s = A e^{B(T-T_{c2})^{-1/2}} \ . \tag{24}$$

Here, A and B are non-universal constants. In Fig. 14, we plot the correlation length ξ_s as a function of temperature in the paramagnetic phase for various system sizes at $\Delta = 0.3$. The figure shows that ξ_s follows the predicted exponential form until finite-size effects take over close to the transition point.

4.4. CRITICAL BEHAVIOR IN THE STRONG-DISORDER REGIME

We now turn our attention to the strong-disorder regime, i.e., disorder strengths above the multicritical value $\Delta \approx 0.5$, where the system features a direct transition between the TLRO and paramagnetic phases. To explore this region, we have performed simulations for several disorder strengths, viz., $\Delta = 0.7, 1.0, 1.5$ and 2.0. Based on the SDRG of Senthil and Majumdar [153], the critical behavior at sufficiently large Δ is expected to be of the infinite-randomness type with activated rather than conventional power-law dynamical

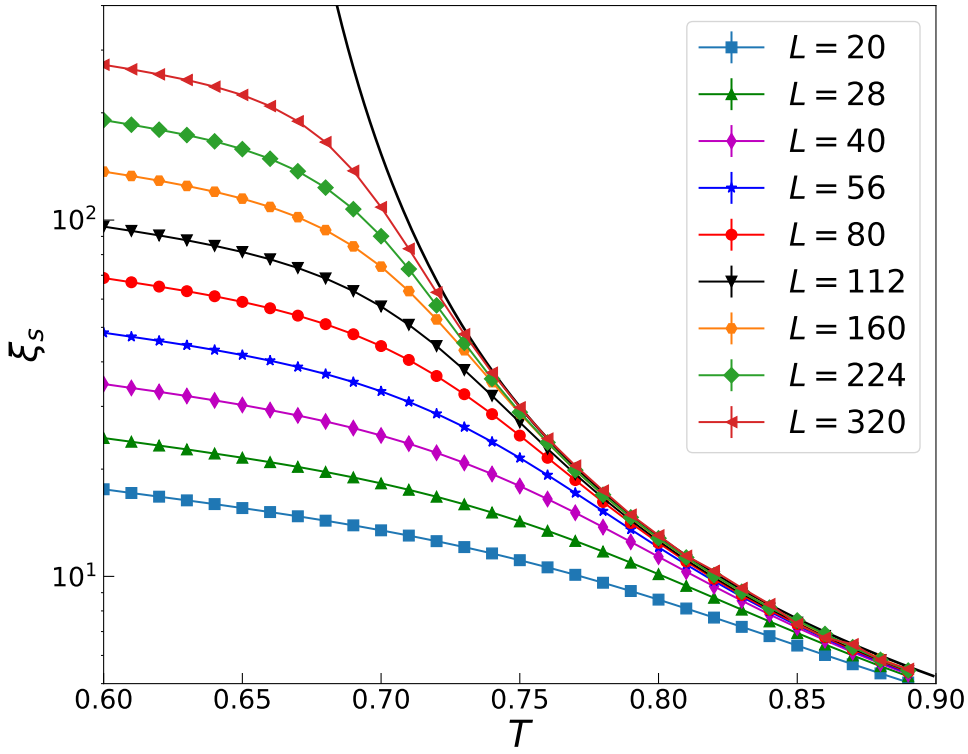

Figure 14. Spatial correlation length ξ_s vs. temperature T in the paramagnetic phase for $\Delta = 0.3$. The solid line is a fit of the data for the largest system size with the BKT form (24) in the temperature range from 0.73 to 0.9. The value of T_{c2} is fixed at 0.625, as found via the Binder cumulant crossings in Fig. 8.

scaling. To test this prediction, we perform the anisotropic FSS analysis discussed in Sec. 3.3. The results are shown in Fig. 15 for the prototypical case of $\Delta = 1.5$. To find the critical temperature T_c, we use the fact that the m_ϕ vs. L_τ curve (at fixed L and T) develops a maximum at $L_\tau^{\max}$ which marks the "optimal shape" that keeps the second argument of the scaling functions in Eqs. (15) to (20) constant. The value of m_ϕ at the maximum is independent of the system size L right at criticality [169, 172], as is the case in Fig. 15(b). In contrast, this maximum value increases with L for $T < T_c$ as illustrated in Fig. 15(a), whereas it decreases with L for $T > T_c$, see Fig. 15(c). Following this methodology, we estimate the transition temperatures to be 0.380(6), 0.294(6), 0.200(8), and 0.140(10) for $\Delta = 0.7$, 1.0, 1.5 and 2.0, respectively.

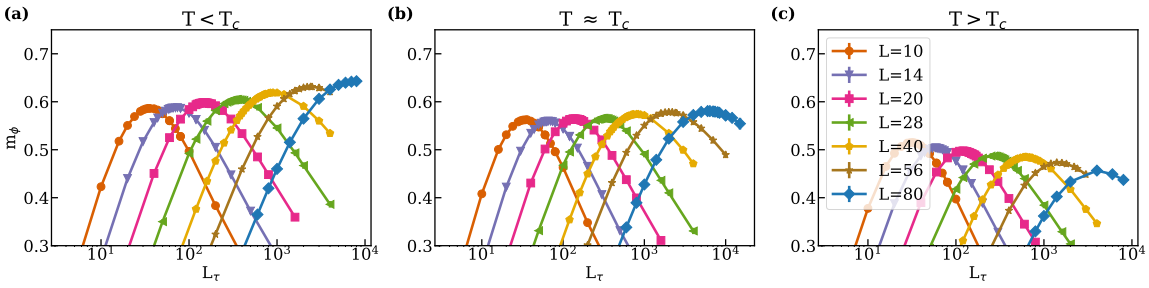

Figure 15. Clock order parameter m_ϕ as a function of the imaginary-time system size L_τ for different spatial system sizes L and disorder strength $\Delta = 1.5$. The temperatures are (a) $T = 0.196 < T_c$, (b) $T = 0.200 \approx T_c$ and (c) $T = 0.208 > T_c$. The peak values of m_ϕ are independent of L at T_c whereas they decrease with L for $T > T_c$ and increase with L for $T < T_c$. The statistical errors are of the order of the symbol size or smaller.

To distinguish conventional power-law dynamical scaling from activated dynamical scaling, we investigate the scaling collapse of the m_ϕ vs. L_τ curves for $\Delta = 1.5$ in Fig. 16. The figure clearly shows that the data collapses very well when plotted according to the activated scaling ansatz (20). Small deviations from perfect collapse for the smallest system sizes can be attributed to corrections to scaling stemming from the crossover towards infinite-randomness criticality. In contrast, the data do not collapse when plotted according to the conventional power-law scaling ansatz (16) but rather broaden with increasing system size. We therefore conclude that the critical behavior is of infinite-randomness type. We have repeated this analysis for $\Delta = 1.0$, and 2.0, with analogous results. The data collapse using the activated scaling scenario gets increasingly better, and extends to smaller system sizes as the disorder strength increases. This implies the presence of a cross-over length scale which decreases with increasing disorder strength.

To compare the critical behavior quantitatively with the predictions of Senthil and Majumdar [153], we analyze the dependence of $L_\tau^{\max}$ on L in Fig. 17. The figure shows that the data follow the predicted activated scaling relation $\log(L_\tau^{max}) \sim L^\psi$ with $\psi = 1/2$ for all disorder strengths we studied in the strong-disorder regime, provided the system size is larger than a disorder-dependent crossover length scale. Specifically, the data for the strongest disorders, $\Delta = 2.0$ and 1.5, follow the infinite-randomness prediction for all

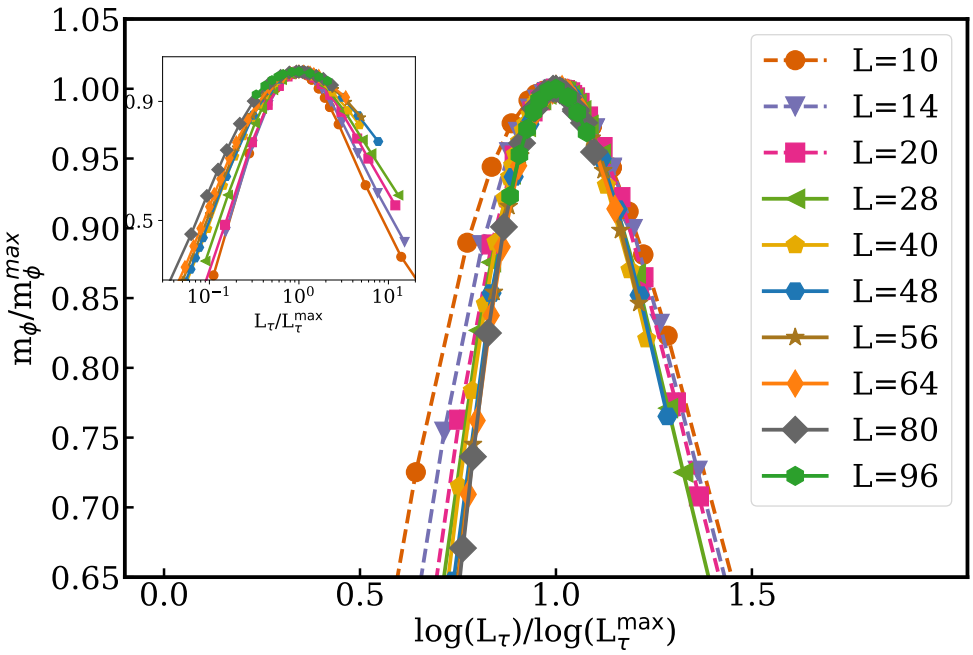

Figure 16. Scaling plot of $m_\phi/m_\phi^{\max}$ vs. $\log(L_\tau)/\log(L_\tau^{\max})$ at the critical temperature for $\Delta = 1.5$ according to the activated scaling ansatz (20). The dashed lines represent the data of the smallest system sizes which do not collapse perfectly due to the corrections to scaling. Inset: Same data plotted according to the power-law scaling ansatz (16). The data do not collapse onto each other but broaden with increasing system size.

$L \geq 20$. The $\Delta = 1$ data follow the prediction for $L \geq 56$, whereas the data for the weakest disorder, $\Delta = 0.7$, only follow the prediction if $L \geq 80$. This shows that the cross-over length scale increases with decreasing disorder (as the multicritical point is approached).

Finally, we analyze the system-size dependence of the average magnetization at criticality (using the optimal shapes, i.e., $L_\tau = L_\tau^{\max}$). Figure 18 shows that the data for disorder strengths $\Delta \geq 1.0$ follow the SDRG prediction $m \sim L^{-\beta/\nu}$ with critical exponent $\beta/\nu = 0.19$ for system sizes above a crossover scale that increases rapidly with decreasing disorder. The data for the weakest disorder we study in this regime, $\Delta = 0.7$, show the beginning of a crossover (manifest in the small downward curvature of the curve with increasing L), but the crossover length appears to be larger than the maximum system size

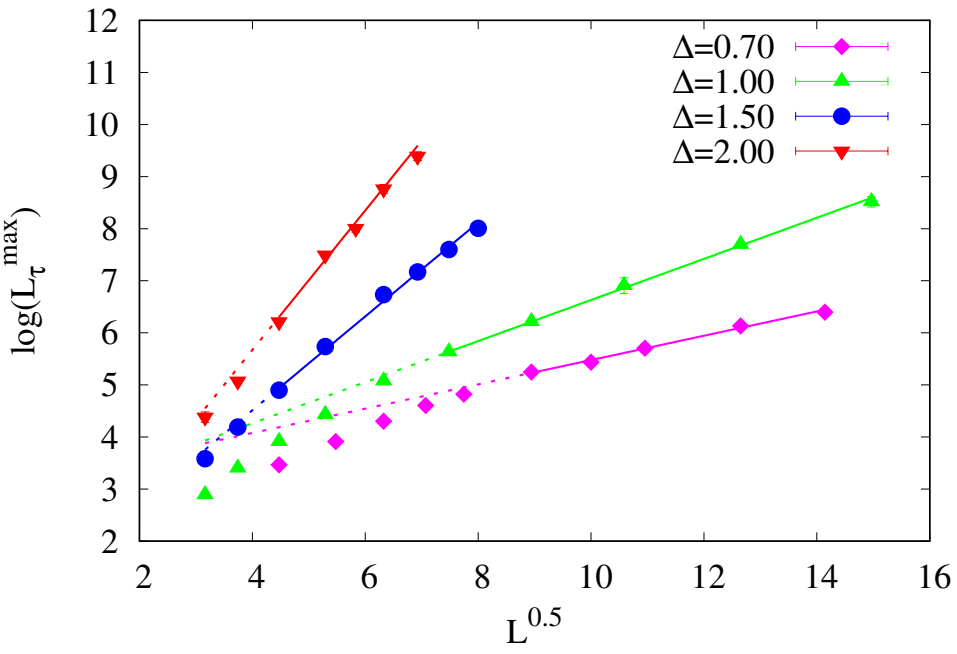

Figure 17. $\log(L_\tau^{\max})$ vs. $L^{0.5}$ at criticality for several disorder strengths in the strong-disorder regime. The solid lines are fits with the activated scaling relation $\log(L_\tau^{\max}) = a + bL^\psi$. Here ψ is fixed at the theoretical value of 0.5, and a and b are fit parameters. The dotted lines mark smaller system sizes that are not included in the fits.

in our simulations. This implies that a power-law fit of the data for $\Delta = 0.7$ would only yield an effective (L-dependent) exponent value rather than the true asymptotic exponent (analogous to a fit of the $\Delta = 1.00$ data for $L < 96$).

We thus conclude that the magnetization data for $\Delta = 0.7$ are compatible with the infinite-randomness scenario predicted by the SDRG, but we cannot exclude a different asymptotic behavior.

Within the infinite-randomness scenario, the critical point is expected to be accompanied by quantum Griffiths phases [95, 96, 97, 98, 99, 100] that feature non-universal power-law singularities of observables not just at criticality but in an entire region around the transition. In order to identify quantum Griffiths behavior in our simulations, we follow the method employed in Ref. [91] and study the susceptibility χ as a function of L_τ for large fixed L close to (but not exactly at) the transition. For the original quantum Hamiltonian

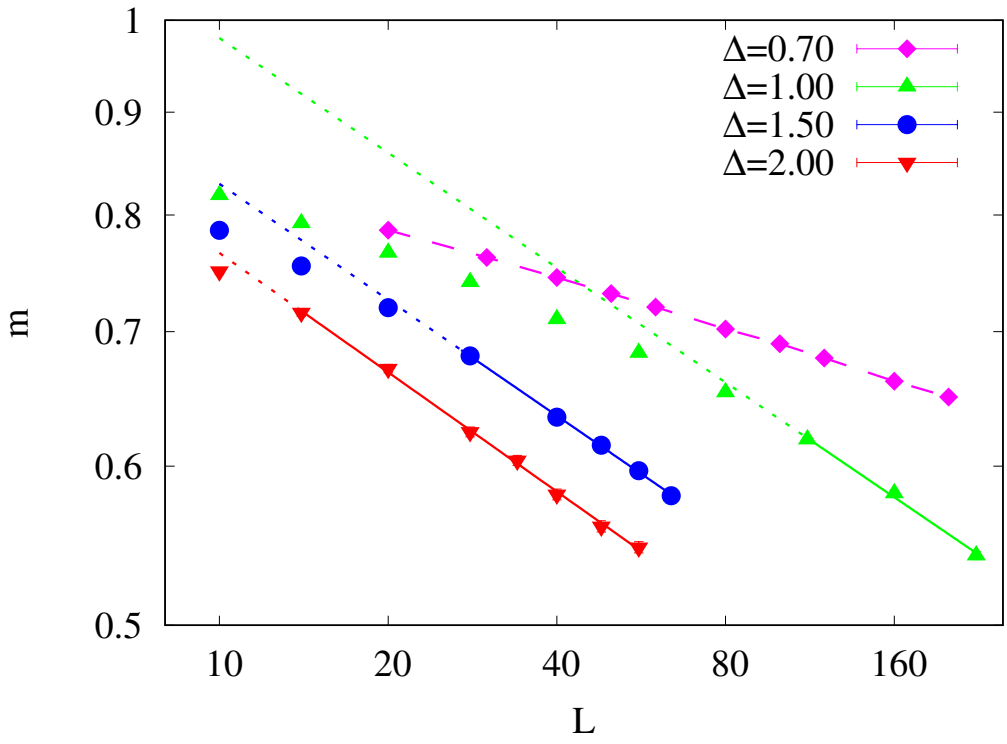

Figure 18. Average magnetization m at criticality vs. system size L for several disorder strengths Δ in the strong disorder regime. Solid lines are fits with $m = aL^{-\frac{\beta}{\nu}}$ with β/ν and a fit parameters. The fits yield $\beta/\nu = 0.19(1)$ for disorder strengths $\Delta \geq 1.0$. The dotted lines mark smaller system sizes that are not included in the fits. The data for $\Delta = 0.7$ (dashed line) do not appear to reach the asymptotic behavior for the available system sizes. Thus, we do not show a power-law fit of these data .

(1), this corresponds to studying the temperature dependence of χ slightly off criticality. Specifically, we compute χ for disorder strength $\Delta = 2.0$, spatial system size $L = 800$, and temporal sizes $L_\tau = 10$ to 80 in the temperature region from $T = 0.125$ to 0.25. For a range of temperatures close to $T_c = 0.14$ (as found from the scaling analysis of m_ϕ above), the susceptibility follows the expected non-universal power law $\chi \sim L_\tau^{1\pm 1/z'}$ where z' is the Griffiths dynamical exponent. Within the infinite-randomness scenario, z' is expected

to diverge at T_c, leading to a linear relation between χ and L_τ. Our simulation data do not quite agree with this, they give $\chi \sim L_\tau^{1.2}$ at $T = 0.14$. We attribute this deviation to finite-size effects due to the relatively small L_τ values from 10 to 80 [13].

It is interesting to compare our strong evidence for a Griffiths phase in the form of non-universal power-law behavior of the susceptibility with the results of Ref. [173] for the $(2 + 1)$ dimensional disordered clock model. In Ref. [173], the evidence for the very existence of the Griffiths phase is inconclusive because the data do not consistently show non-universal power-law behavior. This may stem from the fact that the strengths of Griffiths singularities decreases with increasing dimensionality [98, 174] implying that stronger disorder and/or larger sizes may be necessary to see the Griffiths phase in $(2 + 1)$ dimensions.

5. CONCLUSION AND SUMMARY

In this manuscript, we have investigated the impact of quenched random disorder on the phases and phase transitions of the one-dimensional quantum q-state clock model, focusing on $q = 6$ which serves as a test bed for all $q > 4$ cases. To this end, we have performed large-scale Monte Carlo simulations of a classical clock model with a perfectly correlated (columnar) disorder that arises from the quantum-to-classical mapping of the quantum model's partition function. Our results have established that the disorder is inimical to the emergent QLRO phase that separates the TLRO phase from the paramagnetic phase in the clean system. Specifically, the intermediate QLRO phase shrinks with increasing disorder strength, finally resulting in a multicritical point beyond which there is a direct phase transition from the clock-ordered (TLRO) phase to the paramagnetic phase.

[13] In the Griffiths phase, the susceptibility contains a regular bulk contribution and the singular rare region contribution that produces the Griffiths singularities. For small L_τ, corrections to the Griffiths physics stemming from the regular part are still sizable.

The bulk of our results were obtained using the power-law disorder distribution (3). This distribution becomes arbitrarily broad (even on a logarithmic scale) for $\Delta \to \infty$, We have tested the influence of the disorder distribution by performing simulations with a binary distribution as implemented in Ref. [152]. In agreement with the expected universality of the phase diagram, these simulations show the same shrinking of the QLRO phase with increasing disorder strengths. However, the crossover to the strong disorder regime is slower, and the asymptotic behavior is not reached for the numerically accessible system sizes. We expect analogous behavior for other "less broad" distributions such as the box distribution.

We have also characterized the critical behavior along the different phase boundaries in the disorder-(classical) temperature phase diagram. In agreement with the Harris criterion [93], the critical behaviors of the BKT transitions from the TLRO phase to the QLRO phase as well as from the QLRO phase to the paramagnetic phase are stable against weak disorder. As the disorder strength is increased, both transitions retain the BKT character with a dynamical exponent $z = 1$ all the way to the multicritical point (or, at least, close to it). However, the anomalous exponent η of the QLRO-to-paramagnet transition deviates from its clean value and becomes disorder dependent, analogous to the behavior observed in a disordered (1+1)-dimensional XY model [152]. For the TLRO-to-QLRO transition, in contrast, the changes of η, if any, are small and within the error bars of our simulations.

For disorder strengths well above the multi-critical point, our results have demonstrated that the critical behavior of the direct transition between the TLRO and paramagnetic phases is of exotic infinite-randomness type and falls into the random transverse-field Ising universality class, as predicted by the SDRG analysis of Ref. [153]. Our results have also provided numerical evidence for a quantum Griffiths phase associated with the infinite-randomness critical point.

The critical behavior of the multi-critical point itself is difficult to determine numerically because the crossovers between the three different critical behaviors on the adjacent phase boundaries lead to a strong and complex finite-size correction. Resolving these with a Monte Carlo approach would require significantly larger system sizes than we were able to access in our simulations. The same also applies to the interesting question of whether the infinite-randomness critical behavior takes over right after the disorder strength is increased beyond its multicritical value. While our numerical data show no indication of an intermediate regime between the multicritical point and infinite-randomness criticality at the largest disorders, a complete analysis of the vicinity of the multicritical point remains a task for the future.

Interesting questions arise for higher-dimensional quantum clock models and their classical counterparts. The two-dimensional q-state quantum clock model and its three-dimensional classical counterpart do not have an intermediate phase but a direct transition from the clock-ordered phase to the paramagnetic phase. For $q \geq 4$, the critical point has an emerging XY symmetry. However, this symmetry is broken down to a discrete Z_q symmetry in the ordered phase by means of a dangerously irrelevant variable [135, 175, 176]. What happens to this scenario in the presence of quenched disorder? A recent study employing a numerical SDRG calculation concluded that the critical behavior is of the IRFP type [173]. As discussed in Sec. 4.4, the evidence for quantum Griffith behavior in the vicinity of the transition was inconclusive. An investigation along the lines of our study may help address this problem and potentially unravel surprising disorder-induced cross-over effects.

APPENDIX: QUANTUM TO CLASSICAL MAPPING

In this section, we discuss the quantum-to-classical mapping that relates the partition function of a d-dimensional quantum system to that of a classical system in $D = d + 1$ dimensions. It is based on expressing the quantum partition function as a path integral in $(d + 1)$-dimensional Euclidean space-time. This is formally always possible, e.g., via a

Trotter decomposition of the partition function. However, the question of whether or not the action of this path integral can be interpreted as a classical Hamiltonian in $(d+1)$ space dimensions depends on the problem at hand. In some cases (including ours), the action is real and leads to positive statistical weights. It can thus be understood as a classical Hamiltonian. In other cases, such as the bosonic Hubbard model at non-integer filling, the action leads to negative or complex weights and cannot be interpreted as the Hamiltonian of a classical system [8, 177].

We now derive the mapping from the one-dimensional quantum clock Hamiltonian (1) to the equivalent two-dimensional classical clock model (2). For simplicity, let us consider the translational invariant case with $J_l = J$ and $h_l = h$. We rewrite the Hamiltonian (1) in terms of generalized Pauli matrices as follows,

$$\begin{aligned} H &= -\frac{J}{2}\sum_{i}^{N}\left[\hat{\tau}_i\hat{\tau}_{i+1}^{\dagger} + \hat{\tau}_i^{\dagger}\hat{\tau}_{i+1}\right] - \frac{h}{2}\sum_{i}^{N}\left[\hat{\Gamma}_i + \hat{\Gamma}_i^{\dagger}\right] \\ &= H_0 + H_1 \ . \end{aligned} \tag{25}$$

The matrix forms of the clock operators $\hat{\tau}$ and the shift operators $\hat{\Gamma}$ in the clock state basis $|p\rangle$ with $p = 0, \ldots, q-1$ are given by

$$\hat{\tau} = \begin{pmatrix} 1 & 0 & 0 & \cdots & 0 \\ 0 & \omega & 0 & \cdots & 0 \\ 0 & 0 & \omega^2 & \cdots & 0 \\ \vdots & \vdots & \vdots & \ddots & \vdots \\ 0 & 0 & 0 & \cdots & \omega^{(q-1)} \end{pmatrix} \tag{26}$$

and

$$\hat{\Gamma} = \begin{pmatrix} 0 & 1 & 0 & \cdots & 0 \\ 0 & 0 & 1 & \cdots & 0 \\ 0 & 0 & \ddots & 1 & 0 \\ \vdots & \vdots & \vdots & \ddots & \vdots \\ 1 & 0 & 0 & \cdots & 0 \end{pmatrix}, \tag{27}$$

where $\omega = e^{2\pi i/q}$. In other words,

$$\hat{\tau}\,|p\rangle = \omega^p\,|p\rangle\ , \tag{28}$$

$$\hat{\Gamma}\,|p\rangle = |(p-1) \mod q\rangle\ . \tag{29}$$

The clock and shift operators at a given lattice site satisfy the relations

$$\hat{\tau}^q = I = \hat{\Gamma}^q \quad \text{and} \quad \hat{\tau}\hat{\Gamma} = \omega\hat{\Gamma}\hat{\tau}\ . \tag{30}$$

The clock and shift operators commute at different sites.

Consider the partition function of the Hamiltonian (1) at a (quantum) temperature $T = 1/\beta$ [14],

$$Z = \mathrm{Tr}\left(e^{-\beta H}\right)\ . \tag{31}$$

The operator $e^{-\beta H}$ can be regarded as the imaginary time evolution operator from imaginary time 0 to β. Using the standard Trotter decomposition technique, we can decompose Z as

$$Z = \mathrm{Tr}(\underbrace{e^{-\Delta\tau H}e^{-\Delta\tau H}\ldots e^{-\Delta\tau H}}_{L_\tau \text{ times}}) \quad \left(\text{where } \Delta\tau = \frac{\beta}{L_\tau}\right)\ . \tag{32}$$

[14] In this appendix, the inverse physical temperature of the quantum Hamiltonian (1) is denoted by β while that of the mapped classical system (2) is called β_{cl}.

Here, L_τ is the number of time slices. Now, we use the completeness condition

$$I = \sum_{\{p=0,1,\ldots q-1\}} |p\rangle \langle p| \tag{33}$$

with $|p\rangle = |p_1\rangle \bigotimes |p_2\rangle \bigotimes \ldots |p_N\rangle$. Imposing periodic boundary conditions in the imaginary time direction $|p^0\rangle = |p^{L_\tau}\rangle$, the partition function can be expressed as

$$\begin{aligned} Z = \sum_{\{p^\tau\}} & \left\langle p^0 \left| e^{-\Delta\tau H} \right| p^{L_\tau - 1} \right\rangle \left\langle p^{L_\tau - 1} \left| e^{-\Delta\tau H} \right| p^{L_\tau - 2} \right\rangle \\ & \cdots \left\langle p^{\tau+1} \left| e^{-\Delta\tau H} \right| p^{\tau} \right\rangle \cdots \left\langle p^{1} \left| e^{-\Delta\tau H} \right| p^{0} \right\rangle \end{aligned} , \tag{34}$$

where we have introduced, at each time step τ, a complete set of states $|p^\tau\rangle$. We assume that L_τ is large so that $\Delta\tau$ is small and further decompose

$$e^{-\Delta\tau H} = e^{-\Delta\tau(H_0+H_1)} \simeq e^{-\Delta\tau H_0} e^{-\Delta\tau H_1} . \tag{35}$$

Now, consider one such matrix element :

$$\left\langle p^{\tau+1} \left| e^{-\Delta\tau H} \right| p^{\tau} \right\rangle \simeq \left\langle p^{\tau+1} \left| e^{-\Delta\tau H_0} e^{-\Delta\tau H_1} \right| p^{\tau} \right\rangle . \tag{36}$$

We note that $|p\rangle$ is an eigenstate of $\hat{\tau}$ operator. Therefore

$$\begin{aligned} e^{\hat{\tau}_i \hat{\tau}_{i+1}^\dagger} |p_i p_{i+1}\rangle &= e^{\omega^{p_i} \omega^{-p_{i+1}}} |p_i p_{i+1}\rangle \quad \text{and} \\ e^{\hat{\tau}_i^\dagger \hat{\tau}_{i+1}} |p_i p_{i+1}\rangle &= e^{\omega^{-p_i} \omega^{p_{i+1}}} |p_i p_{i+1}\rangle . \end{aligned} \tag{37}$$

We have

$$\begin{aligned} \omega^{p_i} \omega^{-p_{i+1}} &= e^{\frac{2\pi i}{q}(p_i - p_{i+1})} \quad \text{and} \\ \omega^{-p_i} \omega^{p_{i+1}} &= e^{-\frac{2\pi i}{q}(p_i - p_{i+1})} . \end{aligned} \tag{38}$$

From the above expressions, we can write

$$e^{\frac{2\pi i}{q}(p_i - p_{i+1})} + e^{-\frac{2\pi i}{q}(p_i - p_{i+1})} = 2\cos\left[\frac{2\pi}{q}(p_i - p_{i+1})\right]. \tag{39}$$

Hence, the matrix element can be written as

$$\begin{aligned} &\left\langle p^{\tau+1}\left|e^{-\Delta\tau H_0}e^{-\Delta\tau H_1}\right|p^{\tau}\right\rangle \\ &= \left\langle p^{\tau+1}\left|e^{+J\Delta\tau\sum_i^N \cos\left[\frac{2\pi}{q}(p_i^{\tau+1} - p_{i+1}^{\tau+1})\right]}e^{-\Delta\tau H_1}\right|p^{\tau}\right\rangle . \end{aligned} \tag{40}$$

Now, we act the remaining operator on the eigenstates. Consider

$$\begin{aligned} &\left\langle p^{\tau+1}\left|e^{-\Delta\tau H_1}\right|p^{\tau}\right\rangle \\ &= \left\langle p^{\tau+1}\left|e^{+\frac{h}{2}\Delta\tau\sum_i(\Gamma_i + \Gamma_i^{\dagger})}\right|p^{\tau}\right\rangle . \end{aligned} \tag{41}$$

Let us assume $\theta = \frac{h}{2}\Delta\tau$. Then,

$$e^{\theta\Gamma} = \sum_n \frac{(\theta\Gamma)^n}{n!} . \tag{42}$$

Here, we split the expansion into q different series as follows

$$e^{\theta\Gamma} = \sum_p \frac{(\theta\Gamma)^{qp}}{(qp)!} + \sum_p \frac{(\theta\Gamma)^{qp+1}}{(qp+1)!} + ... + \sum_p \frac{(\theta\Gamma)^{qp+q-1}}{(qp+q-1)!} \tag{43}$$

Using the identity Γ^q=I, the expansion simplifies to

$$e^{\theta\Gamma} = \sum_p \frac{\theta^{qp}}{(qp)!} + \sum_p \frac{\theta^{qp+1}\Gamma}{(qp+1)!} + ... + \sum_p \frac{\theta^{qp+q-1}\Gamma^{q-1}}{(qp+q-1)!} \text{ ‘} \tag{44}$$

which we represent as

$$e^{\theta\Gamma} = f_0(\theta) + f_1(\theta)\Gamma + ... + f_{q-1}(\theta)\Gamma^{q-1} , \tag{45}$$

where we denote

$$f_{p-1}(\theta) = \Lambda e^{\gamma\omega^{p-1}} \ . \tag{46}$$

Now, let's evaluate the following elements,

$$\begin{aligned}
&\left\langle p^{\tau+1} \left| e^{\theta\Gamma} \right| p^{\tau} \right\rangle \\
&= \left\langle p^{\tau+1} \left| f_0(\theta) I + f_1(\theta)\Gamma + ... + f_{q-1}(\theta)\Gamma^{q-1} \right| p^{\tau} \right\rangle \\
&= \begin{cases} f_0(\theta) & \text{if } p^{\tau+1} = p^{\tau} \\ f_1(\theta) & \text{if } p^{\tau+1} = (p^{\tau}+1) \\ ... & \\ f_{q-1}(\theta) & \text{if } p^{\tau+1} = (p^{\tau}+q-1) \end{cases} \\
&= \begin{cases} \Lambda e^{\gamma\omega^0} & \text{if } p^{\tau+1} = p^{\tau} \\ \Lambda e^{\gamma\omega^1} & \text{if } p^{\tau+1} = (p^{\tau}+1) \\ ... & \\ \Lambda e^{\gamma\omega^{q-1}} & \text{if } p^{\tau+1} = (p^{\tau}+q-1) \end{cases} \\
&= \Lambda e^{\gamma\omega^{-(p^{\tau}-p^{\tau+1})}} \ .
\end{aligned} \tag{47}$$

Similarly,

$$\left\langle p^{\tau+1} \left| e^{\theta\Gamma^{\dagger}} \right| p^{\tau} \right\rangle = \Lambda e^{\gamma\omega^{(p^{\tau}-p^{\tau+1})}} \ . \tag{48}$$

Therefore,

$$\begin{aligned}
&\left\langle p^{\tau+1} \left| e^{\theta(\Gamma+\Gamma^{\dagger})} \right| p^{\tau} \right\rangle \\
&\qquad = \Lambda^2 e^{\gamma\omega^{(p^{\tau}-p^{\tau+1})}} e^{\gamma\omega^{-(p^{\tau}-p^{\tau+1})}} \\
&\qquad = \Lambda^2 e^{\gamma\left[e^{\frac{2\pi i}{q}(p^{\tau}-p^{\tau+1})} + e^{-\frac{2\pi i}{q}(p^{\tau}-p^{\tau+1})}\right]} \\
&\qquad = \Lambda^2 e^{2\gamma\left[\cos\frac{2\pi}{q}(p^{\tau}-p^{\tau+1})\right]} \ ,
\end{aligned} \tag{49}$$

which implies that,

$$\left\langle p^{\tau+1} \left| e^{\frac{h}{2}\Delta\tau \sum_i (\Gamma_i + \Gamma_i^\dagger)} \right| p^\tau \right\rangle = \Lambda^{2N} e^{2\gamma \sum_i^N \left[\cos \frac{2\pi}{q}(p_i^\tau - p_i^{\tau+1})\right]} . \tag{50}$$

The partition function can be rewritten to the following form

$$Z = \Lambda^{2NL_\tau} e^{\sum_i^N \sum_\tau^{L_\tau} [J\Delta\tau \cos[\frac{2\pi}{q}(p_i^\tau - p_{i+1}^\tau)] + 2\gamma \cos[\frac{2\pi}{q}(p_i^\tau - p_i^{\tau+1})]]} . \tag{51}$$

This is equivalent to the partition function of a two-dimensional classical clock model with the following Hamiltonian:

$$\begin{aligned} H_{\rm cl} = &- \sum_{i,\tau} J^s \cos\left[\frac{2\pi(p_{i,\tau} - p_{i+1,\tau})}{q}\right] \\ &- \sum_{i,\tau} J^t \cos\left[\frac{2\pi(p_{i,\tau} - p_{i,\tau+1})}{q}\right] . \end{aligned} \tag{52}$$

The couplings are connected via the relation

$$\beta_{\rm cl} J_s = J\Delta\tau, \quad \beta_{\rm cl} J_t = 2\gamma . \tag{53}$$

We have

$$\begin{aligned} e^{\frac{h}{2}\Delta\tau} &= \Lambda \left[\sum_{p=0}^{q-1} e^{\gamma\omega^p}\right] \quad \text{and} \\ e^{-\frac{h}{2}\Delta\tau} &= \Lambda \left[\sum_{p=0}^{q-1} (-1)^p e^{\gamma\omega^p}\right] . \end{aligned} \tag{54}$$

Therefore the relation between h and γ can be obtained as,

$$e^{-h\Delta\tau} = \frac{\sum_{p=0}^{q-1} (-1)^p e^{\gamma\omega^p}}{\sum_{p=0}^{q-1} e^{\gamma\omega^p}} . \tag{55}$$

For the case of the Ising model ($q = 2$), this reduces to

$$e^{-h\Delta\tau} = \frac{e^{\gamma} - e^{-\gamma}}{e^{\gamma} + e^{-\gamma}} = \tanh\gamma \ . \tag{56}$$

Note that temperature is not the tuning parameter of the quantum phase transition in the quantum Hamiltonian. However, changing the (inverse) classical temperature $\beta_{\rm cl}$ in the mapped classical model corresponds to changing h/J in the quantum Hamiltonian. Thus, universal properties of the quantum phase transitions in the quantum clock model can be obtained from the finite temperature transitions of the corresponding 2D classical clock model.

ACKNOWLEDGEMENTS

The simulations were performed on the Pegasus and Foundry clusters at Missouri S&T and the Aqua cluster at IIT Madras. We thank Ambuj Jain, Pranay Patil, Shashikant Singh, and José A. Hoyos for the helpful discussions. P.K.V. acknowledges support via the IIE Travel award by the Global Engagement Office, IIT Madras. R.N. and P.K.V. also acknowledge funding from the Center for Quantum Information Theory in Matter and Spacetime, IIT Madras and from the Department of Science and Technology, Govt. of India, under Grant No. DST/ICPS/QuST/Theme-3/2019/Q69, as well as support from the Mphasis F1 Foundation via the Centre for Quantum Information, Communication, and Computing (CQuICC). G.K. and T.V. acknowledge support from the National Science Foundation under grant nos. DMR-1506152, DMR-1828489, OAC-1919789. T.V. also acknowledges support for a visit at IIT Madras, where part of the work was completed, via a Visiting Faculty Fellowship of the Office of Global Engagement IIT Madras.

SECTION

2. SUMMARY AND CONCLUSIONS

In this work, we investigated the effects of disorder on the critical behavior of various magnetic systems using large-scale Monte Carlo simulations. We studied the interplay of interactions, quenched disorder, thermal and quantum fluctuations and their effect on the properties of the phase transitions. In this chapter, we summarize our findings and their implications.

In Paper I, we studied site-diluted XY and Heisenberg models to help us understand the phase diagram of diluted magnetic materials, specifically hexagonal ferrites. We explored the phase diagram assuming a percolation scenario as suggested by the experimental observations. We confirmed the percolation theory predictions of the phase boundary in the vicinity of percolation threshold, and also explored the pre-asymptotic region, by the means of large-scale Monte Carlo simulations. Our results showed that the asymptotic critical region is very narrow, and the pre-asymptotic phase boundary follows a different dilution dependence than the experiments. This unusual behavior was later explained by preferential dilution of a specific sub-lattice of the hexagonal ferrites [178].

In Paper II, we studied the effects of finite twists in the boundary conditions on a two-dimensional classical XY model motivated by an unexpected difference of the simulation results of the helicity modulus between infinitesimal and finite twists. We showed that the thermodynamic ensemble is composed of a mixture of states with opposite chirality, as a response to twisted boundary conditions. This mixing of states results in a reduction of the free energy cost associated with a non-infinitesimal twist in the quasi-long-range ordered phase. We also showed that a macroscopic system with the anti-periodic boundary conditions in the quasi-long-range ordered phase spontaneously breaks the chiral symmetry.

We provided an improved prescription for the numerical evaluation of the free energy, and helicity modulus for a finite twist. These results and numerical methods are important for discrete spin systems such as q-state clock model, where twists are unavoidably non-infinitesimal. These results also have implications for experiments on planer magnets.

In Paper III, we studied phases and phase transitions in the disordered one-dimensional quantum q-state clock model using large-scale Monte Carlo simulations. We showed that the quasi-long-range ordered phase, which separates the long-range-ordered phase from the paramagnetic phase, shrinks and vanishes in a multi-critical point as disorder strength is increased. For disorder strengths above the multi-critical point, there is a direct transition between the long-range ordered phase and paramagnetic phases. We characterized the critical behavior across all phase boundaries and confirmed the predictions of the strong-disorder renormalization group theory. The transition between paramagnetic and quasi-long-range ordered phases shows a weak-to-strong disorder crossover, similar to the case of disordered bosons in one dimension [152]. For weak disorder, the transition between quasi-long-range ordered and ordered phases belongs to the same universality class as the clean case. In the strong disorder regime, beyond the multi-critical point, the critical behavior is same as the random transverse field Ising model, i.e. infinite randomness type. In the vicinity of the multi-critical point we also found the signatures of exotic quantum Griffiths phases.

To summarize, we presented in-depth analysis of disorder dependence on phases and phase transitions in several systems. We showed that the disorder gives rise to a variety of emergent behavior such as change of universality class, infinite randomness criticality, Griffiths singularity, etc. This work enhances our understanding of the rich and complex behavior of disordered magnetic systems, providing a motivation for future theoretical and experimental investigations in condensed matter physics and quantum many-body systems.

Going further than the simple models covered in this dissertation, one can include effects of more complicated interactions, or realistic lattice structures. One can also investigate transport properties in the vicinity of phase transitions. These model calculations coupled with first-principles calculations provide a detailed description of interplay of interactions and fluctuations, to explain the experimental results.

REFERENCES

[1] S. E. Rowley, T. Vojta, A. T. Jones, W. Guo, J. Oliveira, F. D. Morrison, N. Lindfield, E. Baggio Saitovitch, B. E. Watts, and J. F. Scott. Quantum percolation phase transition and magnetoelectric dipole glass in hexagonal ferrites. *Phys. Rev. B*, 96:020407, Jul 2017. doi: 10.1103/PhysRevB.96.020407. URL https://link.aps.org/doi/10.1103/PhysRevB.96.020407.

[2] D Bitko, TF Rosenbaum, and G Aeppli. Quantum critical behavior for a model magnet. *Physical review letters*, 77(5):940, 1996.

[3] Sudhir Sachdev. *Quantum Phase Transitions*. Cambridge University Press, Cambridge, 2nd edition, 2011.

[4] N David Mermin and Herbert Wagner. Absence of ferromagnetism or antiferromagnetism in one-or two-dimensional isotropic heisenberg models. *Physical Review Letters*, 17(22):1133, 1966.

[5] J M Kosterlitz and D J Thouless. Ordering, metastability and phase transitions in two-dimensional systems. *Journal of Physics C*, 6(7):1181, apr 1973. doi: 10.1088/0022-3719/6/7/010. URL https://dx.doi.org/10.1088/0022-3719/6/7/010.

[6] V. L. Berezinskii. Destruction of long-range order in one-dimensional and two-dimensional systems having a continuous symmetry group i. classical systems. *Sov. Phys. JETP*, 32:493, 1971.

[7] D. Stauffer and A. Aharony. *Introduction to Percolation Theory*. CRC Press, Boca Raton, 1991.

[8] Mats Wallin, Erik S So, SM Girvin, AP Young, et al. Superconductor-insulator transition in two-dimensional dirty boson systems. *Physical Review B*, 49(17):12115, 1994.

[9] Thomas Vojta. Rare region effects at classical, quantum and nonequilibrium phase transitions. *J. Phys. A*, 39(22):R143, may 2006. doi: 10.1088/0305-4470/39/22/R01. URL https://dx.doi.org/10.1088/0305-4470/39/22/R01.

[10] Julia M Yeomans. *Statistical mechanics of phase transitions*. Clarendon Press, 1992.

[11] Nigel Goldenfeld. *Lectures on phase transitions and the renormalization group*. CRC Press, 2018.

[12] Mark EJ Newman and Gerard T Barkema. *Monte Carlo methods in statistical physics*. Clarendon Press, 1999.

[13] A Brooks Harris. Effect of random defects on the critical behaviour of ising models. *Journal of Physics C: Solid State Physics*, 7(9):1671, 1974.

[14] Thomas Vojta. Disorder in quantum many-body systems. *Ann. Rev. Condens. Mat. Phys.*, 10:233–252, 2019. doi: 10.1146/annurev-conmatphys-031218-013433.

[15] B Derrida and D Stauffer. Corrections to scaling and phenomenological renormalization for 2-dimensional percolation and lattice animal problems. *Journal de Physique*, 46 (10):1623–1630, 1985.

[16] G. Grinstein and A. Luther. Application of the renormalization group to phase transitions in disordered systems. *Phys. Rev. B*, 13:1329–1343, Feb 1976. doi: 10.1103/PhysRevB.13.1329. URL https://link.aps.org/doi/10.1103/PhysRevB.13.1329.

[17] Daniel S. Fisher. Random transverse field ising spin chains. *Phys. Rev. Lett.*, 69: 534–537, Jul 1992. doi: 10.1103/PhysRevLett.69.534.

[18] D. S. Fisher. Critical behavior of random transverse-field Ising spin chains. *Phys. Rev. B*, 51:6411, 1995. doi: 10.1103/PhysRevB.51.6411.

[19] R. B. Griffiths. Nonanalytic behavior above the critical point in a random Ising ferromagnet. *Phys. Rev. Lett.*, 23:17, 1969. doi: 10.1103/PhysRevLett.23.17.

[20] M. Thill and D. A. Huse. Equilibrium behaviour of quantum Ising spin glass. *Physica A*, 214:321, 1995. doi: 10.1016/0378-4371(94)00247-Q.

[21] A. P. Young and H. Rieger. Numerical study of the random transverse-field ising spin chain. *Phys. Rev. B*, 53:8486–8498, Apr 1996. doi: 10.1103/PhysRevB.53.8486. URL https://link.aps.org/doi/10.1103/PhysRevB.53.8486.

[22] Thomas Vojta. Disorder-induced rounding of certain quantum phase transitions. *Phys. Rev. Lett.*, 90:107202, Mar 2003. doi: 10.1103/PhysRevLett.90.107202.

[23] Rastko Sknepnek and Thomas Vojta. Smeared phase transition in a three-dimensional ising model with planar defects: Monte carlo simulations. *Phys. Rev. B*, 69:174410, May 2004. doi: 10.1103/PhysRevB.69.174410. URL https://link.aps.org/doi/10.1103/PhysRevB.69.174410.

[24] Grégory Schehr and Heiko Rieger. Strong-disorder fixed point in the dissipative random transverse-field ising model. *Phys. Rev. Lett.*, 96:227201, Jun 2006. doi: 10.1103/PhysRevLett.96.227201. URL https://link.aps.org/doi/10.1103/PhysRevLett.96.227201.

[25] José A. Hoyos and Thomas Vojta. Theory of smeared quantum phase transitions. *Phys. Rev. Lett.*, 100:240601, Jun 2008. doi: 10.1103/PhysRevLett.100.240601.

[26] T. Vojta. Rare region effects at classical, quantum, and non-equilibrium phase transitions. *J. Phys. A*, 39:R143, 2006. doi: 10.1088/0305-4470/39/22/R01.

[27] T. Vojta. Quantum Griffiths effects and smeared phase transitions in metals: theory and experiment. *J. Low Temp. Phys.*, 161:299, 2010. doi: 10.1007/s10909-010-0205-4.

[28] G. Albanese, F. Leccabue, B. E. Watts, and S. Díaz-Castañón. Magnetic and mössbauer investigation of $PbFe_{12-x}Ga_xO_{19}$ hexagonal ferrites. *J. Mat. Sci*, 37(17): 3759–3763, Sep 2002. ISSN 1573-4803. doi: 10.1023/A:1016529812985. URL https://doi.org/10.1023/A:1016529812985.

[29] Antonio Coniglio. Thermal phase transition of the dilute s-state potts and n-vector models at the percolation threshold. *Phys. Rev. Lett.*, 46:250–253, Jan 1981. doi: 10.1103/PhysRevLett.46.250. URL https://link.aps.org/doi/10.1103/PhysRevLett.46.250.

[30] T. Vojta and J. A. Hoyos. Quantum phase transitions on percolating lattices. In J. Boronat, G. Astrakharchik, and F. Mazzanti, editors, *Recent Progress in Many-Body Theories*, page 235. World Scientific, Singapore, 2008.

[31] Chuanjian Wu, Zhong Yu, Ke Sun, Jinlan Nie, Rongdi Guo, Hai Liu, Xiaona Jiang, and Zhongwen Lan. Calculation of exchange integrals and curie temperature for la-substituted barium hexaferrites. *Scientific Reports*, 6:36200, 2016. doi: 10.1038/srep36200. URL http://dx.doi.org/10.1038/srep36200.

[32] EF Shender and BI Shklovskii. The curie temperature of dilute ferromagnetic alloys near the percolation threshold. *Physics Letters A*, 55(2):77–78, 1975.

[33] B. Kozlov and M. Laguës. Universality of 3d percolation exponents and first-order corrections to scaling for conductivity exponents. *Physica A: Statistical Mechanics and its Applications*, 389(23):5339 – 5346, 2010. ISSN 0378-4371. doi: https://doi.org/10.1016/j.physa.2010.08.002. URL http://www.sciencedirect.com/science/article/pii/S0378437110006758.

[34] Junfeng Wang, Zongzheng Zhou, Wei Zhang, Timothy M. Garoni, and Youjin Deng. Bond and site percolation in three dimensions. *Phys. Rev. E*, 87:052107, May 2013. doi: 10.1103/PhysRevE.87.052107. URL https://link.aps.org/doi/10.1103/PhysRevE.87.052107.

[35] AB Harris and TC Lubensky. Diluted continuous spin models near the percolation threshold. *Journal of Physics A: Mathematical and General*, 17(11):L609, 1984.

[36] A Brooks Harris and Amnon Aharony. Phase diagrams for the randomly diluted resistor network and xy model. *Physical Review B*, 40(10):7230, 1989.

[37] Ulli Wolff. Collective monte carlo updating for spin systems. *Phys. Rev. Lett.*, 62:361–364, Jan 1989. doi: 10.1103/PhysRevLett.62.361. URL https://link.aps.org/doi/10.1103/PhysRevLett.62.361.

[38] Nicholas Metropolis and Stanislaw Ulam. The monte carlo method. *Journal of the American statistical association*, 44(247):335–341, 1949.

[39] H. G. Ballesteros, L. A. Fernández, V. Martín-Mayor, A. Muñoz Sudupe, G. Parisi, and J. J. Ruiz-Lorenzo. Critical exponents of the three-dimensional diluted ising model. *Phys. Rev. B*, 58:2740–2747, Aug 1998. doi: 10.1103/PhysRevB.58.2740.

[40] Thomas Vojta and Rastko Sknepnek. Quantum phase transitions of the diluted o(3) rotor model. *Phys. Rev. B*, 74:094415, Sep 2006. doi: 10.1103/PhysRevB.74.094415. URL https://link.aps.org/doi/10.1103/PhysRevB.74.094415.

[41] Qiong Zhu, Xin Wan, Rajesh Narayanan, José A. Hoyos, and Thomas Vojta. Emerging criticality in the disordered three-color ashkin-teller model. *Phys. Rev. B*, 91:224201, Jun 2015. doi: 10.1103/PhysRevB.91.224201.

[42] Kurt Binder. Finite size scaling analysis of ising model block distribution functions. *Zeitschrift für Physik B*, 43(2):119–140, 1981. doi: 10.1007/BF01293604. URL https://doi.org/10.1007/BF01293604.

[43] Walter Selke and Lev N Shchur. Critical binder cumulant in two-dimensional anisotropic ising models. *Journal of Physics A: Mathematical and General*, 38(44):L739, 2005.

[44] Aloysius P. Gottlob and Martin Hasenbusch. Critical behaviour of the 3d xy-model: a monte carlo study. *Physica A: Statistical Mechanics and its Applications*, 201(4):593 – 613, 1993. ISSN 0378-4371. doi: https://doi.org/10.1016/0378-4371(93)90131-M. URL http://www.sciencedirect.com/science/article/pii/037843719390131M.

[45] R. G. Brown and M. Ciftan. Critical behavior of the helicity modulus for the classical heisenberg model. *Phys. Rev. B*, 74: 224413, Dec 2006. doi: 10.1103/PhysRevB.74.224413. URL https://link.aps.org/doi/10.1103/PhysRevB.74.224413.

[46] S. E. Rowley, Yi-Sheng Chai, Shi-Peng Shen, Young Sun, A. T. Jones, B. E. Watts, and J. F. Scott. Uniaxial ferroelectric quantum criticality in multiferroic hexaferrites bafe12o19 and srfe12o19. *Scientific Reports*, 6:25724, 2016. doi: 10.1038/srep25724. URL http://dx.doi.org/10.1038/srep25724.

[47] Jayanth R Banavar, Marek Cieplak, and Marta Z Cieplak. Influence of boundary conditions on random unfrustrated magnetic systems. *Physical Review B*, 26(5):2482, 1982.

[48] C M Newman and D L Stein. Multiple states and thermodynamic limits in short-ranged ising spin-glass models. *Physical Review B*, 46(2):973, 1992.

[49] Eric O Endo, Aernout CD van Enter, and Arnaud Le Ny. The roles of random boundary conditions in spin systems. In Maria Eulalia Vares, Roberto Fernandez, Luiz Renato Fontes, and Charles M. Newman, editors, *In and Out of Equilibrium 3: Celebrating Vladas Sidoravicius*, pages 371–381. Springer, 2021.

[50] A Gandolfi, C M Newman, and D L Stein. Exotic states in long-range spin glasses. *Communications in Mathematical Physics*, 157(2):371–387, 1993.

[51] Daniel S Fisher and David A Huse. Equilibrium behavior of the spin-glass ordered phase. *Physical Review B*, 38(1):386–411, 1988.

[52] N Akino and JM Kosterlitz. Domain wall renormalization group study of the xy model with quenched random phase shifts. *Physical Review B*, 66(5):054536, 2002.

[53] Hikaru Kawamura and Masaharu Tanemura. Chiral order in a two-dimensional xy spin glass. *Physical Review B*, 36(13):7177, 1987.

[54] M Ney-Nifle and HJ Hilhorst. Chiral and spin order in the two-dimensional±j xy spin glass: Domain-wall scaling analysis. *Physical Review B*, 51(13):8357, 1995.

[55] M.E. Fisher and P.G. de Gennes. Wall phenomena in a critical binary mixture. *C. R. Acad. Sci. Paris Ser. B*, 287:207–209, 1978.

[56] H. W. J. Blöte, John L. Cardy, and M. P. Nightingale. Conformal invariance, the central charge, and universal finite-size amplitudes at criticality. *Phys. Rev. Lett.*, 56:742–745, Feb 1986. doi: 10.1103/PhysRevLett.56.742. URL https://link.aps.org/doi/10.1103/PhysRevLett.56.742.

[57] John L. Cardy. Effect of boundary conditions on the operator content of two-dimensional conformally invariant theories. *Nuclear Physics B*, 275(2):200–218, 1986. ISSN 0550-3213. doi: https://doi.org/10.1016/0550-3213(86)90596-1. URL https://www.sciencedirect.com/science/article/pii/0550321386905961.

[58] Ian Affleck. Universal term in the free energy at a critical point and the conformal anomaly. *Phys. Rev. Lett.*, 56:746–748, Feb 1986. doi: 10.1103/PhysRevLett.56.746. URL https://link.aps.org/doi/10.1103/PhysRevLett.56.746.

[59] Jonathan Bergknoff, Daniel Dantchev, and Joseph Rudnick. Casimir force in the rotor model with twisted boundary conditions. *Physical Review E*, 84(4):041134, 2011.

[60] Daniel Dantchev and Joseph Rudnick. Manipulation and amplification of the casimir force through surface fields using helicity. *Physical Review E*, 95(4):042120, 2017.

[61] DM Dantchev and S Dietrich. Critical casimir effect: Exact results. *Physics Reports*, 1005:1–130, 2023.

[62] Daniel Dantchev. On casimir and helmholtz fluctuation-induced forces in micro-and nano-systems: Survey of some basic results. *Entropy*, 26(6):499, 2024.

[63] N. D. Mermin and H. Wagner. Absence of ferromagnetism or antiferromagnetism in one- or two-dimensional isotropic Heisenberg models. *Phys. Rev. Lett.*, 17:1133–1136, Nov 1966. doi: 10.1103/PhysRevLett.17.1133. URL https://link.aps.org/doi/10.1103/PhysRevLett.17.1133.

[64] Michael E. Fisher, Michael N. Barber, and David Jasnow. Helicity modulus, superfluidity, and scaling in isotropic systems. *Phys. Rev. A*, 8:1111–1124, Aug 1973. doi: 10.1103/PhysRevA.8.1111. URL https://link.aps.org/doi/10.1103/PhysRevA.8.1111.

[65] Joseph Rudnick and David Jasnow. Renormalization-group proof of josephson's relation and ϵ expansion for the helicity modulus (superfluid density). *Phys. Rev. B*, 16:2032–2046, Sep 1977. doi: 10.1103/PhysRevB.16.2032. URL https://link.aps.org/doi/10.1103/PhysRevB.16.2032.

[66] J R Banavar and D Jasnow. Helicity modulus at low temperatures. *J. Phys. A*, 11(7):1361, jul 1978. doi: 10.1088/0305-4470/11/7/024. URL https://dx.doi.org/10.1088/0305-4470/11/7/024.

[67] S. Teitel and C. Jayaprakash. Phase transtions in frustrated two-dimensional XY models. *Physical Review B*, 27:598–601, Jan 1983. doi: 10.1103/PhysRevB.27.598. URL https://link.aps.org/doi/10.1103/PhysRevB.27.598.

[68] M. Caffarel, P. Azaria, B. Delamotte, and D. Mouhanna. Monte carlo calculation of the spin stiffness of the two-dimensional heisenberg model. *Europhysics Letters*, 26(7):493, jun 1994. doi: 10.1209/0295-5075/26/7/003. URL https://dx.doi.org/10.1209/0295-5075/26/7/003.

[69] Martin Hasenbusch. Direct Monte Carlo measurement of the surface tension in ising models. *Journal de Physique I*, 3:753–765, 1993. doi: 10.1051/jp1:1993160. URL https://hal.science/jpa-00246755.

[70] Koji Hukushima. Domain-wall free energy of spin-glass models: Numerical method and boundary conditions. *Phys. Rev. E*, 60:3606–3613, Oct 1999. doi: 10.1103/PhysRevE.60.3606. URL https://link.aps.org/doi/10.1103/PhysRevE.60.3606.

[71] Nicholas Metropolis and Stanislaw Ulam. The Monte Carlo method. *Journal of the American statistical association*, 44(247):335–341, 1949.

[72] Nicholas Metropolis, Arianna W. Rosenbluth, Marshall N. Rosenbluth, Augusta H. Teller, and Edward Teller. Equation of state calculations by fast computing machines. *J. Chem. Phys.*, 21(6):1087–1092, 1953. doi: 10.1063/1.1699114. URL https://doi.org/10.1063/1.1699114.

[73] Atsushi Ueda and Masaki Oshikawa. Resolving the berezinskii-kosterlitz-thouless transition in the two-dimensional xy model with tensor-network-based level spectroscopy. *Physical Review B*, 104(16):165132, 2021.

[74] Gaurav Khairnar, Cameron Lerch, and Thomas Vojta. Phase boundary near a magnetic percolation transition. *European Physical Journal B*, 94(2):1–8, 2021.

[75] David R Nelson and JM Kosterlitz. Universal jump in the superfluid density of two-dimensional superfluids. *Physical Review Letters*, 39(19):1201, 1977.

[76] M Hasenbusch and K Pinn. Computing the roughening transition of ising and solid-on-solid models by bcsos model matching. *Journal of Physics A: Mathematical and General*, 30(1):63, 1997.

[77] Yun-Da Hsieh, Ying-Jer Kao, and Anders W Sandvik. Finite-size scaling method for the Berezinskii–Kosterlitz–Thouless transition. *Journal of Statistical Mechanics: Theory and Experiment*, 2013(09):P09001, 2013.

[78] Raghav G Jha. Critical analysis of two-dimensional classical XY model. *Journal of Statistical Mechanics*, 2020(8):083203, 2020.

[79] Martin Hasenbusch. The kosterlitz–thouless transition in thin films: a monte carlo study of three-dimensional lattice models. *Journal of Statistical Mechanics: Theory and Experiment*, 2009(02):P02005, 2009.

[80] Martin Hasenbusch. The two-dimensional xy model at the transition temperature: a high-precision monte carlo study. *Journal of Physics A: Mathematical and General*, 38 (26):5869, 2005.

[81] Nikolai V. Prokof'ev and Boris V. Svistunov. Two definitions of superfluid density. *Phys. Rev. B*, 61:11282–11284, May 2000. doi: 10.1103/PhysRevB.61.11282. URL https://link.aps.org/doi/10.1103/PhysRevB.61.11282.

[82] P. C. Hohenberg and B. I. Halperin. Theory of dynamic critical phenomena. *Rev. Mod. Phys.*, 49:435–479, Jul 1977. doi: 10.1103/RevModPhys.49.435. URL https://link.aps.org/doi/10.1103/RevModPhys.49.435.

[83] Jacques Villain. Theory of one-and two-dimensional magnets with an easy magnetization plane. ii. the planar, classical, two-dimensional magnet. *Journal de Physique*, 36 (6):581–590, 1975.

[84] Jorge V José, Leo P Kadanoff, Scott Kirkpatrick, and David R Nelson. Renormalization, vortices, and symmetry-breaking perturbations in the two-dimensional planar model. *Physical Review B*, 16(3):1217, 1977.

[85] John L Cardy. Universal properties of u (1) gauge theories. *Nuclear Physics B*, 170(3): 369–387, 1980.

[86] A Vallat and H Beck. Coulomb-gas representation of the two-dimensional xy model on a torus. *Physical Review B*, 50(6):4015, 1994.

[87] Thierry Giamarchi. *Quantum Physics in One Dimension*. Clarendon Press, Oxford, 2004.

[88] Sergei Lukyanov. Low energy effective hamiltonian for the xxz spin chain. *Nuclear Physics B*, 522(3):533–549, 1998. ISSN 0550-3213. doi: https://doi.org/10.1016/S0550-3213(98)00249-1. URL https://www.sciencedirect.com/science/article/pii/S0550321398002491.

[89] Roberto E Troncoso, Arne Brataas, and Asle Sudbø. Fingerprints of universal spin-stiffness jump in two-dimensional ferromagnets. *Physical Review Letters*, 125(23): 237204, 2020.

[90] Yuta Kumano, Koji Hukushima, Yusuke Tomita, and Masaki Oshikawa. Response to a twist in systems with z p symmetry: The two-dimensional p-state clock model. *Physical Review B*, 88(10):104427, 2013.

[91] Fawaz Hrahsheh, Hatem Barghathi, and Thomas Vojta. Infinite-randomness criticality in a randomly layered heisenberg magnet. *Phys. Rev. B*, 84:184202, Nov 2011. doi: 10.1103/PhysRevB.84.184202. URL https://link.aps.org/doi/10.1103/PhysRevB.84.184202.

[92] Thomas Vojta. Phases and phase transitions in disordered quantum systems. *AIP Conf. Proc.*, 1550(1):188–247, 2013. doi: 10.1063/1.4818403. URL https://aip.scitation.org/doi/abs/10.1063/1.4818403.

[93] A B Harris. Effect of random defects on the critical behaviour of ising models. *Journal of Physics C: Solid State Physics*, 7(9):1671–1692, may 1974. doi: 10.1088/0022-3719/7/9/009. URL https://doi.org/10.1088/0022-3719/7/9/009.

[94] Yoseph Imry and Shang-keng Ma. Random-field instability of the ordered state of continuous symmetry. *Phys. Rev. Lett.*, 35: 1399–1401, Nov 1975. doi: 10.1103/PhysRevLett.35.1399. URL https://link.aps.org/doi/10.1103/PhysRevLett.35.1399.

[95] Daniel S. Fisher. Random transverse field ising spin chains. *Phys. Rev. Lett.*, 69:534–537, Jul 1992. doi: 10.1103/PhysRevLett.69.534. URL https://link.aps.org/doi/10.1103/PhysRevLett.69.534.

[96] Daniel S. Fisher. Critical behavior of random transverse-field ising spin chains. *Phys. Rev. B*, 51:6411–6461, Mar 1995. doi: 10.1103/PhysRevB.51.6411. URL https://link.aps.org/doi/10.1103/PhysRevB.51.6411.

[97] H. Rieger and A. P. Young. Griffiths singularities in the disordered phase of a quantum ising spin glass. *Phys. Rev. B*, 54:3328–3335, Aug 1996. doi: 10.1103/PhysRevB.54.3328. URL https://link.aps.org/doi/10.1103/PhysRevB.54.3328.

[98] Muyu Guo, R. N. Bhatt, and David A. Huse. Quantum griffiths singularities in the transverse-field ising spin glass. *Phys. Rev. B*, 54:3336–3342, Aug 1996. doi: 10.1103/PhysRevB.54.3336. URL https://link.aps.org/doi/10.1103/PhysRevB.54.3336.

[99] José A. Hoyos, Chetan Kotabage, and Thomas Vojta. Effects of dissipation on a quantum critical point with disorder. *Phys. Rev. Lett.*, 99:230601, Dec 2007. doi: 10.1103/PhysRevLett.99.230601. URL https://link.aps.org/doi/10.1103/PhysRevLett.99.230601.

[100] Thomas Vojta, Chetan Kotabage, and José A. Hoyos. Infinite-randomness quantum critical points induced by dissipation. *Phys. Rev. B*, 79:024401, Jan 2009. doi: 10.1103/PhysRevB.79.024401. URL https://link.aps.org/doi/10.1103/PhysRevB.79.024401.

[101] Thomas Vojta. Smearing of the phase transition in ising systems with planar defects. *J. Phys. A*, 36(43):10921, oct 2003. doi: 10.1088/0305-4470/36/43/017. URL https://dx.doi.org/10.1088/0305-4470/36/43/017.

[102] J M Kosterlitz and D J Thouless. Ordering, metastability and phase transitions in two-dimensional systems. *Journal of Physics C: Solid State Physics*, 6(7):1181, apr 1973. doi: 10.1088/0022-3719/6/7/010. URL https://dx.doi.org/10.1088/0022-3719/6/7/010.

[103] Jorge V. José, Leo P. Kadanoff, Scott Kirkpatrick, and David R. Nelson. Renormalization, vortices, and symmetry-breaking perturbations in the two-dimensional planar model. *Phys. Rev. B*, 16:1217–1241, Aug 1977. doi: 10.1103/PhysRevB.16.1217. URL https://link.aps.org/doi/10.1103/PhysRevB.16.1217.

[104] S. Elitzur, R. B. Pearson, and J. Shigemitsu. Phase structure of discrete abelian spin and gauge systems. *Phys. Rev. D*, 19:3698–3714, Jun 1979. doi: 10.1103/PhysRevD.19.3698. URL https://link.aps.org/doi/10.1103/PhysRevD.19.3698.

[105] J L Cardy. General discrete planar models in two dimensions: Duality properties and phase diagrams. *Journal of Physics A: Mathematical and General*, 13(4):1507, apr 1980. doi: 10.1088/0305-4470/13/4/037. URL https://dx.doi.org/10.1088/0305-4470/13/4/037.

[106] Jan Tobochnik. Properties of the q-state clock model for $q = 4, 5,$ and6. *Phys. Rev. B*, 26:6201–6207, Dec 1982. doi: 10.1103/PhysRevB.26.6201. URL https://link.aps.org/doi/10.1103/PhysRevB.26.6201.

[107] Murty S. S. Challa and D. P. Landau. Critical behavior of the six-state clock model in two dimensions. *Phys. Rev. B*, 33:437–443, Jan 1986. doi: 10.1103/PhysRevB.33.437. URL https://link.aps.org/doi/10.1103/PhysRevB.33.437.

[108] A Yamagata and I Ono. Phase transitions of the 6-clock model in two dimensions. *Journal of Physics A: Mathematical and General*, 24(1):265, jan 1991. doi: 10.1088/0305-4470/24/1/033. URL https://dx.doi.org/10.1088/0305-4470/24/1/033.

[109] Yusuke Tomita and Yutaka Okabe. Probability-changing cluster algorithm for two-dimensional XY and clock models. *Phys. Rev. B*, 65:184405, Apr 2002. doi: 10.1103/PhysRevB.65.184405. URL https://link.aps.org/doi/10.1103/PhysRevB.65.184405.

[110] Cintia M. Lapilli, Peter Pfeifer, and Carlos Wexler. Universality away from critical points in two-dimensional phase transitions. *Phys. Rev. Lett.*, 96:140603, Apr 2006. doi: 10.1103/PhysRevLett.96.140603. URL https://link.aps.org/doi/10.1103/PhysRevLett.96.140603.

[111] Haruhiko Matsuo and Kiyohide Nomura. Berezinskii–kosterlitz–thouless transitions in the six-state clock model. *Journal of Physics A: Mathematical and General*, 39(12):2953, mar 2006. doi: 10.1088/0305-4470/39/12/006. URL https://dx.doi.org/10.1088/0305-4470/39/12/006.

[112] A. Faissal Brito, José Arnaldo Redinz, and J. A. Plascak. Two-dimensional xy and clock models studied via the dynamics generated by rough surfaces. *Phys. Rev. E*, 81:031130, Mar 2010. doi: 10.1103/PhysRevE.81.031130. URL https://link.aps.org/doi/10.1103/PhysRevE.81.031130.

[113] I. G. Enting and N. Clisby. Series analysis of a kosterlitz-thouless transition: The 6-state planar potts model. *Journal of Statistical Physics*, 145(3): 696–712, Nov 2011. ISSN 1572-9613. doi: 10.1007/s10955-011-0322-8. URL https://doi.org/10.1007/s10955-011-0322-8.

[114] O. Borisenko, G. Cortese, R. Fiore, M. Gravina, and A. Papa. Numerical study of the phase transitions in the two-dimensional z(5) vector model. *Phys. Rev. E*, 83:041120, Apr 2011. doi: 10.1103/PhysRevE.83.041120. URL https://link.aps.org/doi/10.1103/PhysRevE.83.041120.

[115] G. Ortiz, E. Cobanera, and Z. Nussinov. Dualities and the phase diagram of the p-clock model. *Nuclear Physics B*, 854(3):780–814, 2012. ISSN 0550-3213. doi: https://doi.org/10.1016/j.nuclphysb.2011.09.012. URL https://www.sciencedirect.com/science/article/pii/S0550321311005219.

[116] Yuta Kumano, Koji Hukushima, Yusuke Tomita, and Masaki Oshikawa. Response to a twist in systems with Z_p symmetry: The two-dimensional p-state clock model. *Phys. Rev. B*, 88:104427, Sep 2013. doi: 10.1103/PhysRevB.88.104427. URL https://link.aps.org/doi/10.1103/PhysRevB.88.104427.

[117] Christophe Chatelain. Dmrg study of the berezinskii–kosterlitz–thouless transitions of the 2d five-state clock model. *Journal of Statistical Mechanics: Theory and Experiment*, 2014(11):P11022, nov 2014. doi: 10.1088/1742-5468/2014/11/P11022. URL https://dx.doi.org/10.1088/1742-5468/2014/11/P11022.

[118] Jing Chen, Hai-Jun Liao, Hai-Dong Xie, Xing-Jie Han, Rui-Zhen Huang, Song Cheng, Zhong-Chao Wei, Zhi-Yuan Xie, and Tao Xiang. Phase transition of the q-state clock model: Duality and tensor renormalization*. *Chinese Physics Letters*, 34(5):050503, may 2017. doi: 10.1088/0256-307X/34/5/050503. URL https://dx.doi.org/10.1088/0256-307X/34/5/050503.

[119] G. Sun, T. Vekua, E. Cobanera, and G. Ortiz. Phase transitions in the F_p and u(1) clock models. *Phys. Rev. B*, 100:094428, Sep 2019. doi: 10.1103/PhysRevB.100.094428. URL https://link.aps.org/doi/10.1103/PhysRevB.100.094428.

[120] Zi-Qian Li, Li-Ping Yang, Z. Y. Xie, Hong-Hao Tu, Hai-Jun Liao, and T. Xiang. Critical properties of the two-dimensional q-state clock model. *Phys. Rev. E*, 101:060105, Jun 2020. doi: 10.1103/PhysRevE.101.060105. URL https://link.aps.org/doi/10.1103/PhysRevE.101.060105.

[121] Yusuke Miyajima, Yusuke Murata, Yasuhiro Tanaka, and Masahito Mochizuki. Machine learning detection of berezinskii-kosterlitz-thouless transitions in q-state clock models. *Phys. Rev. B*, 104:075114, Aug 2021. doi: 10.1103/PhysRevB.104.075114. URL https://link.aps.org/doi/10.1103/PhysRevB.104.075114.

[122] Hao Chen, Pengcheng Hou, Sheng Fang, and Youjin Deng. Monte carlo study of duality and the berezinskii-kosterlitz-thouless phase transitions of the two-dimensional q-state clock model in flow representations. *Phys. Rev. E*, 106:024106, Aug 2022. doi: 10.1103/PhysRevE.106.024106. URL https://link.aps.org/doi/10.1103/PhysRevE.106.024106.

[123] Luong Minh Tuan, Ta Thanh Long, Duong Xuan Nui, Pham Tuan Minh, Nguyen Duc Trung Kien, and Dao Xuan Viet. Binder ratio in the two-dimensional q-state clock model. *Phys. Rev. E*, 106:034138, Sep 2022. doi: 10.1103/PhysRevE.106.034138. URL https://link.aps.org/doi/10.1103/PhysRevE.106.034138.

[124] Guanrong Li, Kwok Ho Pai, and Zheng-Cheng Gu. Tensor-network renormalization approach to the q-state clock model. *Phys. Rev. Res.*, 4: 023159, May 2022. doi: 10.1103/PhysRevResearch.4.023159. URL https://link.aps.org/doi/10.1103/PhysRevResearch.4.023159.

[125] Hiromi Otsuka, Kenta Shiina, and Yutaka Okabe. Comprehensive studies on the universality of bkt transitions—machine-learning study, monte carlo simulation, and level-spectroscopy method. *Journal of Physics A: Mathematical and Theoretical*, 56(23):235001, may 2023. doi: 10.1088/1751-8121/acd156. URL https://dx.doi.org/10.1088/1751-8121/acd156.

[126] Wei chen Guo and Liang He. Learning phase transitions from regression uncertainty: a new regression-based machine learning approach for automated detection of phases of matter. *New Journal of Physics*, 25(8):083037, aug 2023. doi: 10.1088/1367-2630/acef4e. URL https://dx.doi.org/10.1088/1367-2630/acef4e.

[127] Daniel Podolsky, Efrat Shimshoni, Giovanna Morigi, and Shmuel Fishman. Buckling transitions and clock order of two-dimensional coulomb crystals. *Phys. Rev. X*, 6:031025, Aug 2016. doi: 10.1103/PhysRevX.6.031025. URL https://link.aps.org/doi/10.1103/PhysRevX.6.031025.

[128] Ryui Kaneko, Yoshihiko Nonomura, and Masanori Kohno. Thermal algebraic-decay charge liquid driven by competing short-range coulomb repulsion. *Phys. Rev. B*, 97:205125, May 2018. doi: 10.1103/PhysRevB.97.205125. URL https://link.aps.org/doi/10.1103/PhysRevB.97.205125.

[129] Richard L. C. Vink. Universality class of a displacive structural phase transition in two dimensions. *Phys. Rev. E*, 98:062109, Dec 2018. doi: 10.1103/PhysRevE.98.062109. URL https://link.aps.org/doi/10.1103/PhysRevE.98.062109.

[130] Peter P. Orth, Premala Chandra, Piers Coleman, and Jörg Schmalian. Emergent critical phase and ricci flow in a 2d frustrated heisenberg model. *Phys. Rev. Lett.*, 109:237205, Dec 2012. doi: 10.1103/PhysRevLett.109.237205. URL https://link.aps.org/doi/10.1103/PhysRevLett.109.237205.

[131] Peter P. Orth, Premala Chandra, Piers Coleman, and Jörg Schmalian. Emergent criticality and friedan scaling in a two-dimensional frustrated heisenberg antiferromagnet. *Phys. Rev. B*, 89:094417, Mar 2014. doi: 10.1103/PhysRevB.89.094417. URL https://link.aps.org/doi/10.1103/PhysRevB.89.094417.

[132] Bhilahari Jeevanesan, Premala Chandra, Piers Coleman, and Peter P. Orth. Emergent power-law phase in the 2d heisenberg windmill antiferromagnet: A computational experiment. *Phys. Rev. Lett.*, 115: 177201, Oct 2015. doi: 10.1103/PhysRevLett.115.177201. URL https://link.aps.org/doi/10.1103/PhysRevLett.115.177201.

[133] M. Žukovič and A. Bobák. Phase transitions in a triangular blume-capel antiferromagnet. *Phys. Rev. E*, 87:032121, Mar 2013. doi: 10.1103/PhysRevE.87.032121. URL https://link.aps.org/doi/10.1103/PhysRevE.87.032121.

[134] Hiromi Otsuka, Yutaka Okabe, and Kiyohide Nomura. Global phase diagram and six-state clock universality behavior in the triangular antiferromagnetic ising model with anisotropic next-nearest-neighbor coupling: Level-spectroscopy approach. *Phys. Rev. E*, 74:011104, Jul 2006. doi: 10.1103/PhysRevE.74.011104. URL https://link.aps.org/doi/10.1103/PhysRevE.74.011104.

[135] Daniel Blankschtein, M. Ma, A. Nihat Berker, Gary S. Grest, and C. M. Soukoulis. Orderings of a stacked frustrated triangular system in three dimensions. *Phys. Rev. B*, 29:5250–5252, May 1984. doi: 10.1103/PhysRevB.29.5250. URL https://link.aps.org/doi/10.1103/PhysRevB.29.5250.

[136] S. V. Isakov and R. Moessner. Interplay of quantum and thermal fluctuations in a frustrated magnet. *Phys. Rev. B*, 68:104409, Sep 2003. doi: 10.1103/PhysRevB.68.104409. URL https://link.aps.org/doi/10.1103/PhysRevB.68.104409.

[137] Gia-Wei Chern and Oleg Tchernyshyov. Magnetic charge and ordering in kagome spin ice. *Philosophical Transactions of the Royal Society A: Mathematical, Physical and Engineering Sciences*, 370(1981):5718–5737, 12 2012. ISSN 1364-503X. doi: 10.1098/rsta.2011.0388. URL http://dx.doi.org/10.1098/rsta.2011.0388.

[138] Wen-Yu Su, Feng Hu, Chen Cheng, and Nvsen Ma. Berezinskii-kosterlitz-thouless phase transitions in a kagome spin ice by a quantifying monte carlo process: Distribution of hamming distances. *Phys. Rev. B*, 108:134422, Oct 2023. doi: 10.1103/PhysRevB.108.134422. URL https://link.aps.org/doi/10.1103/PhysRevB.108.134422.

[139] Kedar Damle. Melting of three-sublattice order in easy-axis antiferromagnets on triangular and kagome lattices. *Phys. Rev. Lett.*, 115: 127204, Sep 2015. doi: 10.1103/PhysRevLett.115.127204. URL https://link.aps.org/doi/10.1103/PhysRevLett.115.127204.

[140] S. C. Chae, N. Lee, Y. Horibe, M. Tanimura, S. Mori, B. Gao, S. Carr, and S.-W. Cheong. Direct observation of the proliferation of ferroelectric loop domains and vortex-antivortex pairs. *Phys. Rev. Lett.*, 108:167603, Apr 2012. doi: 10.1103/PhysRevLett.108.167603. URL https://link.aps.org/doi/10.1103/PhysRevLett.108.167603.

[141] Han Li, Yuan Da Liao, Bin-Bin Chen, Xu-Tao Zeng, Xian-Lei Sheng, Yang Qi, Zi Yang Meng, and Wei Li. Kosterlitz-thouless melting of magnetic order in the triangular quantum ising material tmmggao4. *Nature Communications*, 11(1): 1111, Feb 2020. ISSN 2041-1723. doi: 10.1038/s41467-020-14907-8. URL https://doi.org/10.1038/s41467-020-14907-8.

[142] T. Giamarchi and H. J. Schulz. Localization and interaction in one-dimensional quantum fluids. *Europhysics Letters*, 3(12):1287, jun 1987. doi: 10.1209/0295-5075/3/12/007. URL https://dx.doi.org/10.1209/0295-5075/3/12/007.

[143] Zoran Ristivojevic, Aleksandra Petković, Pierre Le Doussal, and Thierry Giamarchi. Phase transition of interacting disordered bosons in one dimension. *Phys. Rev. Lett.*, 109:026402, Jul 2012. doi: 10.1103/PhysRevLett.109.026402. URL https://link.aps.org/doi/10.1103/PhysRevLett.109.026402.

[144] Ehud Altman, Yariv Kafri, Anatoli Polkovnikov, and Gil Refael. Phase transition in a system of one-dimensional bosons with strong disorder. *Phys. Rev. Lett.*, 93:150402, Oct 2004. doi: 10.1103/PhysRevLett.93.150402.

[145] Ehud Altman, Yariv Kafri, Anatoli Polkovnikov, and Gil Refael. Insulating phases and superfluid-insulator transition of disordered boson chains. *Phys. Rev. Lett.*, 100:170402, May 2008. doi: 10.1103/PhysRevLett.100.170402. URL http://link.aps.org/doi/10.1103/PhysRevLett.100.170402.

[146] Ehud Altman, Yariv Kafri, Anatoli Polkovnikov, and Gil Refael. Superfluid-insulator transition of disordered bosons in one dimension. *Phys. Rev. B*, 81:174528, May 2010. doi: 10.1103/PhysRevB.81.174528. URL https://link.aps.org/doi/10.1103/PhysRevB.81.174528.

[147] Susanne Pielawa and Ehud Altman. Numerical evidence for strong randomness scaling at a superfluid-insulator transition of one-dimensional bosons. *Phys. Rev. B*, 88:224201, Dec 2013. doi: 10.1103/PhysRevB.88.224201. URL http://link.aps.org/doi/10.1103/PhysRevB.88.224201.

[148] Lode Pollet, Nikolay V. Prokof'ev, and Boris V. Svistunov. Asymptotically exact scenario of strong-disorder criticality in one-dimensional superfluids. *Phys. Rev. B*, 89: 054204, Feb 2014. doi: 10.1103/PhysRevB.89.054204.

[149] Elmer V. H. Doggen, Gabriel Lemarié, Sylvain Capponi, and Nicolas Laflorencie. Weak- versus strong-disorder superfluid—bose glass transition in one dimension. *Phys. Rev. B*, 96:180202, Nov 2017. doi: 10.1103/PhysRevB.96.180202. URL https://link.aps.org/doi/10.1103/PhysRevB.96.180202.

[150] Tobias Pfeffer, Zhiyuan Yao, and Lode Pollet. Strong randomness criticality in the scratched xy model. *Phys. Rev. B*, 99: 104514, Mar 2019. doi: 10.1103/PhysRevB.99.104514. URL https://link.aps.org/doi/10.1103/PhysRevB.99.104514.

[151] G. Lemarié, I. Maccari, and C. Castellani. Kane-fisher weak link physics in the clean scratched xy model. *Phys. Rev. B*, 99: 054519, Feb 2019. doi: 10.1103/PhysRevB.99.054519. URL https://link.aps.org/doi/10.1103/PhysRevB.99.054519.

[152] Fawaz Hrahsheh and Thomas Vojta. Disordered bosons in one dimension: From weak- to strong-randomness criticality. *Phys. Rev. Lett.*, 109:265303, Dec 2012. doi: 10.1103/PhysRevLett.109.265303. URL https://link.aps.org/doi/10.1103/PhysRevLett.109.265303.

[153] T. Senthil and Satya N. Majumdar. Critical properties of random quantum potts and clock models. *Phys. Rev. Lett.*, 76: 3001–3004, Apr 1996. doi: 10.1103/PhysRevLett.76.3001. URL https://link.aps.org/doi/10.1103/PhysRevLett.76.3001.

[154] Enrico Carlon, Péter Lajkó, and Ferenc Iglói. Disorder induced cross-over effects at quantum critical points. *Phys. Rev. Lett.*, 87: 277201, Dec 2001. doi: 10.1103/PhysRevLett.87.277201. URL http://link.aps.org/doi/10.1103/PhysRevLett.87.277201.

[155] Barry M. McCoy and Tai Tsun Wu. Random impurities as the cause of smooth specific heats near the critical temperature. *Phys. Rev. Lett.*, 21:549–551, Aug 1968. doi: 10.1103/PhysRevLett.21.549. URL https://link.aps.org/doi/10.1103/PhysRevLett.21.549.

[156] R. Shankar and Ganpathy Murthy. Nearest-neighbor frustrated random-bond model in d=2: Some exact results. *Phys. Rev. B*, 36:536–545, Jul 1987. doi: 10.1103/PhysRevB.36.536. URL https://link.aps.org/doi/10.1103/PhysRevB.36.536.

[157] Tasrief Surungan and Yutaka Okabe. Kosterlitz-thouless transition in planar spin models with bond dilution. *Phys. Rev. B*, 71: 184438, May 2005. doi: 10.1103/PhysRevB.71.184438. URL https://link.aps.org/doi/10.1103/PhysRevB.71.184438.

[158] Seung Ki Baek, Petter Minnhagen, and Beom Jun Kim. True and quasi-long-range order in the generalized q-state clock model. *Phys. Rev. E*, 80:060101, Dec 2009. doi: 10.1103/PhysRevE.80.060101. URL https://link.aps.org/doi/10.1103/PhysRevE.80.060101.

[159] K. Binder. Finite size scaling analysis of ising model block distribution functions. *Zeitschrift für Physik B Condensed Matter*, 43(2):119–140, Jun 1981. ISSN 1431-584X. doi: 10.1007/BF01293604. URL https://doi.org/10.1007/BF01293604.

[160] Thomas Vojta, Jack Crewse, Martin Puschmann, Daniel Arovas, and Yury Kiselev. Quantum critical behavior of the superfluid-mott glass transition. *Phys. Rev. B*, 94:134501, Oct 2016. doi: 10.1103/PhysRevB.94.134501. URL https://link.aps.org/doi/10.1103/PhysRevB.94.134501.

[161] Fred Cooper, B. Freedman, and Dean Preston. Solving $\phi^4_{1,2}$ field theory with monte carlo. *Nuclear Physics B*, 210(2):210–228, 1982. ISSN 0550-3213. doi: https://doi.org/10.1016/0550-3213(82)90240-1. URL https://www.sciencedirect.com/science/article/pii/0550321382902401.

[162] Jae-Kwon Kim. Application of finite size scaling to monte carlo simulations. *Phys. Rev. Lett.*, 70:1735–1738, Mar 1993. doi: 10.1103/PhysRevLett.70.1735. URL https://link.aps.org/doi/10.1103/PhysRevLett.70.1735.

[163] Caracciolo, S., Gambassi, A., Gubinelli, M., and Pelissetto, A. Finite-size correlation length and violations of finite-size scaling. *Eur. Phys. J. B*, 20(2):255–265, 2001. doi: 10.1007/BF01352587. URL https://doi.org/10.1007/BF01352587.

[164] Gaurav Khairnar and Thomas Vojta. Helicity modulus and chiral symmetry breaking for boundary conditions with finite twist. *Phys. Rev. E*, 111:024114, Feb 2025. doi: 10.1103/PhysRevE.111.024114. URL https://link.aps.org/doi/10.1103/PhysRevE.111.024114.

[165] Einar B. Stiansen, Iver Bakken Sperstad, and Asle Sudbø. Criticality of compact and noncompact quantum dissipative Z_4 models in (1 + 1) dimensions. *Phys. Rev. B*, 83:115134, Mar 2011. doi: 10.1103/PhysRevB.83.115134. URL https://link.aps.org/doi/10.1103/PhysRevB.83.115134.

[166] J. Hooyberghs, F. Iglói, and C. Vanderzande. Strong-disorder fixed point in absorbing-state phase transitions. *Phys. Rev. Lett.*, 90:100601, 2003. doi: 10.1103/PhysRevLett.90.100601.

[167] T. Vojta and M. Dickison. Critical behavior and Griffiths effects in the disordered contact process. *Phys. Rev. E*, 72:036126, 2005. doi: 10.1103/PhysRevE.72.036126.

[168] T. Vojta, A. Farquhar, and J. Mast. Infinite-randomness critical point in the two-dimensional disordered contact process. *Phys. Rev. E*, 79:011111, 2009. doi: 10.1103/PhysRevE.79.011111.

[169] Rastko Sknepnek, Thomas Vojta, and Matthias Vojta. Exotic versus conventional scaling and universality in a disordered bilayer quantum heisenberg antiferromagnet. *Phys. Rev. Lett.*, 93:097201, Aug 2004. doi: 10.1103/PhysRevLett.93.097201. URL https://link.aps.org/doi/10.1103/PhysRevLett.93.097201.

[170] S. K. Yip, T. Li, and P. Kumar. Thermodynamic considerations and the phase diagram of superconducting upt_3. *Phys. Rev. B*, 43:2742–2747, Feb 1991. doi: 10.1103/PhysRevB.43.2742. URL https://link.aps.org/doi/10.1103/PhysRevB.43.2742.

[171] Jae-Kwon Kim. Asymptotic scaling of the mass gap in the two-dimensional o(3) nonlinear σ model: A numerical study. *Phys. Rev. D*, 50:4663–4667, Oct 1994. doi: 10.1103/PhysRevD.50.4663. URL https://link.aps.org/doi/10.1103/PhysRevD.50.4663.

[172] H. Rieger and A. P. Young. Zero-temperature quantum phase transition of a two-dimensional ising spin glass. *Phys. Rev. Lett.*, 72: 4141–4144, Jun 1994. doi: 10.1103/PhysRevLett.72.4141. URL https://link.aps.org/doi/10.1103/PhysRevLett.72.4141.

[173] Valentin Anfray and Christophe Chatelain. Numerical evidence of a universal critical behavior of two-dimensional and three-dimensional random quantum clock and potts models. *Phys. Rev. E*, 108:014124, Jul 2023. doi: 10.1103/PhysRevE.108.014124. URL https://link.aps.org/doi/10.1103/PhysRevE.108.014124.

[174] M.J. Thill and D.A. Huse. Equilibrium behaviour of quantum ising spin glass. *Physica A: Statistical Mechanics and its Applications*, 214(3):321–355, 1995. ISSN 0378-4371. doi: https://doi.org/10.1016/0378-4371(94)00247-Q. URL https://www.sciencedirect.com/science/article/pii/037843719400247Q.

[175] Masaki Oshikawa. Ordered phase and scaling in Z_n models and the three-state antiferromagnetic potts model in three dimensions. *Phys. Rev. B*, 61:3430–3434, Feb 2000. doi: 10.1103/PhysRevB.61.3430. URL https://link.aps.org/doi/10.1103/PhysRevB.61.3430.

[176] Jie Lou, Anders W. Sandvik, and Leon Balents. Emergence of u(1) symmetry in the 3d xy model with Z_q anisotropy. *Phys. Rev. Lett.*, 99:207203, Nov 2007. doi: 10.1103/PhysRevLett.99.207203. URL https://link.aps.org/doi/10.1103/PhysRevLett.99.207203.

[177] Daniel S. Fisher and Matthew P. A. Fisher. Onset of superfluidity in random media. *Phys. Rev. Lett.*, 61:1847–1850, Oct 1988. doi: 10.1103/PhysRevLett.61.1847. URL https://link.aps.org/doi/10.1103/PhysRevLett.61.1847.

[178] Logan Sowadski, Sean Anderson, Cameron Lerch, Julia Medvedeva, and Thomas Vojta. Magnetic properties of diluted hexaferrites. *Physical Review B*, 110(1):014432, 2024.

VITA

Gaurav Ramesh Khairnar was born in Nashik, Maharashtra, India. He completed his primary to high school education in Nashik. He attended Indian Institute of Science Education and Research (IISER), Pune, from 2012 to 2017, earning his Bachelor's and Master's degrees (BS-MS) in Science. During this period, he worked with Dr. Anil Gangal on multiple semester projects, where he discovered his interests in theoretical physics. He then worked under the supervision of Dr. MS Santhanam and presented a Master's thesis on 'Classical and Quantum Dynamics of Delta-kicked Duffing Oscillator'. Later, from 2017 to 2018, he studied 'Many-body Localization in Open Quantum Systems' with Dr. Deepak Dhar. In 2018, he joined the Department of Physics at Missouri University of Science and Technology, Rolla as a graduate student and became a member of Dr. Thomas Vojta's research group. During his time working with Dr. Thomas Vojta, he published three journal articles in respectable journals, presented research in multiple international conferences and participated in prestigious summer and winter schools. Gaurav's research activities have been recognized with two first-place awards in the annual department-wide graduate research competition at Missouri University of Science and Technology. In May 2025, he received his Ph.D. in Physics from Missouri University of Science and Technology.